The Astrophysical Journal Letters, 907:L10 (33pp), 2021 January 20 https://doi.org/10.3847/2041-8213/abcc02
© 2021. The American Astronomical Society. All rights reserved.

Kinematic Analysis of a Protostellar Multiple System: Measuring the Protostar Masses and Assessing Gravitational Instability in the Disks of L1448 IRS3B and L1448 IRS3A

Nickalas K. Reynolds[1], John J. Tobin[2], Patrick Sheehan[2,3], Sarah I. Sadavoy[4], Kaitlin M. Kratter[5], Zhi-Yun Li[6], Claire J. Chandler[7], Dominique Segura-Cox[8], Leslie W. Looney[9], and Michael M. Dunham[10,11]
[1] Homer L. Dodge Department of Physics and Astronomy, University of Oklahoma, 440 W. Brooks Street, Norman, OK 73019, USA
[2] National Radio Astronomy Observatory, 520 Edgemont Rd. Charlottesville, VA 22901, USA
[3] Department of Physics and Astronomy, Northwestern University, 2145 Sheridan Road, Evanston, IL 60208, USA
[4] Department of Physics, Engineering Physics & Astronomy, Queen's University, Kingston, Ontario, Canada
[5] University of Arizona, Steward Observatory, Tucson, AZ 85721, USA
[6] Department of Astronomy, University of Virginia, Charlottesville, VA 22903, USA
[7] National Radio Astronomy Observatory, P.O. Box O, Socorro, NM 87801, USA
[8] Center for Astrochemical Studies, Max-Planck-Institut für extraterrestrische Physik (MPE), Giessenbachstr. 1, D-85741 Garching, Germany
[9] Department of Astronomy, University of Illinois, Urbana, IL 61801, USA
[10] Department of Physics, State University of New York Fredonia, Fredonia, NY 14063, USA
[11] Harvard-Smithsonian Center for Astrophysics, 60 Garden St, MS 78, Cambridge, MA 02138, USA
Received 2020 June 3; revised 2020 October 28; accepted 2020 November 11; published 2021 January 18

Abstract

We present new Atacama Large Millimeter/submillimeter Array observations toward a compact (∼230 au separation) triple protostar system, L1448 IRS3B, at 879 μm with $0\farcs11 \times 0\farcs05$ resolution. Spiral arm structure within the circum-multiple disk is well resolved in dust continuum toward IRS3B, and we detect the known wide (∼2300 au) companion, IRS3A, also resolving possible spiral substructure. Using dense gas tracers, $C^{17}O$ ($J = 3 \rightarrow 2$), $H^{13}CO^+$ ($J = 4 \rightarrow 3$), and $H^{13}CN$ ($J = 4 \rightarrow 3$), we resolve the Keplerian rotation for both the circum-triple disk in IRS3B and the disk around IRS3A. Furthermore, we use the molecular line kinematic data and radiative transfer modeling of the molecular line emission to confirm that the disks are in Keplerian rotation with fitted masses of $1.19^{+0.13}_{-0.07}$ $M_\odot$ for IRS3B-ab and $1.51^{+0.06}_{-0.07}$ $M_\odot$ for IRS3A and place an upper limit on the central protostar mass for the tertiary IRS3B-c of 0.2 $M_\odot$. We measure the mass of the fragmenting disk of IRS3B to be ∼0.29 $M_\odot$ from the dust continuum emission of the circum-multiple disk and estimate the mass of the clump surrounding IRS3B-c to be 0.07 $M_\odot$. We also find that the disk around IRS3A has a mass of ∼0.04 $M_\odot$. By analyzing the Toomre Q parameter, we find the IRS3A circumstellar disk is gravitationally stable ($Q > 5$), while the IRS3B disk is consistent with a gravitationally unstable disk ($Q < 1$) between the radii ∼200–500 au. This coincides with the location of the spiral arms and the tertiary companion IRS3B-c, supporting the hypothesis that IRS3B-c was formed in situ via fragmentation of a gravitationally unstable disk.

Unified Astronomy Thesaurus concepts: Protostars (1302); Young stellar objects (1834)

1. Introduction

Star formation takes place in dense cores within molecular clouds (Shu et al. 1987), which are generally found within filamentary structures (André et al. 2014). The Perseus molecular cloud, in particular, hosts a plethora of young stellar objects (YSOs; Enoch et al. 2009; Sadavoy et al. 2014) and is nearby ($d \sim 288 \pm 22$ pc; e.g., Ortiz-León et al. 2018; Zucker et al. 2019), making its protostellar population ideal for high–spatial resolution studies. By observing these YSOs during the early stages of star formation, we can learn about how cores collapse and evolve into protostellar and/or protomultiple systems and how their disks may form into protoplanetary systems.

Protostellar systems have been classified into several groups following an evolutionary sequence: class 0, the youngest and most embedded objects characterized by low L_{bol}/L_{submm} ($<5 \times 10^{-3}$; Andre et al. 1993) and $T_{bol} \leqslant 70$ K; class I sources that are still enshrouded by an envelope that is less dense than the class 0 envelope, with $T_{bol} \leq 650$ K, flat spectrum sources, which are a transition phase between class I and class II; and class II objects, which have shed their envelope and consist of a pre-main-sequence star and a protoplanetary disk. Most stellar mass buildup is expected to occur during the class 0 and class I phases ($<5 \times 10^5$ yr; e.g., Lada 1987; Kristensen & Dunham 2018), because by the time the system has evolved to the class II stage, most of the mass of the envelope has been either accreted onto the disk/protostar or blown away by outflows (Arce & Sargent 2006; Offner & Arce 2014).

Studies of multiplicity in field stars have observed MFs of 63% for nearby stars (Worley 1962), 44%–72% for Sun-like stars (Abt 1983; Raghavan et al. 2010), 50% for F-G type nearby stars (Duquennoy & Mayor 1991), 84% for A-type stars (Moe & Di Stefano 2017), and 60% for pre-main-sequence stars (Mathieu 1994). These studies demonstrate the high frequency of stellar multiples and motivate the need for further multiplicity surveys toward young stars to understand their formation mechanisms.

Current theories suggest four favored pathways for forming multiple systems: turbulent fragmentation (on scales ∼1000s of au; e.g., Fisher 2004; Padoan & Nordlund 2004), thermal fragmentation (on scales ∼1000s of au; e.g., Offner et al. 2010; Boss & Keiser 2013), gravitational instabilities (GIs) within disks (on scales ∼100s of au; e.g., Adams et al. 1989; Stamatellos & Whitworth 2009; Kratter et al. 2010a), and/or loose dynamical capture of cores ($\sim 10^{4-5}$ au scales Bate et al. 2002; Lee et al. 2019). Additionally, stellar multiples may evolve via multibody dynamical interactions, which can alter their hierarchies early in the star formation process (Bate et al. 2002; Moeckel & Bate 2010; Reipurth & Mikkola 2012). In order to fully understand star

Table 1
Summary of Observations

Source	R.A. (J2000)	Decl. (J2000)	Config.[a]	Resolution	LAS[b]	Date (UT)	Calibrators (Gain, Bandpass, Flux)
L1448 IRS3B	03:25:36.382	30:45:14.715	C40-6	0.″12	1.″3	2016 October 1 and 4	J0336+3218,J0237+2848,J0238+1636
L1448 IRS3B	03:25:36.382	30:45:14.715	C40-3	0.″59	5.″6	2016 December 19	J0336+3218,J0237+2848,J0238+1636

Notes.
[a] C40-6 is extended; C40-3 is compact.
[b] LAS: largest angular scale.

formation and multiple-star formation, it is important to target the youngest systems to characterize the initial conditions.

The VLA Nascent Disk and Multiplicity (VANDAM) survey (Tobin et al. 2016b) targeted all known protostars down to 20 au scales within the Perseus molecular cloud using the Karl G. Jansky Very Large Array to better characterize protostellar multiplicity. They found the multiplicity fraction (MF) of class 0 protostars to be ∼57% (15–10,000 au scales) and ∼28% for close companions (15–1000 au scales), while for class I protostars, the MF for companions (15–10,000 au scales) is 23% and for close companions (15–1000 au scales) is 27%. This empirical distinction in MF motivates the need to observe class 0 protostars to resolve the dynamics before the systems evolve. It was during this survey that the multiplicity of L1448 IRS3B, a compact (∼230 au) triple system, was discovered. Tobin et al. (2016a) observed this source at 1.3 mm, resolving spiral arms and kinematic rotation signatures in $C^{18}O$, ^{13}CO, and H_2CO, with strong outflows originating from the IRS3B system.

L1448 IRS3B has a hierarchical configuration, which features an inner binary (separation 0.″25 ≈ 75 au, denoted -a and -b, respectively) and an embedded tertiary (separation 0.″8 ≈ 230 au, denoted -c). The IRS3B-c source is deeply embedded within a clump positioned within the IRS3B disk; thus we reference the still-forming protostar as IRS3B-c and the observed compact emission as a "clump" around IRS3B-c. Tobin et al. (2016b) found evidence for Keplerian rotation around the disks of IRS3B and IRS3A. They also found that the circum-triple disk was likely gravitationally unstable.

Theory suggests that during stellar mass assembly via disk accretion, fragmentation via GI may occur if the disk is sufficiently massive, cold, and rapidly accreting (Adams et al. 1989; Yorke & Bodenheimer 1999; Kratter et al. 2010b). Due to the scales of fragmentation, and ongoing infall, fragments likely turn into stellar or brown dwarf mass companions, and GI is a favored pathway for the formation of compact multisystems ($\lesssim$100 au). Since observations show that the youngest systems, like L1448 IRS3B, have higher disk masses than their more evolved counterparts (Tobin et al. 2020), we would also expect observational signatures of disk instability and fragmentation to be most prevalent at the class 0 stage.

The wide and compact protomultiple configurations of IRS3A and IRS3B contained within a single system provide a test bed for multiple star formation pathways to determine which theories best describe this system. Here we detail our follow-up observations to Tobin et al. (2016a) of L1448 IRS3B with the Atacama Large Millimeter/submillimeter Array (ALMA) in band 7, with 2× higher resolution and 6× higher sensitivity. We resolve the kinematics toward both IRS3B and IRS3A with much higher fidelity that the previous observations, enabling us to characterize the nature of the rotation in the disks, measure the protostar masses, and characterize the stability of both disks. We show our observations of this system and describe the data reduction techniques in Section 2, we discuss our empirical results and our use of molecular lines in Section 3, we further analyze the molecular line kinematics in Section 4, we further detail our models and the results in Section 5, and we interpret our findings in Section 6, where we discuss the implications of our empirical and model results and future endeavors. Section 7 concludes.

2. Observations

We observed L1448 IRS3B with ALMA in band 7 (879 μm) during cycle 4 in two configurations, an extended (C40-6) and a compact (C40-3) configuration, in order to fully recover the total flux out to ∼5″ angular scales in addition to resolving the structure in the disk. C40-6 was used on 2016 October 1 and 4 with 45 antennas. The baselines ranged from 15 to 3200 meters, for a total of 4495 s on source (8052 s total) for both executions. C40-3 was used on 2016 December 19 with 41 antennas. The baselines covered 15–490 m for a total of 1335 s on source (3098 s total).

The complex gain calibrator was J0336+3218, the bandpass calibrator was J0237+2848, and the flux calibrator was the monitored quasar J0238+1636. The observations were centered on IRS3B. IRS3A, the wide companion, is detected further out in the primary beam with a beam efficiency ∼60%. We summarize the observations in Tables 1 and 2 and further detail our observations and reductions in Appendix A.

It should also be noted there is possible line blending of $H^{13}CN$ ($J = 4 \rightarrow 3$) and SO_2 ($J = 13_{2,12} \rightarrow 12_{1,11}$) (Lis et al. 1997) (Table 2). The SO_2 line has an Einstein A coefficient of 2.4×10^{-4} s^{-1} with an upper level energy of 93 K, demonstrating that the transition line strength could be strong. SO_2 provides another shock tracer that could be present toward the protostars. We label $H^{13}CN$ and SO_2 together for the rest of this analysis to emphasize the possible line blending of these molecular lines. Additionally, the ^{12}CO and SiO emission primarily traces outflowing material, and analysis of these data is beyond the scope of this paper, but the integrated intensity maps of selected velocity ranges are shown in Appendices D.1 and D.2. The results of this analysis are summarized for each of the sources in Table 3.

3. Results

3.1. 879 μm Dust Continuum

The observations contain the known wide-binary system L1448 IRS3A and L1448 IRS3B and strongly detect continuum disks toward each protostellar system (Figures 1 and 2). We resolve the extended disk surrounding IRS3A (Briggs robust weight = 0.5: Figure 1, superuniform: Figure 3).

Table 2
Continuum and Spectral Line Data

	MFS Continuum[a]	^{12}CO	SiO[b]	H^{13}CN/SO$_2$[c]	H^{13}CO$^+$	C^{17}O	335.5 GHz Continuum
Rest. Freq. (GHz)	341.0	346.0	347.000030579	345.339756	346.998347	337.061104	335.5
Center Freq. (GHz)	341.0	346.778059	347.2698586	345.3520738	347.010582	337.0730133	335.4708304
Chan. Width (km/s)	2747.96	0.212	0.210	0.053	0.053	0.054	0.873
Num. Chan.	1	1920	1920	1920	1920	3840	1920
rms/chan. (mJy)	0.069	4.0	0.5	4.5	4.5	3.7	⋯
Integr. (Jy) IRS3B[d]	1.5	512.7,809.8[e]	7.8, 3.5[e]	0.2, 0.1[e]	2.6, 4.1[e]	2.9, 3.2[e]	⋯
Integr. (Jy) IRS3A[d]	0.2	3.16,67.6[e]	0,0[e]	2.3, 2.7[e]	0.2, 0.4[e]	0.1, 0.1[e]	⋯
Synth. Beam[f]	0.″11 × 0.″05	0.″19 × 0.″11	0.″85 × 0.″52	0.″22 × 0.″14	0.″21 × 0.″13	0.″21 × 0.″13	0.″21 × 0.″13
Briggs Robust	0.5	0.5	0.5	0.5	0.5	0.5	⋯
Taper (kλ)	⋯	⋯	⋯	1000	1500	1500	⋯

Notes. The setup of the correlator for the observations.
[a] Multifrequency synthesis (MFS) utilizing the extracted emission from line free spectral channels.
[b] SiO was tuned incorrectly for the C40-6 observations.
[c] The H^{13}CN line is blended with the SO_2 line (345.3385377 GHz) and has a velocity separation of ∼1.06 km s^{-1}.
[d] The integrated flux density for the source, measured by the integrated full emission whose origin is the source. In the case of continuum emission, this is given in Jy; in the case of molecular line emission this is given in Jy km s^{-1}.
[e] The molecular line emission is given as the total integrated flux (Jy km s^{-1}) for the blue and red Doppler-shifted emission, denoted blue and red, respectively.
[f] The synthesized beam size is provided from the *clean* task for the molecular lines (or continuum for the MFS column) using the Briggs robust weighing parameter of 0.5 during image reconstruction.

Table 3
Source Properties

Source	R.A. (J2000)	Decl. (J2000)	Inc.[a] (°)	P.A.[b] (°)	Outflow?	V_{sys} (km s^{-1})
IRS3B-ab	03:25:36.317	30:45:15.005	45	28	Joint	4.75
IRS3B-c	03:25:36.382	30:45:14.715	27	21	Yes	4.75
IRS3A	03:25:36.502	30:45:21.859	69	133	No	5.2

L_{bol} ($L_\odot$)	M_{dust} ($M_\odot$)	FWHM$_{Dust}$[c] Major Axis (″, au)	FWHM$_{Dust}$[c] Minor Axis (″, au)	FWHM$_{Gas}$[c] Major Axis (″, au)	FWHM$_{Gas}$[c] Minor Axis (″, au)	$\langle T_0 \rangle$ (K)	⟨ Optical Depth ⟩
13.0[e]	0.29	1.73 ± 0.05, 498 ± 14	1.22 ± 0.04, 351 ± 12	2.38 ± 0.09, 685 ± 26	2.25 ± 0.08, 648 ± 23	40	0.34
…[d]	0.07	0.28 ± 0.05, 81 ± 14	0.25 ± 0.04, 72 ± 12	⋯	⋯	55	2.14
14.4[e]	0.04	0.70 ± 0.02, 202 ± 6	0.25 ± 0.01, 72 ± 3	0.52 ± 0.08, 150 ± 23	0.42 ± 0.07, 121 ± 20	51	0.57

Notes. Summary of the empirical parameters based on the observations of the system. The sizes were derived from a 2D Gaussian fit to the continuum and moment 0 emission maps, directly to the visibilities. IRS3B-c is blended with the underlying disk continuum, and estimates here are extracted from a 2D Gaussian fit with a zero-level offset to preserve the underlying disk flux and are discussed in Appendix F.
[a] Inclination is defined such that 0° is a face-on disk.
[b] Position angle is defined such that at 0°, the major axis of the disk is aligned north, and the angle corresponds to east of north.
[c] The circumstellar disks surround IRS3B and IRS3A are ellipsoidal in the dust continuum and molecular line emission.
[d] The bolometric luminosity is not known at this time.
[e] The bolometric luminosity is scaled to a distance of 288 pc from Tobin et al. (2016b).

3.1.1. IRS3B

We resolve the extended circum-multiple disk of IRS3B and the spiral arm structure that extends asymmetrically to ∼600 au north–south in diameter. Figure 2 shows a zoom-in on the IRS3B circumstellar disk, exhibiting clear substructure. Furthermore, we observe the three distinct continuum sources within the disk of IRS3B as identified by Tobin et al. (2016a), but with our superior resolution and sensitivity (∼2× higher), our observations are able to marginally resolve smaller-scale detail closer to the inner pair of sources, IRS3B-a and -b (Figure 2). We now constrain the origin point of the two spiral arm structures. Looking toward IRS3B-ab, we notice a decline in the disk continuum surface brightness in the inner region, northeast of IRS3B-ab. We also observe a "clump" ∼50 au east of IRS3B-b. However, given that this feature is located with apparent symmetry to IRS3B-a, it is possible that the two features ("clump" and IRS3B-a) are a part of an inner disk structure as there appears a slight deficit of emission located between them ("deficit"), while IRS3B-b is just outside of the inner region.

3.1.2. IRS3B-ab

To best determine the position angle and inclination of the circum-multiple disk, we first have to remove the tertiary source that is embedded within the disk using the *imfit* task in CASA by fitting two 2D Gaussians with a constant emission offset (detailed fully in Appendix F). We fit the semimajor and semiminor axis of the IRS3B-ab disk with a 2D Gaussian using the task *imfit* in CASA. To fit the general shape of the disk and not fit the shape of the spiral arms, we smooth the underlying

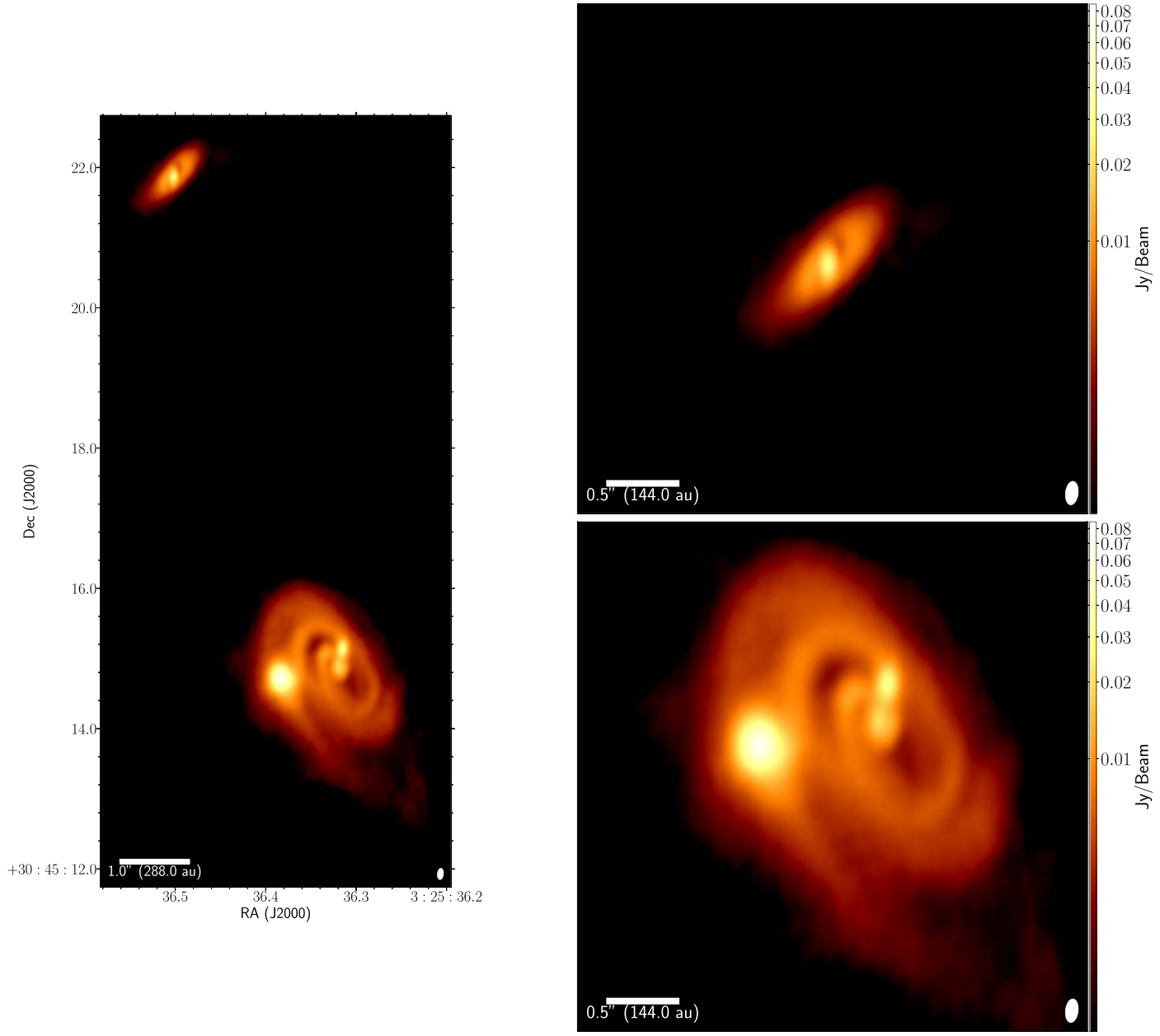

Figure 1. ALMA 879 μm continuum observations of the triple protostellar system L1448 IRS3B and its wide companion IRS3A (left). The right panels are $\sim$2$\times$ zoom-ins on IRS3B and IRS3A. The top right image shows the wide companion, IRS3A ($d \sim 7\farcs9 \approx 2300$ au), featuring possible spiral structure. The bottom right image zooms in on the protomultiple system, IRS3B. The inner binary is separated by $0\farcs25$ (75 au) and has a spiral circumbinary disk with the embedded source $\sim 0\farcs8$ (230 au) away from the binary within one of the arms. The beam size of each panel is shown in lower right ($0\farcs11 \times 0\farcs05$).

disk structure (taper the *uv* visibilities at 500 kλ during deconvolution using the CASA *clean* task), yielding a more appropriate image for single 2D Gaussian fitting.

From this fit, we recovered the disk size, inclination, and position angle, which are summarized in Table 3. The protostellar disk of IRS3B has a deconvolved major axis and minor axis FWHM of $1\farcs73 \pm 0\farcs05$ and $1\farcs22 \pm 0\farcs04$ (497 ± 17 au $\times$ 351 ± 12 au), respectively. This corresponds to an inclination angle of $45\fdg0^{+2.2}_{-2.2}$ assuming the disk is symmetric and geometrically thin, where an inclination angle of 0° corresponds to a face-on disk. We estimate the inclination angle uncertainty to be as much as 25% by considering the southeast side of the disk as asymmetric and more extended. The position angle of the disk corresponds to 28° ± 4° east of north.

3.1.3. IRS3B-c

In the process of removing the clump around the tertiary companion IRS3B-c, we construct a model image of this clump that can be analyzed through the same methods. We recover a deconvolved major axis and minor axis FWHM of $0\farcs28 \pm 0\farcs05$ and $0\farcs25 \pm 0\farcs04$ (80 ± 17 au $\times$ 71 ± 12 au), respectively, corresponding to a radius $\sim$40 au (assuming the disk is symmetric). This corresponds to an inclination angle of $27\fdg0^{+19}_{-19}$, and we fit a position angle of 21° ± 1° east of north. We note the inclination estimates for IRS3B-c may not be realistic since the internal structure of the source (oblate, spherical, etc.) cannot be constrained from these observations; thus the reported angles are assuming a flat, circular internal structure, similar to a disk.

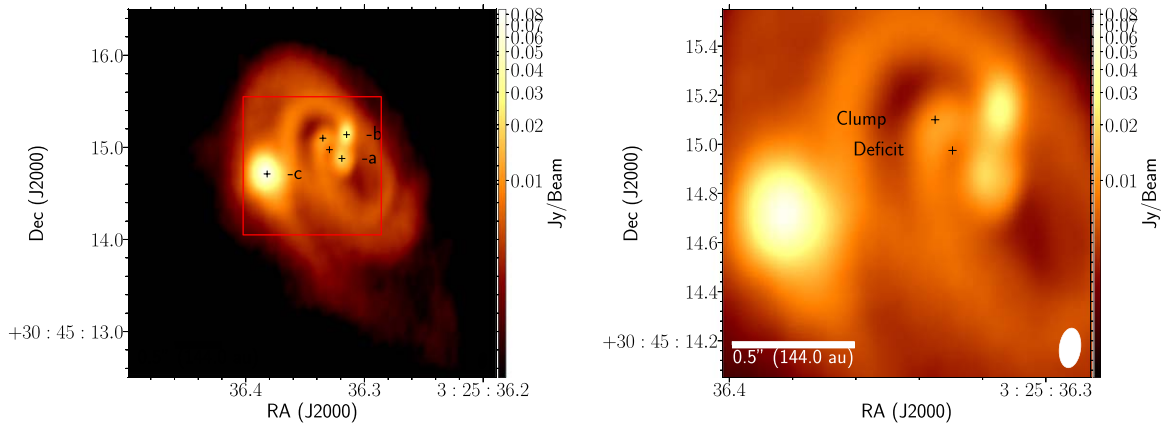

Figure 2. ALMA 879 μm continuum observations of the triple protostellar system L1448 IRS3B with the difference continuum sources marked. The left colored image is zoomed in on IRS3B and is plotting with a log color stretch. The inner binary is separated by $0\farcs25$ (75 au) and has a circumbinary disk with spiral structure, and the tertiary is separated from the binary by $\sim 0\farcs8$ (230 au) within one of the arms. The "protostars" are the continuum positions previously discovered in Tobin et al. (2016a), while the "clump" is a new feature, resolved in these observations. The "deficit" indicates the location of depression of flux between IRS3B-a and the "clump." This is discussed in Sections 3.1 and 6. The beam size of each panel is shown in the lower right ($0\farcs11 \times 0\farcs05$ using a Briggs robust parameter of 0.5).

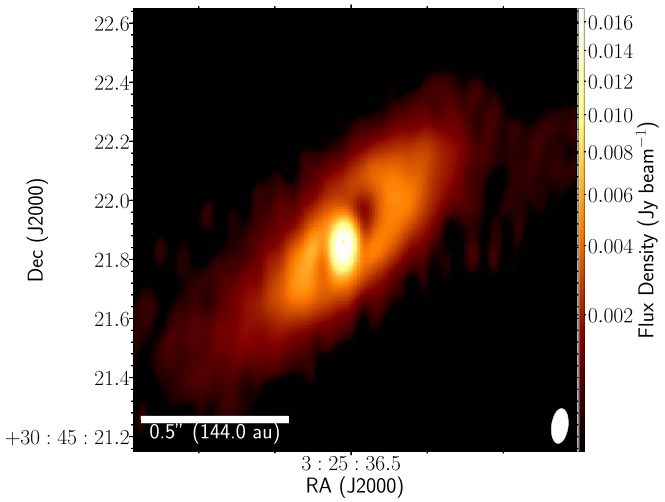

Figure 3. Continuum (879 μm) image of IRS3A, reconstructed with the *superuniform* weighing scheme, half of the cell size, and zoomed 2× from the images in Figure 1 to highlight the possible spiral substructure.

3.1.4. IRS3A

The protostellar disk of IRS3A has an FWHM radius of ~100 au and has a deconvolved major axis and minor axis of $0\farcs69^{+0.01}_{-0.01}$ and $0\farcs25^{+0.1}_{-0.1}$ (197 ± 3 au × 72 ± 3 au), respectively. This corresponds to an inclination angle of $68\fdg6 \pm 1\fdg2$ assuming the disk is axially symmetric. The position angle of the disk corresponds to 133° ± 1° east of north. We marginally resolve two emission deficits one beamwidth off IRS3A, along the major axis of the disk. The potential spirals appear to originate along the minor axis of the disk; however, due to the reconstructed beam elongation along the minor axis of the disk, we cannot fully resolve the substructure of the disk around IRS3A, limiting the characterization that we can perform on it.

3.2. Disk Masses

The traditional way to estimate the disk mass is via the dust component that dominates the disk continuum emission at millimeter wavelengths. If we make the assumption that the disk is isothermal, optically thin, without scattering, and the dust and gas are well mixed, then we can derive the disk mass from the equation

$$M_{\rm dust} = \frac{D^2 F_\lambda}{\kappa_\lambda B_\lambda(T_{\rm dust})}, \quad (1)$$

where D is the distance to the region (288 pc), F_λ is the flux density, κ_λ is the dust opacity, B_λ is the Planck function for a dust temperature, and $T_{\rm dust}$ is taken to be the average temperature of a typical protostar disk. The κ_λ at $\lambda = 1.3$ mm was adopted from dust opacity models with value of 0.899 cm^2 g^{-1}, typical of dense cores with thin icy mantles (Ossenkopf & Henning 1994). We then appropriately scale the opacity:

$$\kappa_{0.879\ \rm mm} = \kappa_{1.3\ \rm mm} \times \left(\frac{1.3\ \rm mm}{0.879\ \rm mm}\right)^{\beta}, \quad (2)$$

assuming $\beta = 1.78$. We note that β values typical for protostars range from 1 to 1.8 (Kwon et al. 2009; Sadavoy 2013). If we assume significant grain growth has occurred, typical of more evolved protoplanetary disks like that of Andrews et al. (2009), we would then adopt a $\kappa_{0.899\ \mu\rm m} \approx 3.5$ cm^2 g^{-1} and $\beta = 1$, which would lower our reported masses by a factor of 2.

The assumed luminosities of the sources are 13.0 $L_\odot$ and 14.4 $L_\odot$ for IRS3B and IRS3A at a distance of 300 pc, respectively (8.3 $L_\odot$ and 9.2 $L_\odot$ for IRS3B and IRS3A, respectively at 230 pc; Tobin et al. 2016b). We note that in the literature there are several luminosity values for IRS3B, differing from our adopted value by a factor of a few. Reconciling this is outside of the scope of this paper, but the difference could arise from source confusion in the crowded field and differences in spectral energy distribution modeling.

We adopt a $T_{\rm dust} \approx 40$ K for the IRS3B disk dust temperatures from the equation $T_{\rm dust} = 30\ {\rm K} \times (L_*/L_\odot)^{1/4}$, which is comparable to temperatures derived from protostellar models (43 K: Tobin et al. 2013) and larger than temperatures assumed for the more evolved protoplanetary disks (25 K: Andrews et al. 2013). The compact clump around IRS3B-c has a peak brightness temperature of 55 K. Thus we adopt a $T_{\rm dust} = 55$ K since the emission may be optically thick ($T_{\rm dust} \sim T_B$). We determine the peak brightness temperature of this clump by first converting the

dust continuum image from Jy into K via the Rayleigh-Jean's Law.[12] We adopt a $T_{\rm dust} = 51$ K for the IRS3A source.

If we assume the canonical interstellar medium (ISM) gas-to-dust mass ratio of 100:1 (Bohlin et al. 1978), we estimate the total mass of the IRS3B-ab disk (IRS3B-c subtracted) to be 0.29 $M_\odot$ for $\kappa_{0.879\,\rm mm} = 1.80\,{\rm cm^2\ g^{-1}}$, $T_{\rm dust} \approx 40$ K (Tobin et al. 2019), and $F_\lambda \approx 1.51$ Jy. We note that the dust-to-gas ratio is expected to decrease as disks evolved from class 0 to class II (Williams & Best 2014), but for such a young disk, we expect it to still be gas rich and therefore have a gas-to-dust ratio more comparable with the ISM. We estimate 0.07 $M_\odot$ to be associated with the circumstellar dust around IRS3B-c, from this analysis, for a $T_{\rm dust} = 55$ K. We perform the same analysis toward IRS3A and arrive at a disk mass estimate of 0.04 $M_\odot$, for a $T_{\rm dust} = 51$ K and $F_\lambda \approx 0.19$ Jy.

The dust around the tertiary source, IRS3B-c, is compact, and it is the highest peak intensity source in the system; thus the optical depth needs to be constrained. An optically thick disk will be more massive than what we calculate, while an optically thin disk will be more closely aligned with our estimates. We calculate the average deprojected, cumulative surface density from the mass and radius provided in Table 3 and determine the optical depth via

$$\tau_{0.879\,\rm mm} = \kappa_{0.879\,\rm mm}\Sigma = \frac{D^2 F_\lambda}{\pi R_{\rm disk}^2 B_\lambda(T_{\rm dust})}$$

from Tobin et al. (2016a). The dust surrounding the tertiary source has an average dust surface density (Σ) of $\sim$2.6 g cm^{-2} and an optical depth (τ) of $\sim$2.14, indicative of being optically thick, while IRS3B-ab (IRS3B-c clump subtracted) is not optically thick if we assume dust is equally distributed throughout the disk with an average dust surface density of $\sim$0.17 g cm^{-2} and an optical depth of 0.34. However, since spiral structure is present, these regions of concentrated dust particles are likely much more dense. L1448 IRS3A has an average dust surface density of 0.32 g cm^{-2} and an optical depth of 0.57. Optically thick emission indicates that our dust continuum mass estimates are likely lower limits for the mass enclosed in the clump surrounding IRS3B-c, while the IRS3B-ab circum-multiple disk and the IRS3A circumstellar disk are probably optically thin except for the inner regions.

An effect that could impact our measurements of disk masses and surface densities is scattering. Scattering reduces the emission of optically thick regions of the disk so they appear optically thin, thus causing an underestimate of the optical depth. Zhu et al. (2019) showed that in the lower limit of extended (>100 au) disks, this effect underestimates the disk masses by a factor of 2. However, toward the inner regions, this effect might be enhanced to factors >10. Sierra & Lizano (2020) show that for wavelengths $\sim$870 and 100 μm size particles, only a $\Sigma \approx 3.2$ (g cm^{-2}) is needed for the particles to be optically thick. Thus our masses could be several factors higher.

3.3. Molecular Line Kinematics

Additionally, we observe a number of molecular lines (^{12}CO, SiO, H^{13}CO$^+$, H^{13}CN/SO$_2$, C^{17}O) toward IRS3B and IRS3A to resolve outflows, envelope, and disk kinematics, with the goal of disentangling the dynamics of the systems. We summarize the observations of each of the molecules below and provide a more rigorous analysis toward molecules tracing disk kinematics. While outflows are important for the evolution and characterization of YSOs, the analysis of these complex structures is beyond the scope of this paper because we are focused on the disk and envelope. We find ^{12}CO and SiO emission primarily traces outflows; H^{13}CO$^+$ emission traces the inner envelope; H^{13}CN/SO$_2$ emission traces energetic gas, which can take the form of outflow launch locations or inner disk rotations; and C^{17}O primarily traces the disk. Nondisk/envelope tracing molecular lines (^{12}CO and SiO) are discussed in Appendix D.

We construct moment 0 maps, which integrate the data cube over the frequency axis, to reduce the 3D nature of data cubes to 2D images. These images show spatial locations of strong emission and deficits. To help preserve some frequency information from the data cubes, we integrated at specified velocities to separate the various kinematics in these systems. However, when integrating over any velocity ranges, we do not preserve the full velocity information of the emission; thus we provide spectral profiles of C^{17}O emission toward the IRS3B-ab, IRS3B-c, and IRS3A sources in Appendix E.

3.3.1. $C^{17}O$ Line Emission

The C^{17}O emission (Figures 4–6) appears to trace the gas kinematics within the circumstellar disks because the emission is largely confined to the scales of the continuum disks for both IRS3B and IRS3A, appears orthogonal to the outflows, and has a well-ordered data cube indicative of rotation (Figure 6). C^{17}O is a less abundant molecule (ISM [^{12}CO]/[C^{17}O] $\approx$ 1700:1; e.g., Wilson & Rood 1994) isotopologue of ^{12}CO (ISM [H$_2$]/[^{12}CO] $\approx 10^4$:1; e.g., Visser et al. 2009) and thus traces gas closer to the disk midplane. Toward IRS3B, the emission extends out to $\sim$1.″8 ($\sim$530 au), further than the continuum disk ($\sim$500 au), and has a velocity gradient indicative of Keplerian rotation. Toward IRS3A, the emission is much fainter, however, from the moment 0 maps, C^{17}O still appears to trace the same region as the continuum disk.

3.3.2. $H^{13}CO^+$ Line Emission

The H^{13}CO$^+$ emission (Figures 7 and 8) detected within these observations probes large-scale structures (>5″), much larger than the size of the continuum disk of IRS3B, and scales $\sim$1.″5 toward IRS3A. For IRS3B, the emission structure is fairly complicated, with multiple emission peaks near line center and emission deficits near the sources IRS3B-ab+c, while appearing faint toward IRS3A. The data cube appears kinematically well ordered, indicating possible rotating structures. Previous studies suggested HCO+ observations are less sensitive to the outer envelope structure, probing densities $\geqslant 10^5$ cm^{-3} and temperatures >25 K (Evans 1999). However, follow-up surveys (Jørgensen et al. 2009) found this molecule to primarily trace the outer circumstellar disk and inner envelope kinematics and were unable to observe the disks of class 0 protostars from these observations alone. Jørgensen et al. (2009) postulated that in order to disentangle dynamical structures on <100 au scales, a less abundant or more optically thin tracer (like that of H^{13}CO$^+$) would be required with high resolutions. However, this molecular line, as shown in the

[12] ($T = 1.222 \times 10^3 \frac{\rm I\ mJy\ beam^{-1}}{(\nu\ \rm GHz)^2(\theta_{major}\ arcsec)(\theta_{minor}\ arcsec)}$ K, Wilson et al. 2009).

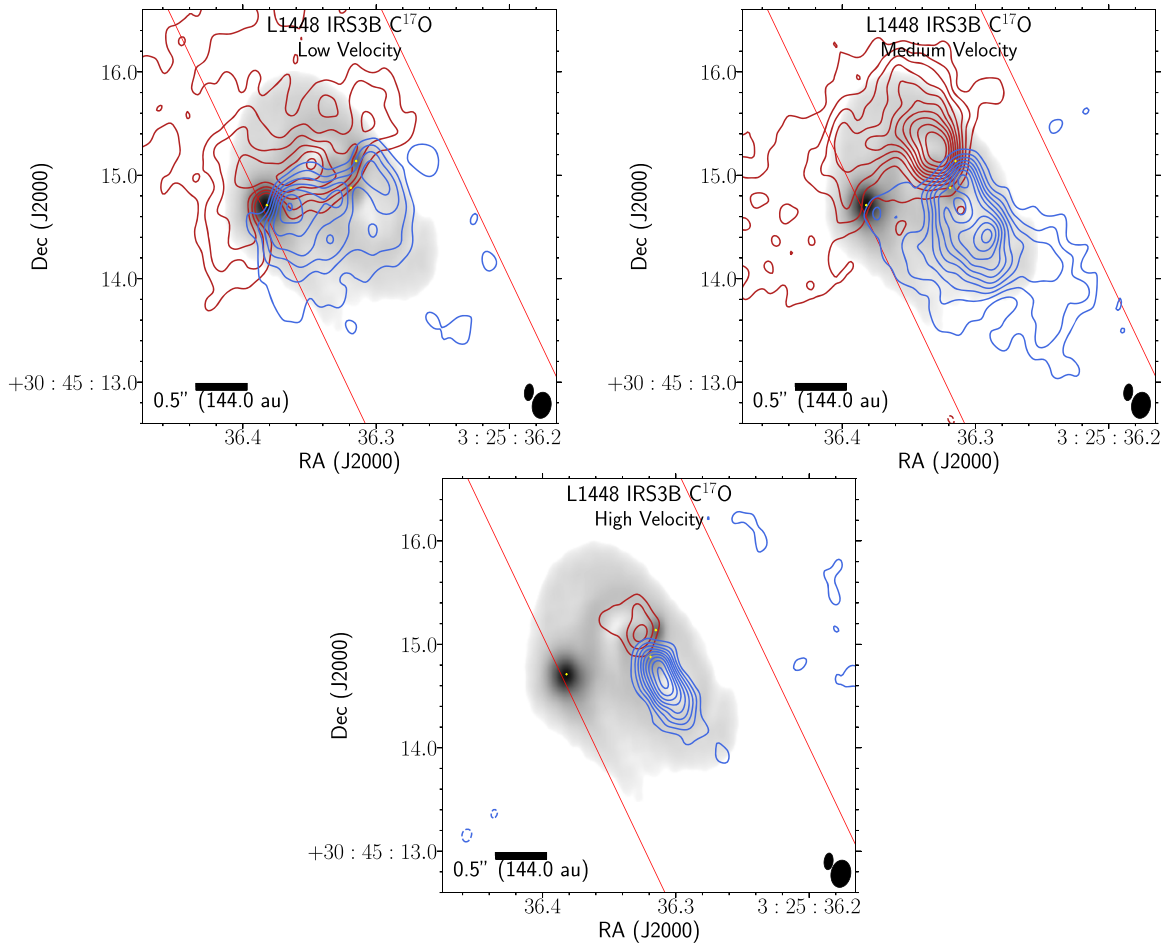

Figure 4. $C^{17}O$ integrated intensity maps toward IRS3B over a selected range of velocities overlaid on continuum (gray scale). The $C^{17}O$ emission traces the rotating gas within the disk via Doppler-shifted emission. The panels correspond to low-, medium-, and high-velocity ranges. The following panel descriptions will be noted red (blue), corresponding to the Doppler shifted emission. Negative contours are not present in these integrated intensity maps; however, at the location of IRS3B-c, there is strong absorption that is evident in the high spectral resolution data cube but is not represented here. The red lines indicate the region extracted for PV diagram construction, along the position angle of the major axis. Low velocity: velocity range starts at 4.68 → 5.67 km s^{-1} (3.58 → 4.68 km s^{-1}) and contours start at 8σ (8σ) and iterate by 3σ (3σ) with the 1σ level starting at 0.0023 (0.0025) Jy beam^{-1} for the red (blue) channels, respectively. Medium velocity: velocity range starts at 5.67 → 6.66 km s^{-1} (2.48 → 3.58 km s^{-1}) and contours start at 3σ (5σ) and iterate by 3σ (3σ) with the 1σ level starting at 0.002 (0.0016) Jy beam^{-1} for the red (blue) channels, respectively. High velocity: velocity range starts at 6.66 → 7.65 km s^{-1} (1.27 → 2.48 km s^{-1}) and contours start at 5σ (5σ) and iterate by 3σ (3σ) with the 1σ level starting at 0.0018 (0.0012) Jy beam^{-1} for the red (blue) channels respectively. The $C^{17}O$ synthesized beam (0.″21 × 0.″13) is the bottom rightmost ellipse on each of the panels, and the continuum synthesized beam (0.″11 × 0.″05) is offset diagonally.

integrated intensity map of $H^{13}CO^+$ (Figures 7 and 8), traces scales much larger than the continuum or gaseous disk of IRS3B and IRS3A and thus is likely tracing the inner envelope.

3.3.3. $H^{13}CN$ Line Emission

The $H^{13}CN/SO_2$ emission (Figures 9 and 10) is a blended molecular line, with a separation of 1 km s^{-1} (Table 2). The integrated intensity maps toward IRS3B appear to trace an apparent outflow launch location from the IRS3B-c protostar (Figure 9) based on the spatial location and parallel orientation to the outflows. The $H^{13}CN/SO_2$ emission toward IRS3B is nearly orthogonal to the disk continuum major axis position angle and indicates that the emission toward IRS3B is tracing predominantly SO_2 and not $H^{13}CN$.

4. Keplerian Rotation

To determine the stability of the circumstellar disks around IRS3B and IRS3A, the gravitational potentials of the central sources must be constrained. The protostars are completely obscured at $\lambda < 3\ \mu$m, rendering spectral typing impossible, and kinematic measurements of the protostar masses from disk rotation are required to characterize the protostars themselves. Assuming the gravitational potential is dominated by the central protostellar source(s), one would expect the disk to follow a Keplerian rotation pattern if the rotation velocities are large enough to support the disk against the protostellar gravity. These Keplerian motions will be observed as Doppler shifts in the emission lines of molecules due to their relative motion within the disk. Well-resolved disks with Keplerian rotation are observed as the characteristic "butterfly" pattern around the central gravitational potential: high-velocity emission at small radii to low-velocity emission at larger radii and back to high-velocity emission at small radii on opposite sides of the disk (e.g., Rosenfeld et al. 2013; Pinte et al. 2018a).

4.1. PV Diagrams

To analyze the kinematics of these sources, we first examine the moment 0 (integrated intensity) maps of the red and blue Doppler-shifted $C^{17}O$ emission to determine whether the

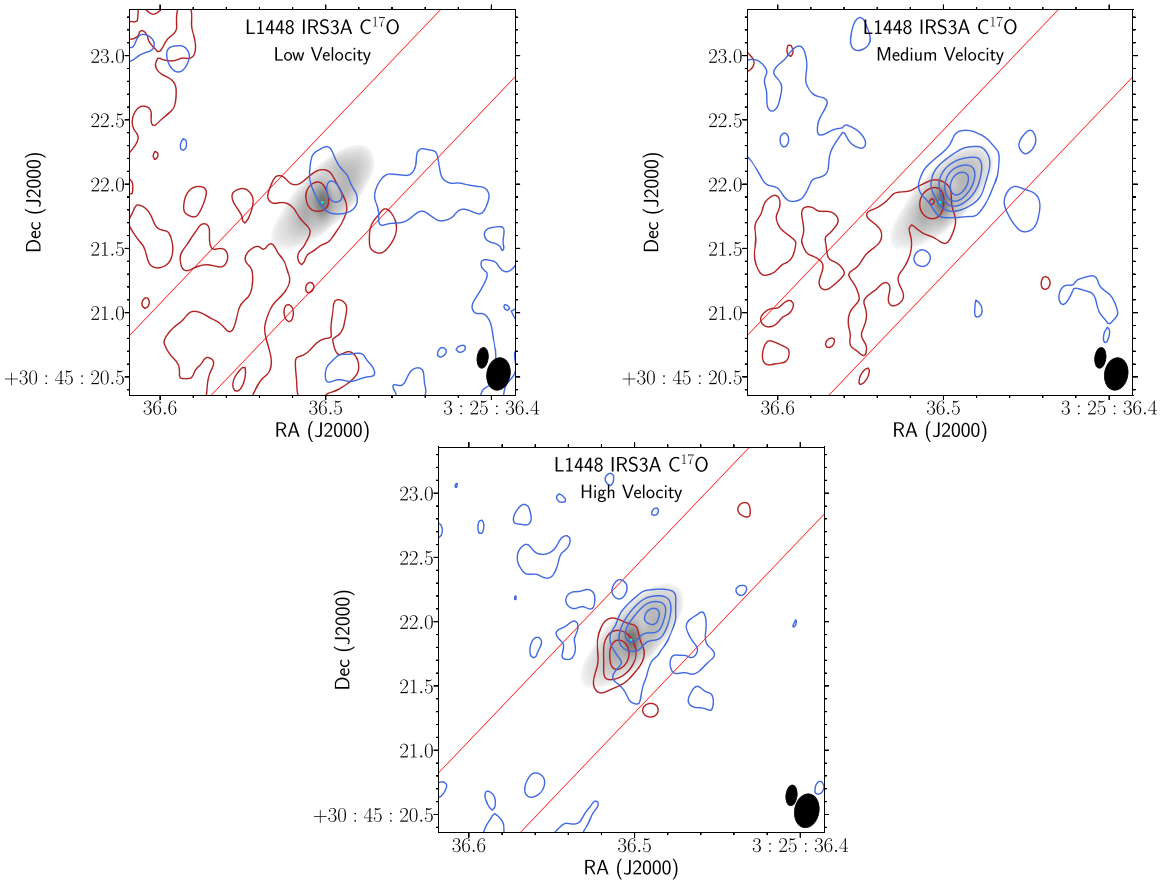

Figure 5. $C^{17}O$ integrated intensity maps toward IRS3A over a selected range of velocities overlaid on continuum (gray scale). The $C^{17}O$ emission exhibits a velocity gradient across the continuum emission. However, the signal-to-noise ratio (S/N) is low in comparison with IRS3B. The panels correspond to low-, medium-, and high-velocity ranges. The following panel descriptions will be noted red (blue), corresponding to the Doppler shifted emission. The red lines indicate the region extracted for PV diagram construction, along the position angle of the major axis. Low velocity: velocity ranges 5.2 → 6.5 km s^{-1} (4.1 → 5.2 km s^{-1}), contours start at 3σ (3σ) and iterate by 3σ (3σ) with the 1σ level starting at 0.0023 (0.0025) Jy beam^{-1} for the red (blue) channels, respectively. Medium velocity: velocity ranges 6.5 → 7.4 km s^{-1} (3.0 → 4.1 km s^{-1}), contours start at 3σ (3σ) and iterate by 3σ (3σ) with the 1σ level starting at 0.002 (0.0016) Jy beam^{-1} for the red (blue) channels, respectively. High velocity: velocity ranges 7.4 → 8.6 km s^{-1} (1.8 → 3.0 km s^{-1}), contours start at 3σ (3σ) and iterate by 3σ (3σ) with the 1σ level starting at 0.0018 (0.0012) Jy beam^{-1} for the red (blue) channels, respectively. The $C^{17}O$ synthesized beam (0.″21 × 0.″13) is the bottom rightmost ellipse on each of the panels, and the continuum synthesized beam (0.″11 × 0.″05) is offset diagonally.

emission appears well ordered (Figure 4) and consistent with $H^{13}CO^+$ (Figure 7). We then examine the sources using a PV diagram, which collapses the 3D nature of these data cubes (R.A., decl., velocity) into a 2D spectral image. We specify the number of integrated pixels across the minor axis to limit bias from the large-scale structure of the envelope and select emission originating from the disk. This allows for an estimation of several parameters via examining the respective Doppler-shifted components.

4.1.1. IRS3B

The PV diagrams for IRS3B are generated over a 105 pixel (2.″1) width strip at a position angle 28°. The PV diagram velocity axis is centered on the system velocity of 4.8 km s^{-1} (Tobin et al. 2016a) and spans ±5 km s^{-1} on either side, while the position axis is centered just off of the inner binary, determined to be the kinematic center, and spans 5″ (∼1500 au) on either side.

$C^{17}O$ appears to trace the gas within the disk of IRS3B on the scale of the continuum disk (Figure 4). It is less abundant and therefore less affected by outflow emission. We use it as a tracer for the kinematics of the disk (PV diagram indicating Keplerian rotation; Figure 11). The $C^{17}O$ emission extends to radii beyond the continuum disk, likely extending into the inner envelope of the protostar, while the $H^{13}CO^+$ emission (Figure 7) appears to trace larger-scale emission surrounding the disk of IRS3B and emission within the spatial scales of the disk has lower intensity. This is indicative of emission from the inner envelope as shown by the larger angular scales the emission extends to with respect to $C^{17}O$ ($H^{13}CO^+$ PV diagram; Figure 12). Finally, the blended molecular line, $H^{13}CN/SO_2$, appears to trace shocks in the outflows and not the disk kinematics for IRS3B. For these reasons, we do not plot the PV diagram of $H^{13}CN/SO_2$.

4.1.2. IRS3A

The PV diagrams for IRS3A are generated with a 31 pixel (0.″62) width strip at a position angle 133°. $C^{17}O$ is faint and diffuse toward the IRS3A disk (Figure 13) but still traces a velocity gradient consistent with rotation (Figure 5) and has a well-ordered PV diagram (Figure 13). $H^{13}CN/SO_2$ (Figure 10) appears to trace the kinematics of the inner disk due to the compactness of the emission near the protostar and the appearance within the disk plane (Figure 14). The velocity cut is centered on the system velocity of 5.4 km s^{-1} and spans 6.2 km s^{-1} on either side. The emission from the blended $H^{13}CN/SO_2$ is likely dominated by $H^{13}CN$ instead of SO_2, due

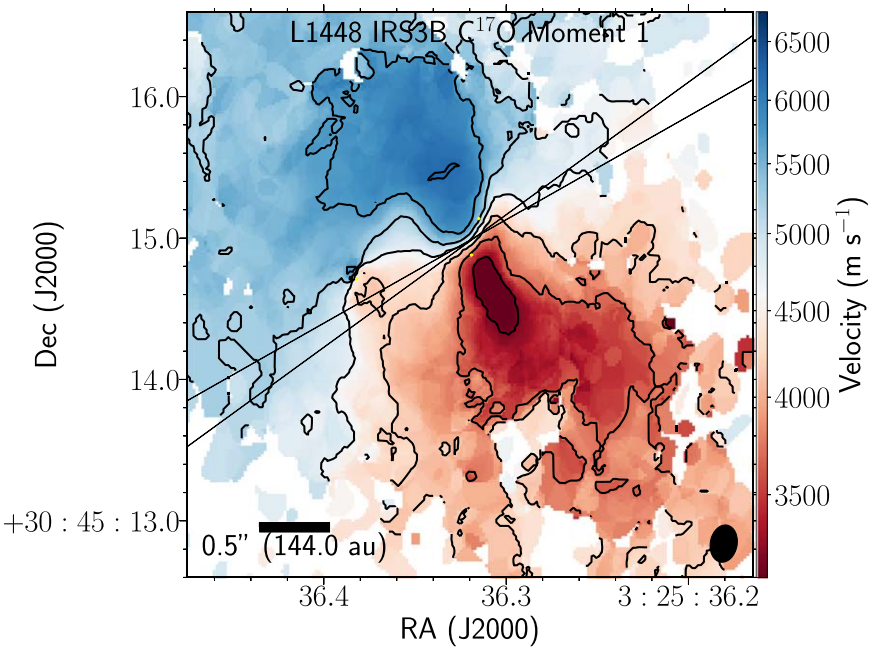

Figure 6. $C^{17}O$ velocity-weighted integrated intensity maps toward IRS3B and IRS3A over a selected range of velocities (1.27 → 7.65 km s^{-1}) The $C^{17}O$ emission appears well ordered across the semimajor axis. The contours denote the 0.5 km s^{-1} velocity offsets from system velocity of 4.8 km s^{-1}. The yellow markers indicate the three continuum sources. The black lines indicate the position angle of the minor disk estimates as given by the *pdspy* fitting routine in Table 4, of $90 + 26.7^{+1.8}_{-2.9}$°. The $C^{17}O$ synthesized beam ($0\farcs21 \times 0\farcs13$) is the bottom rightmost ellipse.

Table 4
PV Diagram Fitting

Source	Center R.A. (″)	Center Decl. (″)	Inclination (°)	Position Angle (°)	Stellar Mass ($M_\odot$)	Velocity (km s^{-1})
IRS3B	$03^h25^m36\overset{s}{.}317$	30°45′15.″005	45	29	$1.15^{+0.09}_{-0.09}$	4.8
IRS3B-c	$03^h25^m36\overset{s}{.}382$	30°45′14.″715	…	…	<0.2[a]	…
IRS3A	$03^h25^m36\overset{s}{.}502$	30°45′21.″859	69	125	1.4[b]	5.4

Notes. Summary of PV diagram stellar parameter estimates with 3σ confidence interval of the best-fit walkers generated from emcee. The inclination and position angle estimates are provided by 2D Gaussian fitting of the *uv*-truncated data and are further confirmed with the PV diagram analysis.

[a] The upper limit for IRS3B-c of <0.2 $M_\odot$ is derived from its apparent lack of significant influence on the disk kinematics within its immediate proximity. Furthermore, we estimate from the dust emission that the mass of the gas and dust clump surrounding the protostar is ∼0.07 $M_\odot$. So the combined mass of the clump and protostar must be <0.2 $M_\odot$. Figure 17 shows the mass limit estimates of the tertiary of the source, with emission outside of the dotted lines indicating additional mass if perturbing the disk.

[b] IRS3A, was marginally resolved, and no sufficient numeric fits could be achieved with simple PV diagram fitting. These estimates are provided by fitting the curve by eye and are not designated to be the final results; they simply provide further constraints for the priors for the more rigorous kinematic modeling.

to the similar system velocity that is observed. SO_2 would have ∼1.05 km s^{-1} offset, which is not observed in IRS3A.

Similar to IRS3B, the $H^{13}CO^+$ emission likely traces the inner envelope, indicated in Figure 8, as it extends well beyond the continuum emission but still traces a velocity gradient consistent with rotation (Figure 15). The circumstellar disk emission is less resolved, however, due to the compact nature of the source and has lower sensitivity to emission because it is located ∼8″ (beam efficiency ∼60%) from the primary beam center.

4.2. Protostar Masses: Modeling Keplerian Rotation

The kinematic structure, as evidenced by the blue- and redshifted integrated intensity maps (e.g., Figures 4 and 5), indicates rotation on the scale of the continuum disk. The disk red- and blueshifted emission are oriented along the disk major axis and not along the disk minor axis, which would be expected if the emission was contaminated by outflow kinematics. We first determined the protostellar mass by analyzing the PV diagram to determine regions indicative of Keplerian rotation. We summarize the results of our PV mass fitting in Table 4. PV diagram fitting provides a reasonable measurement of protostellar masses in the absence of a more rigorous modeling approach. The Keplerian rotation–velocity formula, $V(R) = (GM/R)^{0.5}$, allows several system parameters to be constrained: system velocity, kinematic center position, and protostellar mass. (There is a degeneracy between mass determination and the inclination angle of the Keplerian disk.) We account for inclination in fitting the mass using the constraint from the major and minor axis ratio of the continuum emission.

4.2.1. IRS3B-ab

When calculating the gravitational potential using kinematic line tracers, one must first define the position of the center of

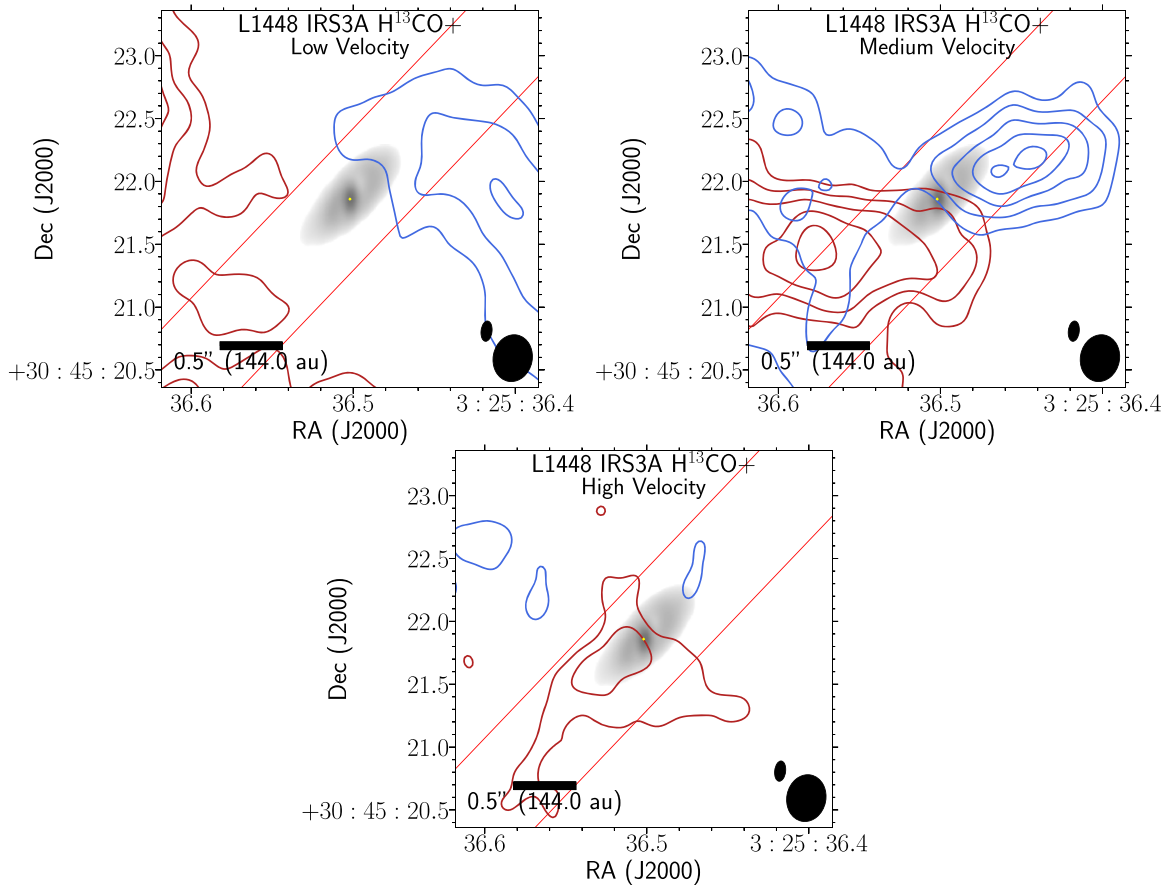

Figure 7. $H^{13}CO^+$ integrated intensity maps toward IRS3B over a selected range of velocities overlaid on continuum (gray scale). The top row spatial scale is set to match those of Figure 4, and the bottom row scale is set to encapsulate the entire IRS3B system, to better demonstrate the spatial scales probed with this molecule. The top row is tapered with a 400 kλ Gaussian to best reduce the amount of noise and show the proper resolution to the spatial scales shown. The $H^{13}CO^+$ emission is primarily tracing the intermediate dense, gaseous material within the inner envelope, but the higher-velocity emission does originate near the protostars. The columns correspond to similar velocity ranges of $C^{17}O$ emission as shown in the previous figure, with low, medium, and high Doppler-shifted velocity ranges delineated as red (blue). Negative contours do not show additional structure and are suppressed for visual aid. The red lines indicate the region extracted for PV diagram construction, along the position angle of the major axis in a region much larger than the $C^{17}O$ PV diagram extraction to fully capture the emission. Low velocity: velocity ranges 4.7 → 5.7 km s^{-1} (3.6 → 4.7 km s^{-1}), contours start at 10σ (10σ) and iterate by 2σ (2σ) with the 1σ level starting at 0.003 (0.003) Jy beam^{-1} for the top row and 0.005 (0.005) Jy beam^{-1} for the bottom row, red (blue) channels. Medium velocity: velocity ranges 5.7 → 6.7 km s^{-1} (2.4 → 3.5 km s^{-1}), contours start at 5σ (5σ) and iterate by 5σ (3σ) with the 1σ level starting at 0.005 (0.005) Jy beam^{-1} for the top row and 0.005 (0.005) Jy beam^{-1} for the bottom row, red (blue) channels. High velocity: velocity ranges 6.7 → 7.7 km s^{-1} (1.3 → 2.4 km s^{-1}), contours start at 5σ (5σ) and iterate by 2σ (2σ) with the 1σ level starting at 0.002 (0.002) Jy beam^{-1} for the top row and 0.005 (0.005) Jy beam^{-1} for the bottom row, for the red (blue) channels. The $H^{13}CO^+$ synthesized beam (top: 0.″374 × 0.″310, bottom: 0.″85 × 0.″52) is the bottom rightmost ellipse on each of the panels, and the continuum synthesized beam (0.″11 × 0.″05) is offset diagonally.

mass. For circum-multiple systems, the center of mass is nontrivial to measure, because it is defined by the combined mass of each object and the distribution can be asymmetric. Figure 16 compares various "kinematic centers" for the circumstellar disk of IRS3B depending on the methodology used. First, by fitting the midpoint between the highest-velocity $C^{17}O$ emission channels, where both red- and blueshifted emission is present, for IRS3B-ab using the respective red- and blueshifted emission, the recovered center is $03^h25^m36.^s32$ 30° 45′14.″92, which is very near IRS3B-a. The second method, fitting symmetry in the PV diagram, however, requires a different center in order to reflect the best symmetry of the emission arising from the disk, at $03^h25^m36.^s33$ 30°45′15.″04, which corresponds to a position northeast of the binary pair, which is close to a region of reduced continuum emission ("deficit" in Figure 2). The first method of fitting the highest-velocity emission assumes these highest-velocity channels correspond to regions that are closest to the center of mass and the emission is symmetric at a given position angle. We chose the $C^{17}O$ molecule, which is not affected by the strong outflows, appears to trace the continuum disk the best, and has no outflow contamination, for fitting. The second method of fitting the PV diagram center assumes the source is symmetric and well described by a simple Keplerian disk across the position angle of the PV cut, ignoring the asymmetry along the minor axis. Finally, we include two other positions corresponding to the peak emission in the highest-velocity blue and red Doppler-shifted channels, respectively. Unsurprisingly, these positions are on either side of the peak fit. The difference in the position of the kinematic centers is within ∼2 resolution elements of the $C^{17}O$ map and does not significantly affect our mass determination, as demonstrated in our following analysis.

We use a method of numerically fitting the $C^{17}O$ PV diagrams employed by Ginsburg et al. (2018) and Seifried et al. (2016), by fitting the emission that is still coupled to the disk and not a part of the envelope emission. This helps to provide better constraints on the kinematic center for the Keplerian circum-multiple disk. This was achieved by extracting points in

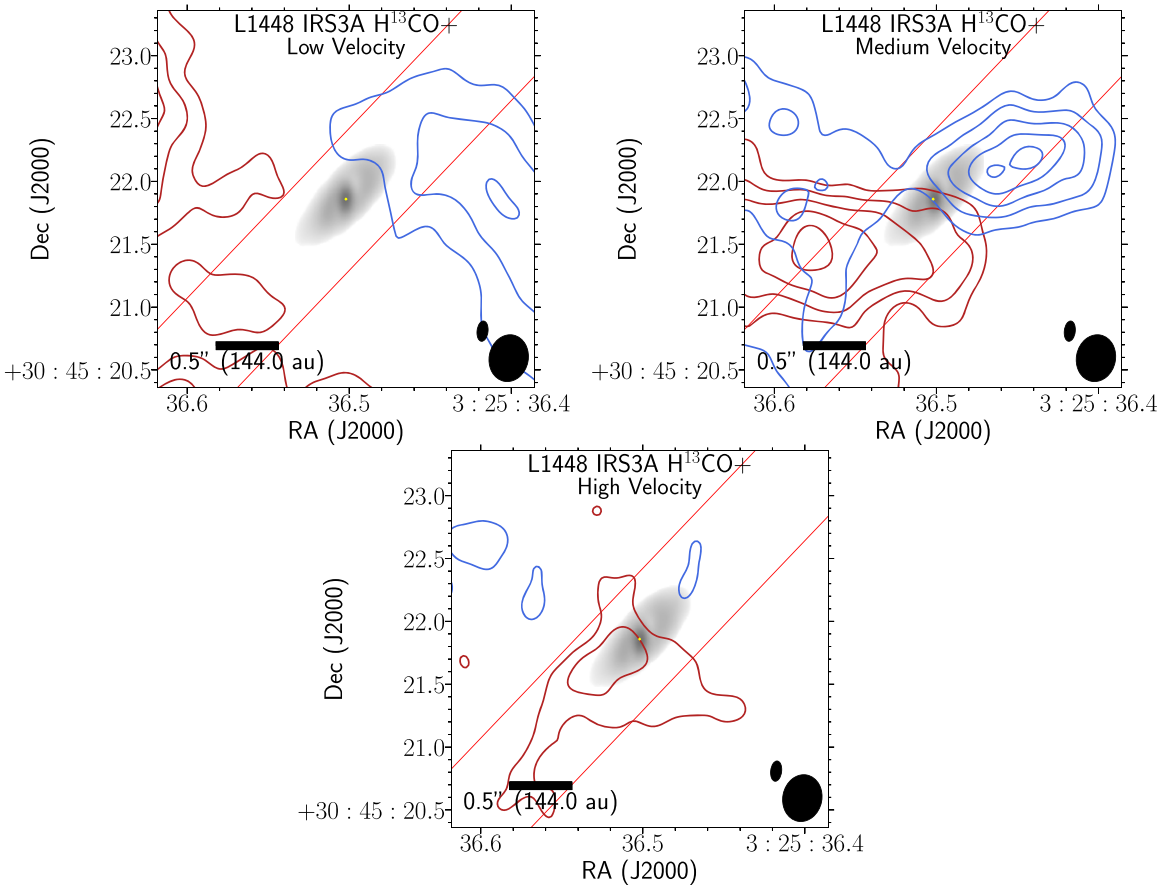

Figure 8. $H^{13}CO^+$ integrated intensity map toward IRS3A generated at a position angle of 125°, whose emission predominately traces the intermediate dense, gaseous material of the inner envelope. The image is tapered with a 400 kλ Gaussian to best reduce the amount of noise and show the proper resolution to the spatial scales shown. The $H^{13}CO^+$ emission might trace a velocity gradient across the source, but the lack of strong emission coming from the disk itself hinders resolving the kinematics. The columns correspond to low-, medium-, and high-velocity ranges. The following panel descriptions will be noted red (blue), corresponding to the Doppler shifted emission. Low velocity: velocity ranges 5.2 → 6.5 km s^{-1} (4.1 → 5.2 km s^{-1}), contours start at 5σ (5σ) and iterate by 2σ (2σ) with the 1σ level starting at 0.004 (0.007) Jy beam^{-1} for the red (blue) channels. Medium velocity: velocity ranges 6.5 → 7.4 km s^{-1} (3.0 → 4.1 km s^{-1}), contours start at 3σ (3σ) and iterate by 2σ (2σ) with the 1σ level starting at 0.003 (0.003) Jy beam^{-1} for the red (blue) channels. High velocity: velocity ranges 7.4 → 8.6 km s^{-1} (1.8 → 3.0 km s^{-1}), contours start at 3σ (3σ) and iterate by 2σ (2σ) with the 1σ level starting at 0.002 (0.0025) Jy beam^{-1} for the red (blue) channels. The $H^{13}CO^+$ synthesized beam (0.″85 × 0.″52) is the bottom rightmost ellipse on each of the panels, and the continuum synthesized beam (0.″11 × 0.″05) is offset diagonally.

the PV diagram that have emission 10σ along the position axis for a given velocity channel and fitting these positions against the standard Keplerian rotation–velocity formula. The Keplerian velocity is the max velocity at a given radius, but each position within a disk will include a superposition of lower-velocity components due to projection effects.

The fitting procedure was achieved using a MCMC employed by the Python MCMC program *emcee* (Foreman-Mackey et al. 2013). Initial prior sampling limits of the mass were set to 0.1–2 $M_\odot$. Outside of these regimes would be highly inconsistent with prior and current observations of the system. Uncertainty in the distance (22 pc) from the Gaia survey (Ortiz-León et al. 2018) and an estimate of the inclination error (10°) were included, while the parameters (M_* and V_{sys}) were allowed to explore phase space. These place approximate limits to the geometry of the disk. The cyan lines in Figure 11 trace the Keplerian rotation curve with $M_* = 1.15\ M_\odot$ with 3σ uncertainty $= 0.09\ M_\odot$, which fits the edge of the $C^{17}O$ emission from the source. This mass estimate describes the total combined mass of the gravitating source(s). Thus if the two clumps (IRS3B-a and -b) are each forming protostars, this mass would be divided between them. However, with the current observations, we cannot constrain the mass ratio of the clumps. Thus, we can consider two scenarios (Section 6.7), an equal mass binary and a single, dominate central potential.

The $H^{13}CO^+$ PV diagram (Figure 12) shows high-asymmetry emission toward the source. However, the $H^{13}CO^+$ emission is still consistent with the central protostellar mass measured using $C^{17}O$ emission of 1.15 $M_\odot$ (indicated by the white dashed line). This added asymmetry is most likely due to $H^{13}CO^+$ emission being dominated by envelope emission, in contrast to the $C^{17}O$ being dominated by the disk. There is considerably more spatially extended and low-velocity emission that extends beyond the Keplerian curve and cannot be reasonably fitted with any Keplerian curve. Additionally, there is a significant amount of $H^{13}CO^+$ emission that is resolved out near line center, appearing as negative emission, whereas the $C^{17}O$ emission did not have as much spatial filtering as the $H^{13}CO^+$ emission.

4.2.2. IRS3B-c

We also analyzed the $C^{17}O$ kinematics near the tertiary, IRS3B-c, to search for indications of the tertiary mass influencing the disk kinematics. In Figure 17, we show the PV diagram of $C^{17}O$ within a 2.″0 region centered on the tertiary and

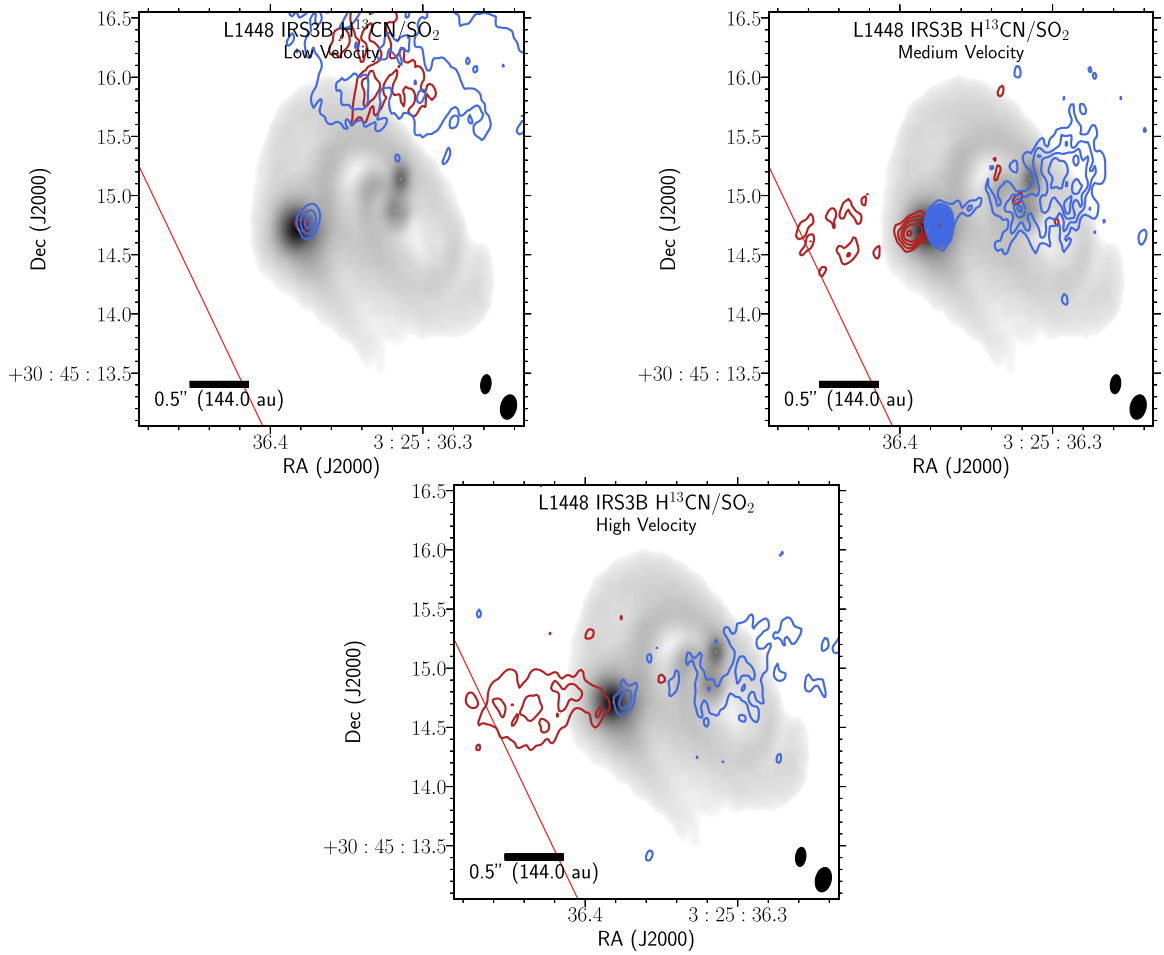

Figure 9. $H^{13}CN/SO_2$ integrated intensity map toward IRS3B appears to trace near the outflow launch location from the tertiary, IRS3B-c. There is pretty large asymmetry in the velocity channels covered by the red- and blueshifted emission. The panels correspond to low-, medium-, and high-velocity ranges. The following panel descriptions will be noted red (blue), corresponding to the Doppler shifted emission. Low velocity: velocity ranges 5.2 → 7.2 km s^{-1} (4 → 4.8 km s^{-1}), contours start at 5σ (5σ) and iterate by 2σ (5σ) with the 1σ level starting at 0.0025 (0.0021) Jy beam^{-1} for the red (blue) channels. Medium velocity: velocity ranges 7.2 → 9.2 km s^{-1} (3.2 → 4 km s^{-1}), contours start at 5σ (5σ) and iterate by 2σ (2σ) with the 1σ level starting at 0.0016 (0.0016) Jy beam^{-1} for the red (blue) channels. High velocity: velocity ranges 9.2 → 11.2 km s^{-1} (1.6 → 3.2 km s^{-1}), contours start at 4σ (4σ) and iterate by 3σ (3σ) with the 1σ level starting at 0.0021 (0.0021) Jy beam^{-1} for the red (blue) channels. The $H^{13}CN$ synthesized beam (0.″22 × 0.″14) is the bottom rightmost ellipse on each of the panels, and the continuum synthesized beam (0.″11 × 0.″05) is offset diagonally.

plot velocities corresponding to Keplerian rotation at the location of IRS3B-c within the disk, to provide an upper bound on the possible protostellar mass within IRS3B-c. Emission in excess of the red dashed lines could be attributed to the tertiary altering the gas kinematics. The velocity profile at IRS3B-c shows no evidence of any excess beyond the Keplerian profile from the main disk, indicating that it has very low mass. Based on the nondetection, we can place upper limits on the mass of the IRS3B-c source of $<0.2\ M_\odot$ as shown by the white dotted lines in Figure 17. A protostellar mass much in excess of this would be inconsistent with the range of velocities observed.

4.2.3. IRS3A

For the IRS3A circumstellar disk, the dense gas tracers $H^{13}CN$ and $C^{17}O$ were used to analyze disk characteristics and are shown in Figures 13 and 14. The position cut is centered on the continuum source (coincides with kinematic center) and spans 2″ (∼576 au) on either side. This provides a large enough window to collect all of the emission from the source. The dotted white lines show the Keplerian velocity corresponding to a $M_* = 1.4\ M_\odot$ central protostar, which is consistent with the PV diagram.

The spatial compactness of IRS3A limits the utility of the $H^{13}CN$ PV diagram with the previous MCMC fitting routine. We found evidence of rotation in this line tracer from the velocity selected moment 0 map series and PV diagram. However, from the PV diagram alone, strong constraints cannot be determined due to the compactness of the $H^{13}CN$ emission and the low S/N of $C^{17}O$.

5. Application of Radiative Transfer Models

To further analyze the disk kinematics, we utilize the methods described in Sheehan et al. (2019) and further described in Appendix C for modeling the molecular line emission presented thus far. The modeling framework uses RADMC-3D (Dullemond et al. 2012) to calculate the synthetic channel maps using 2D axisymmetric radiative transfer models in the limit of local thermodynamic equilibrium and GALARIO (Tazzari et al. 2018) to generate the model visibilities from those synthetic channel maps. We sample the posterior distributions of the parameters to provide fits to the visibilities by utilizing a MCMC approach

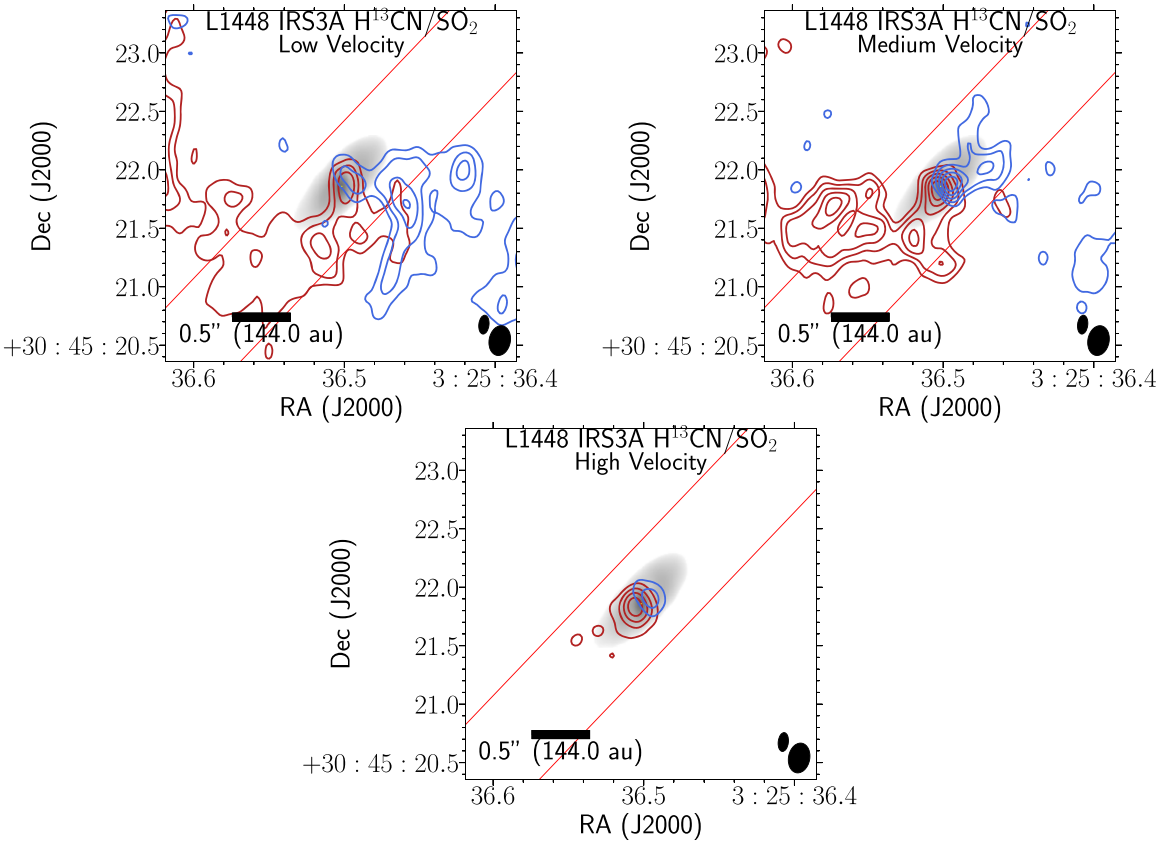

Figure 10. $H^{13}CN/SO_2$ integrated intensity map toward IRS3A, whose emission appears to trace rotation within the inner disk. The panels correspond to low-, medium-, and high-velocity ranges. The following panel descriptions will be noted red (blue), corresponding to the Doppler shifted emission. The system velocity of the $H^{13}CN/SO_2$ emission ($\sim$5.4 km s^{-1}) agrees with system velocity of $C^{17}O$, likely tracing $H^{13}CN$ emission and not SO_2 emission. Low velocity: velocity ranges 5.2 $\rightarrow$ 6.5 km s^{-1} (4.1 $\rightarrow$ 5.2 km s^{-1}), contours start at 4σ (4σ) and iterate by 2σ (2σ) with the 1σ level starting at 0.0021 (0.0021) Jy beam^{-1} for the red (blue) channels. Medium velocity: velocity ranges 6.5 $\rightarrow$ 7.4 km s^{-1} (3.0 $\rightarrow$ 4.1 km s^{-1}), contours start at 4σ (4σ) and iterate by 2σ (2σ) with the 1σ level starting at 0.0016 (0.0016) Jy beam^{-1} for the red (blue) channels. High velocity: velocity ranges 7.4 $\rightarrow$ 8.6 km s^{-1} (1.8 $\rightarrow$ 3.0 km s^{-1}), contours start at 4σ (4σ) and iterate by 3σ (3σ) with the 1σ level starting at 0.0021 (0.0021) Jy beam^{-1} for the red (blue) channels. The $H^{13}CN$ synthesized beam (0.″22 $\times$ 0.″14) is the bottom rightmost ellipse on each of the panels, and the continuum synthesized beam (0.″11 $\times$ 0.″05) is offset diagonally.

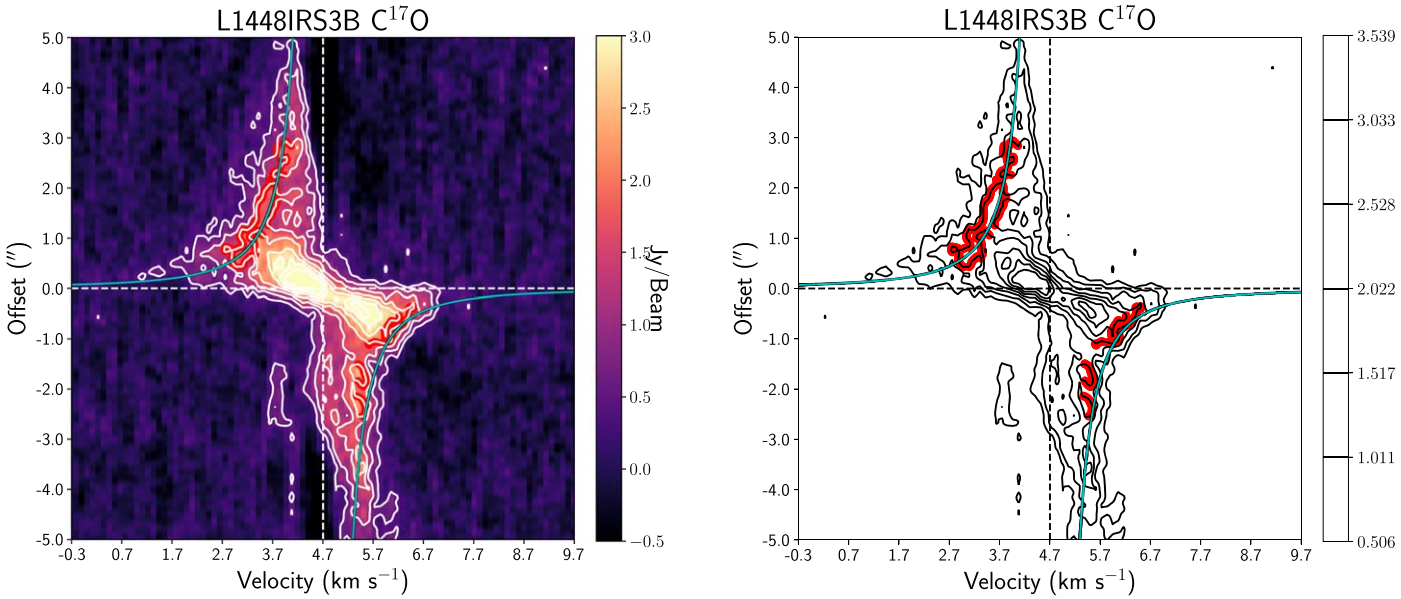

Figure 11. PV diagrams of IRS3B $C^{17}O$ emission generated at a position angle of 29°, with the cyan lines corresponding to the fit of 1.15 $M_\odot$, demonstrating the data could be reproduced reasonably well with a Keplerian disk orbiting a 1.15 $M_\odot$ protostar. The cyan line traces the median fit for a numeric Keplerian orbital fit routine, while the black lines represent 100 randomly sampled Markov Chain Monte Carlo (MCMC) fits, used to estimate errors. As evident, this methodology selectively fits the highest-velocity emission that is symmetric in the protostellar system. The white/black contours trace regions starting from 3σ at 2σ intervals, where $\sigma \approx 0.14$ Jy beam^{-1}. The red contours trace the regions selected for the MCMC fit, which are defined as the 10 and 12σ levels so as to not fit the diffuse large-scale emission.

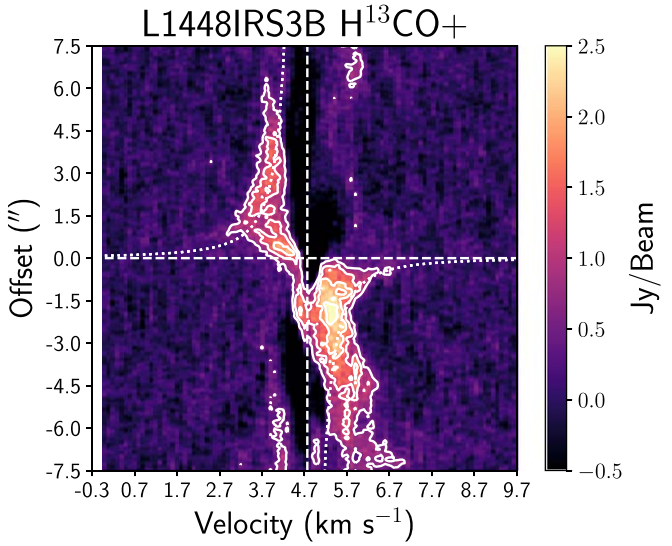

Figure 12. $H^{13}CO^+$ emission toward IRS3B generated at a position angle of 29°, with the white dashed lines corresponding to the Keplerian fit of 1.15 $M_\odot$ from the fit to $C^{17}O$, demonstrating the data are not inconsistent with a 1.15 $M_\odot$ protostar, similarly demonstrated from the $C^{17}O$ emission Keplerian fits. The PV diagram shows a large amount of asymmetry in the molecular line emission close to system velocity, with emission at velocities in excess of Keplerian particularly at the redshifted velocities. These are possible indications of infalling material from the envelope given the spatial location of this emission. The white contours trace regions starting from 3σ at 2σ intervals, where $\sigma \approx 0.15$ Jy.

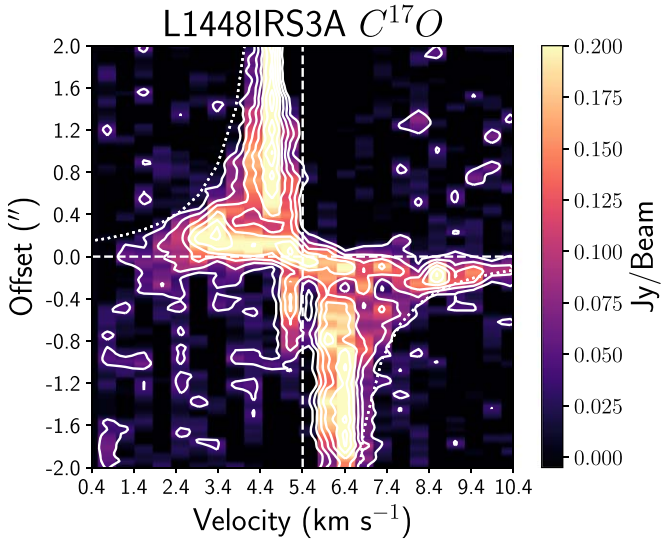

Figure 13. PV diagrams of IRS3A $C^{17}O$ emission generated at a position angle of 125°, with the dotted lines corresponding to 1.4 $M_\odot$. The emission suffers from the lower spatial sampling across the source and the extended, resolved-out emission from the IRS3B+A envelope/core. Similarly, strong spatial integration (width of slice 0.″3) restrictions were placed when making the PV diagram to limit the inclusion of large-scale emission. The white contours trace regions starting from 3σ at 2σ intervals, where $\sigma \approx 0.15$ Jy.

(*pdspy*; Sheehan et al. 2019). *pdspy* uses the full velocity range given by the frequency limit of the input visibilities in modeling.

Some of the parameters are less constrained than others due to asymmetry of the disks, and discussion of these parameters fall outside the scope of the kinematic models sought in this paper. Our focus for the kinematic models are position angle (p.a.), inclination (inc.), stellar mass (M_*), disk radius (R_D), and system velocity (V_{sys}). We provide a summary of our model results in Table 5.

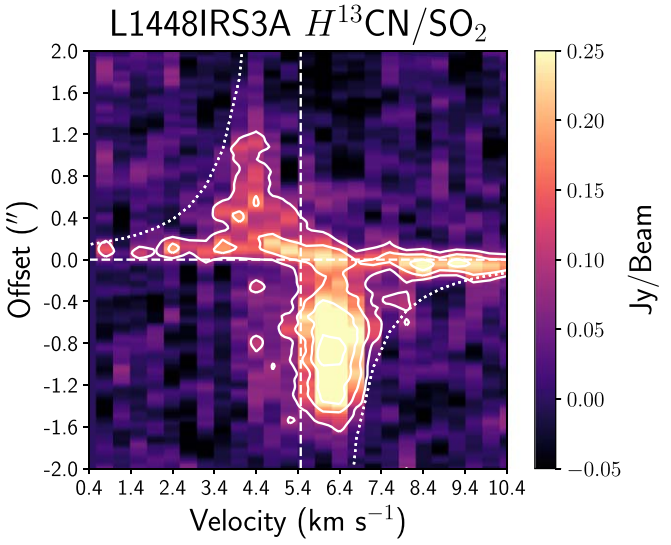

Figure 14. PV diagram of IRS3A $H^{13}CN/SO_2$ emission with the dotted lines corresponding to Keplerian velocities for a 1.4 $M_\odot$ protostar. This PV diagram places a constraint on the possible protostellar mass parameter of ∼1.4 $M_\odot$. The IRS3A mass is less well constrained due to the compactness of the emission. Strong spatial integration (width of slice 0.″3) restrictions were placed when making the PV diagram to help limit the inclusion of large-scale emission.

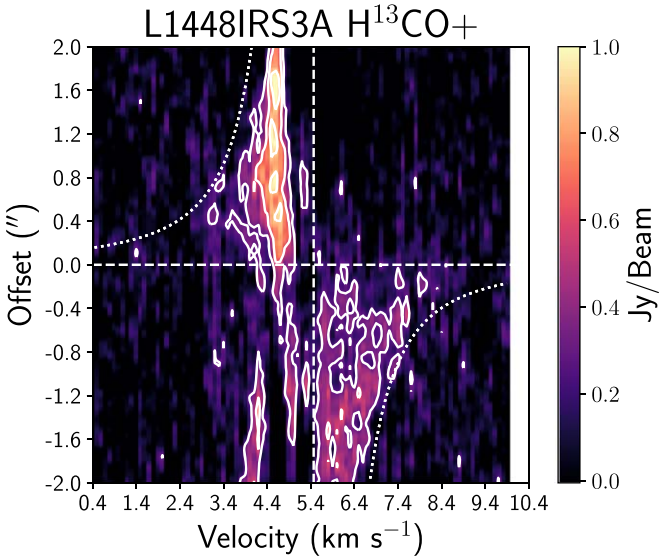

Figure 15. PV diagram of IRS3A $H^{13}CO^+$ generated at a position angle of 125°, whose emission predominately traces the intermediate dense, gaseous material of the inner envelope. The emission is fainter and is coming from the outer disk/inner envelope. The dotted line corresponds to a central protostellar mass of 1.4 $M_\odot$.

The combined fitting of the models is computationally expensive (fitting 200 models simultaneously per "walker integration time step"), requiring on average (1–2) × 10^4 core-hours per source to reach convergence. We run these models across five nodes with 24 cores/nodes each for ∼150 hr on the University of Oklahoma Supercomputing Center for Education and Research supercomputers to reach sufficient convergence in the parameters. The convergence state is determined when the *emcee* "walkers" reach a steady-state solution where the ensemble of walkers is not changing by an appreciable amount, simply oscillating around some median value with a statistical variance.

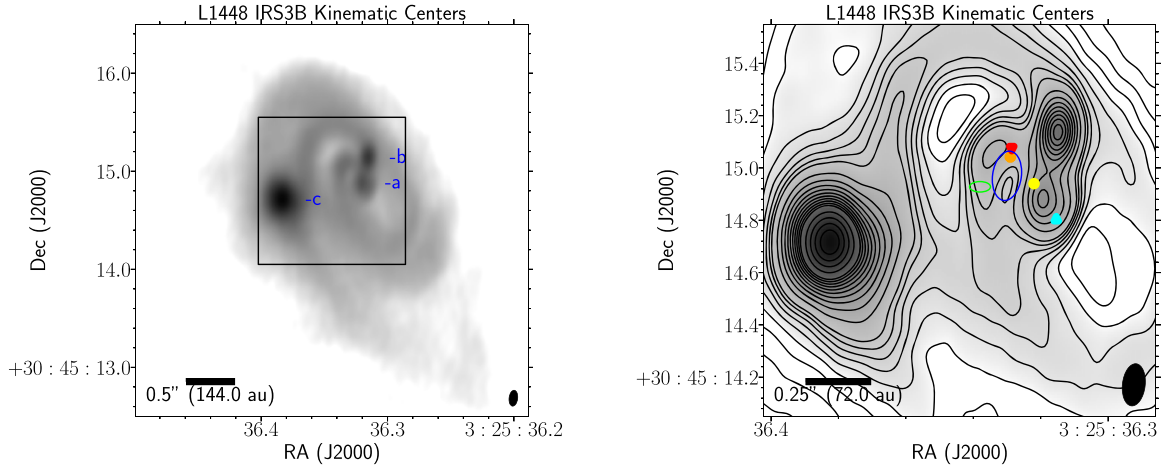

Figure 16. Positions of the various "kinematic centers" that have been fit from $C^{17}O$ emission at IRS3B in relation to continuum structure. The gray scale is the dust continuum from Figure 1. Left: the blue colored texts detail the locations of continuum sources, presumed to be protostars. Right: a zoom-in on the region indicated by the black rectangle in the left image. The red and blue triangles indicate the central Gaussian fit of the highest Doppler-shifted velocity emission, with the yellow circle indicating the midpoint. The orange circle indicates the center that best constructs the PV diagram symmetrically. The green ellipse is the model Keplerian centroid fit with the respective error as indicated by the size of the ellipse (see Section 5). The blue ellipse is the $C^{17}O$ beam ($0\farcs21 \times 0\farcs13$) centered on the region of emission deficit for size comparison. The contours start at 10σ and iterate by 10σ with the 1σ level starting at 8.5×10^{-5} Jy beam^{-1}. The region of deficit, first identified in Figure 2, is shown to be centered within the three various kinematic center fits and are marginally separated by less than a few beams.

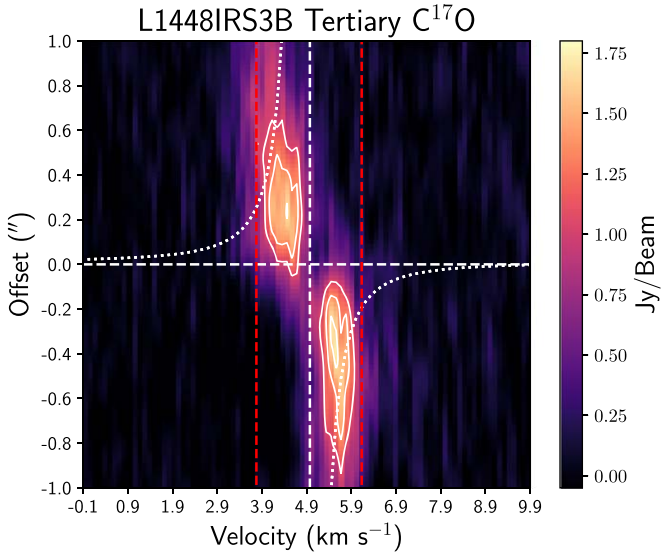

Figure 17. PV diagram of $C^{17}O$ toward IRS3B-c, the tertiary. The white lines correspond to a Keplerian curve of a 0.2 $M_\odot$ protostellar source. These fits place an upper limit to the mass of the tertiary companion to <0.2 $M_\odot$, since if the mass were any larger, we would expect to see emission extending to high velocity, indicating the tertiary would be affecting disk kinematics. The red dashed lines indicate the maximum Keplerian velocities at the radius of IRS3B-c in the rotating disk corresponding to the 1.15 $M_\odot$ mass of the central potential. Emission outside of these bounds could be due to the tertiary affecting disk kinematics, but from this analysis, we cannot detect an obvious effect of the tertiary on the disk kinematics. The white/black contours trace regions starting from 14σ at 4σ intervals, where $\sigma \approx 0.1$ Jy beam^{-1}.

5.1. IRS3B

The *pdspy* kinematic flared disk model results for IRS3B are shown in Figure 18 with the Keplerian disk fit compared with the data. The system velocity fitted is in agreement with the PV diagram analysis. There is some uncertainty in the kinematic center, due to the diffuse, extended emission near the system velocity (<1 km s^{-1}), which yields degeneracy when fitting. The models yielded similar stellar masses compared with the PV/Gaussian fitting (3σ uncertainties listed, *pdspy* $1.19^{+0.13}_{-0.07}$ $M_\odot$; PV: $1.15^{+0.09}_{-0.09}$ $M_\odot$) and similar position angles (*pdspy*: $27^\circ{}^{+1.8}_{-2.9}$; PV: $\sim 28^\circ$), and while the inclinations are not similar (*pdspy*: $66^\circ{}^{+3.0}_{-4.6}$; Gaussian: $\sim 45^\circ$), this discrepancy in inclination is most likely due to a difference in asymmetric gas and dust emission. With the tertiary subtraction method (Appendix F), we Gaussian fit the dust continuum of IRS3B-c to preserve the underlying disk structure, then fit the IRS3B-ab disk with a single Gaussian. Using the PV diagram fitting, we attempt to fit symmetric Keplerian curves to the PV diagram. *pdspy* attempts to also fit the asymmetric southeast side of the disk, which is an asymmetric feature, with the model symmetric Keplerian disk. Upon further inspection of the residual map, there is significant residual emission on the southeastern side of the disk, which is likely a second-order effect in the fit; however, it is confined spatially and spectrally and should not have a major effect on the overall fit.

5.2. IRS3A

The *pdspy* kinematic flared disk model results for IRS3A are shown in Figure 19, primarily fitting the inner disk. The models demonstrate that the gas disk is well represented by a truncated disk with a maximum radius of the disk of ~40 au (most likely due to the compact nature of the emission). This disk size of 40 au is smaller than the continuum disk and results from the compact emission of $H^{13}CN$. The models find a system velocity near 5.3 km s^{-1} in agreement with the PV diagram. The system velocities of numerous molecules ($H^{13}CO^+$, $C^{17}O$, and $H^{13}CN$) are in agreement and thus likely tracing the same structure in the system. The models yielded a similar stellar mass ($1.51^{+0.06}_{-0.07}$ $M_\odot$, 3σ uncertainties listed) to the estimate from the PV diagram. Also the disk orientation of inclination (69°) and position angle (~122°) agree with the estimate from the continuum Gaussian fit.

6. Discussion

6.1. Origin of Triple System and Wide Companion

Protomultiple systems like that of IRS3B and IRS3A can form via several possible pathways: thermal fragmentation (on scales ~1000s of au), turbulent fragmentation (on scales ~1000s of

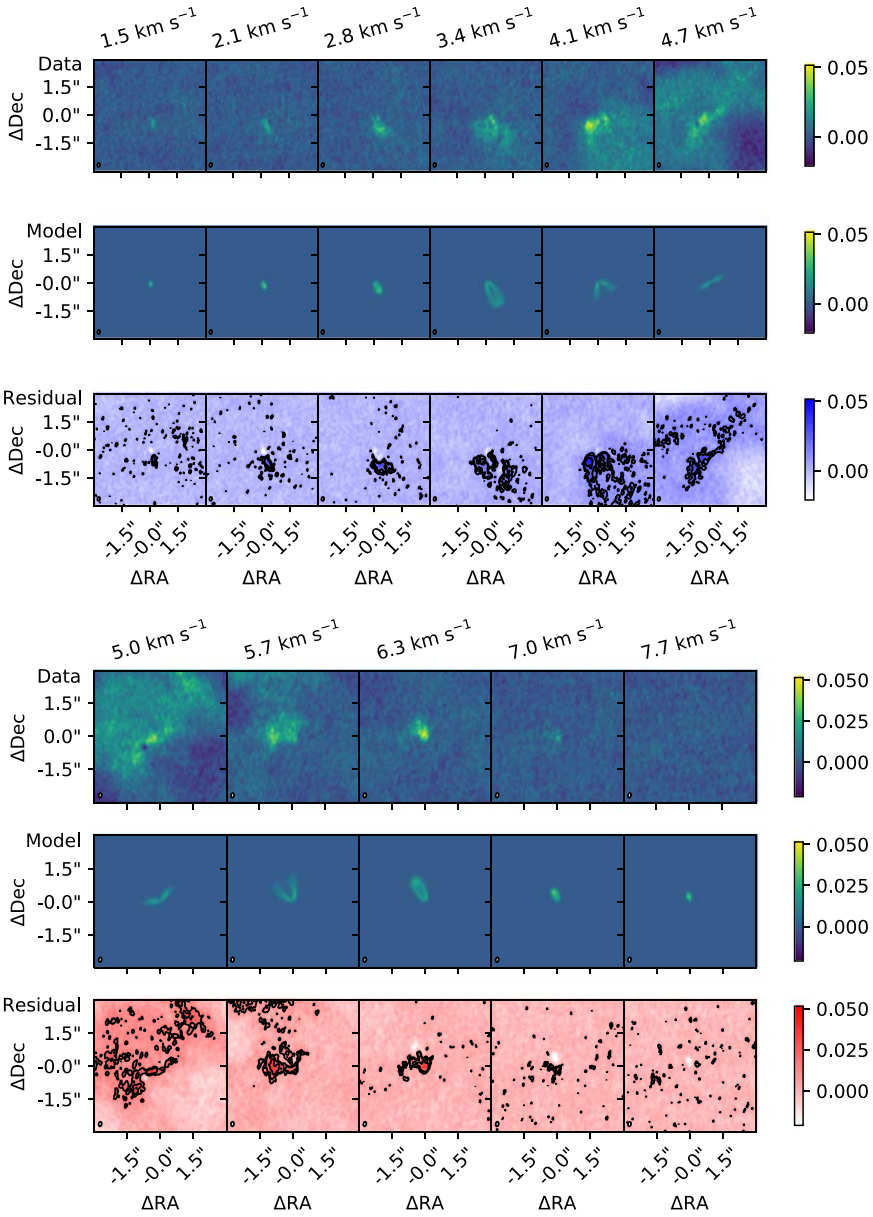

Figure 18. IRS3B kinematic model comparison: A representative selection of channel maps that demonstrate the fit of the model to the data. The top figure is the blue Doppler-shifted emission, while the bottom figure is the red Doppler-shifted emission. The first row contours are the model contours, generated at the 2, 3, 5, and 10σ level overlaid on the data channels selected at the same velocity. The second row is the residual contours (2 and 3σ) overlaid on the same data channels. System velocity is ∼4.8 km s^{-1}. It should be noted the highly correlated structure is visible in the residuals. This reflects an imperfect fit to the data given that the circumstellar disk itself is asymmetric.

Table 5
Kinematic *pdspy* Modeling

Source	R.A. Offset ($''$)	Decl. Offset ($''$)	Inc. (°)	P.A. (°)	M_* ($M_\odot$)	$M_{\rm gas}$[a] ($M_\odot$)	$R_{\rm disk}$ (au)	$V_{\rm sys}$ (km s^{-1})	Turbulence (km s^{-1})	Surface Density Index γ	T_0 (K)
IRS3B	$0.031^{+0.019}_{-0.011}$	$0.025^{+0.020}_{-0.015}$	$66.0^{+3.0}_{-4.6}$	$26.7^{+1.8}_{-2.9}$	$1.19^{+0.13}_{-0.07}$	$0.079^{+0.021}_{-0.016}$	$299.0^{+24.9}_{-47.6}$	$4.880^{+0.110}_{-0.090}$	$0.012^{+0.005}_{-0.003}$	$1.2^{+0.1}_{-0.1}$	50^{+3}_{-5}
IRS3A	$0.034^{+0.003}_{-0.003}$	$0.015^{+0.003}_{-0.003}$	$69.5^{0.38}_{0.37}$	$122.4^{1.4}_{1.4}$	$1.51^{+0.06}_{-0.07}$	$6.3^{+1.6}_{-1.3} \times 10^{-6}$	$39.9^{+2.4}_{-1.4}$	$5.288^{+0.090}_{-0.084}$	$0.015^{+0.06}_{-0.009}$	$0.4^{+0.2}_{-0.1}$	163^{+9}_{-8}

Note. Summary of kinematic model parameters. The R.A. and decl. offsets of the *pdspy* modeling are defined from the central positions given in PV analysis, Table 4. The errors presented are the 3σ confidence intervals of the best-fit walkers generated from *emcee*.
[a] The reported values of $M_{\rm gas}$ depend on the assumed abundance for each of the molecules. For the IRS3B source, we used the $C^{17}O$ emission, which has an assumed abundance of 2×10^{-7} relative to H_2, while for the IRS3A source we used the $H^{13}CN$ emission, which has an assumed abundance of 2.9×10^{-11} relative to H_2.

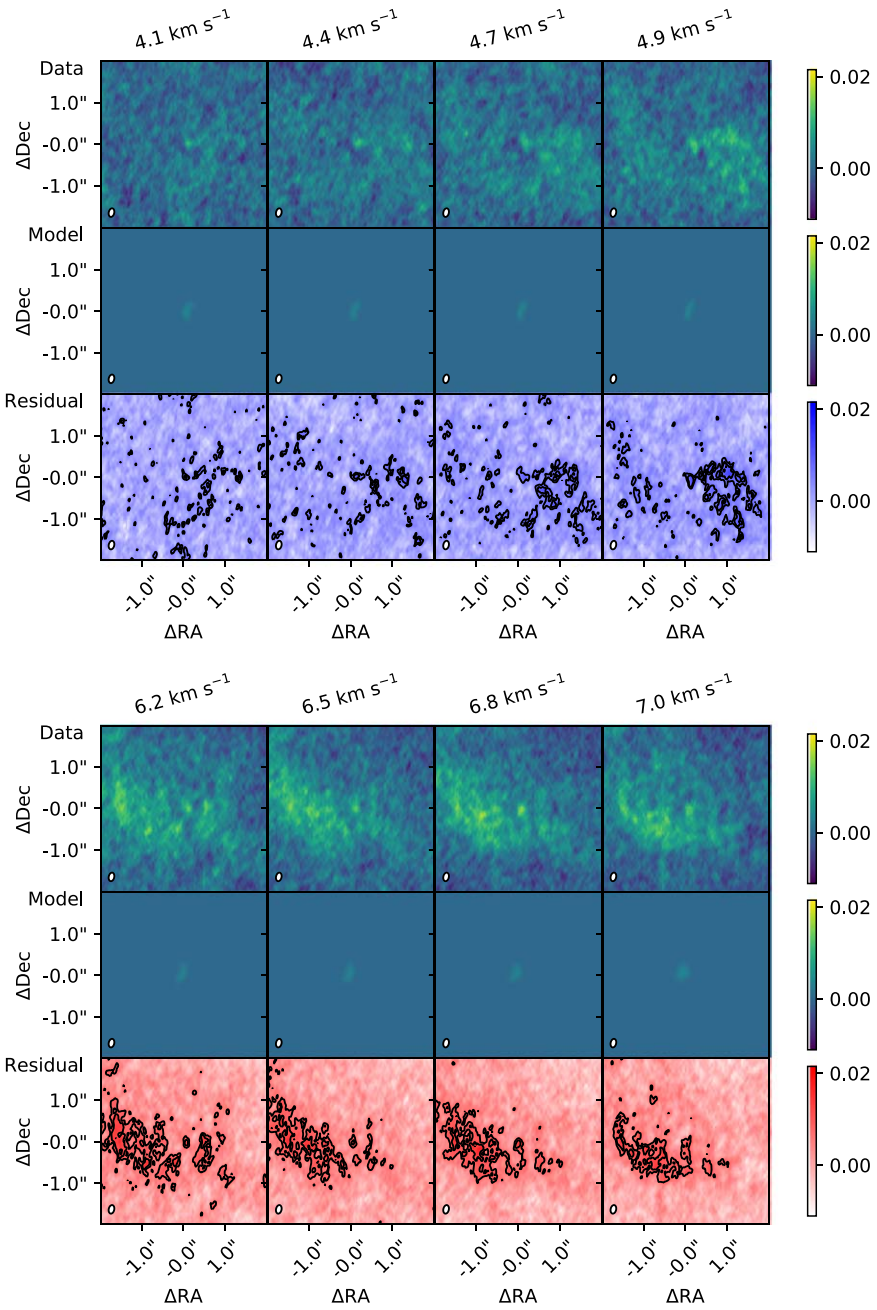

Figure 19. IRS3A kinematic model comparison: a representative selection of channel maps that demonstrate the fit of the model to the data. The top figure is the blue Doppler-shifted emission, while the bottom figure is the red Doppler-shifted emission. The first row contours are the model contours, generated at the 2, 3, 5, and 10σ level overlaid on the data channels selected at the same velocity to not overshadow the emission. The second row is the residual contours overlaid on the same data channels. System velocity is ~5.2 km s^{-1}. There is residual emission at scales much larger than the continuum disk, especially prevalent near the system velocity, likely due to large-scale emission from the cloud that is not included in the disk.

au), GIs within disks (on scales ~100s of au), and/or loose dynamical capture of cores (on scales ~10^{4-5} au). To constrain the main pathways for forming multiple systems, we must first constrain the protostellar geometrical parameters and then the (in)stability of the circum-multiple disk. Previous studies toward L1448 IRS3B (see Tobin et al. 2016a) achieved ~0.″4 molecular line resolution, roughly constraining the protostellar mass. The high-resolution and high-sensitivity data we present allow constraints on the stability of the circumstellar disk of IRS3B and shed light on the formation pathways of the compact triple system and the wide companion. The circumstellar disk around the wide companion, IRS3A, has an orthogonal major axis orientation to the circumstellar disk of IRS3B, favoring formation mechanisms that result in wider companions forming with independent angular momentum vectors. The circumstellar disk around IRS3B is massive, has an embedded companion (IRS3B-c), and has spiral arms, which are indicative of GI, and we will more quantitatively examine the (in)stability of the disk in Section 6.3.

6.2. Signatures of an Embedded Companion in Disk Kinematics

Hydrodynamic simulations show that massive embedded companions within viscous disks should impact the Keplerian

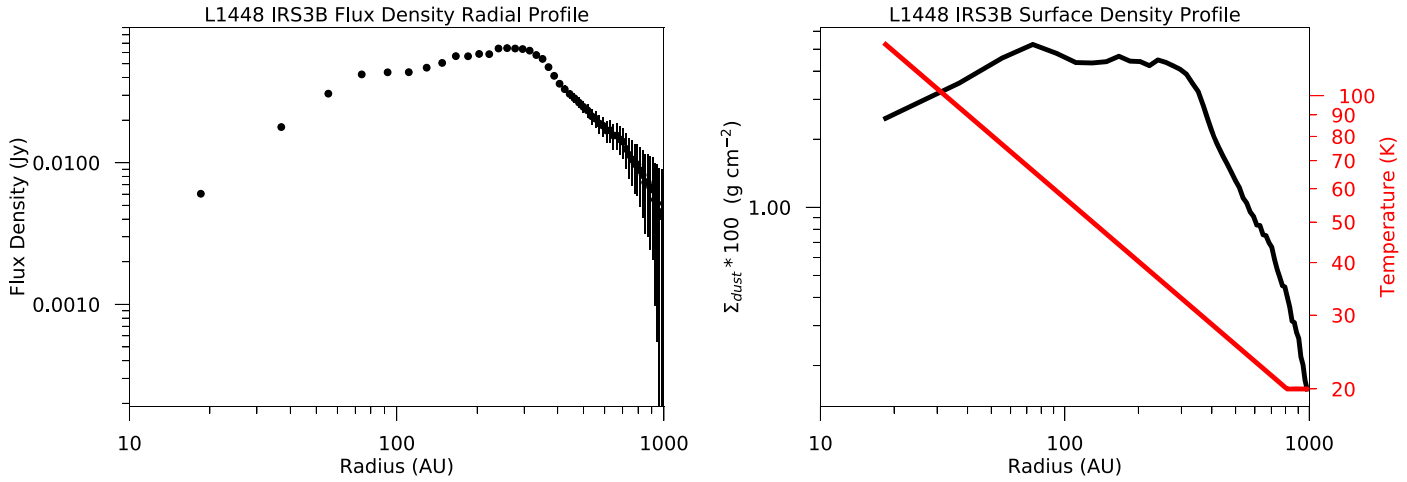

Figure 20. The left plot is the continuum flux density radial profile of IRS3B. The right plot is the deprojected radial surface density profile of the dust continuum in black, while the red line is the radial temperature profile of the disk. The temperature profile is $\propto R^{-0.5}$ and is scaled such that at 100 au it is described via (30 K) $\times$ $(L_*/L_\odot)^{0.25} \approx 40.1$ K.

velocity pattern in a detectable manner (Perez et al. 2015). Pérez et al. (2018) showed the signatures of a massive companion embedded within a viscous, non-self-gravitating disk. Their model observations are higher ($\sim$2$\times$) spectral and angular resolution and more sensitive ($\sim$5$\times$) than the presented observations. They show that a 10 M_J mass source should be easily detectable with about 1000 orbits of evolution by analyzing the moment 1 maps. More recently, several studies of protoplanetary disks have confirmed these predictions of localized Keplerian velocity deviations for moderately massive planets (Pinte et al. 2018b, 2019). However, these systems are much more evolved (>3 Myr), with quiescent, non-self-gravitating disks, and likely experienced thousands of stable orbits compared to IRS3B, a self-gravitating and actively accreting class 0 source, with a companion that likely has completed only a few dynamically changing orbits.

Hall et al. (2020) performed simulations of a viscous, self-gravitating disk (0.3 $M_\odot$) around a 0.6 $M_\odot$ source much more similar in physical parameters or IRS3B than the types of systems discussed in the preceding paragraph. Their results showed that the effects of self-gravity will provide "kinks" at high resolution and sensitivity. Additionally, Vorobyov & Basu (2011) showed that, due to exchange of momentum with the disk or dispersal due to tidal torques, the fragment radius would be drastically changing up to an order of magnitude over the evolution of the disk. All of these work to mask definitive observable kinematic deviations of embedded companions in the disk.

6.3. Disk Structure

With the high-resolution observations, we can construct a radial profile of the continuum emission to analyze disk structure. The circumstellar disk of IRS3B has prominent spiral arms, but the radial profile will azimuthally average this emission. In order to construct the radial profile, we have to define an image center to begin the extraction, the geometry (position angle and inclination) of the source, and the size of each annuli. The system geometry and image center were all adapted from the PV diagram fit parameters, and the radius of the annuli is defined as half the average synthesized beam size (Nyquist Sampling; Nyquist 1928). We then convert from flux density to mass via Equation (1) and further construct a disk mass surface density profile. To convert from flux density into dust mass, we adopt a radial temperature power law with a slope of -0.5, assuming the disk at 100 au can be described with a temperature of (30 K) $\times$ $(L_*/L_\odot)^{0.25}$. The temperature profile has a minimum value of 20 K, based on models of disks embedded within envelopes (Whitney et al. 2003). While we adopt a temperature law profile, protostellar multiples are expected to complicate simple radial temperature profiles.

Toward IRS3B, in order to mitigate the effects of the tertiary source in the surface density calculations, we use the tertiary subtracted images, described in the Appendix F. The system geometric parameters used for the annuli correspond to an inclination of 45° and a position angle of 28°. The PV/Gaussian fits were used here for ease of reproducibility, and utilizing the *pdspy* results would still be consistent. The largest annulus extends out to 5″, corresponding to the largest angular scale on which we can recover most emission. The temperature at 100 au for IRS3B-ab is taken to be ≈40.1 K. We show both the extracted flux radial profile and radial surface density profile for IRS3B-ab in Figure 20. The radial surface density profile shows a flat surface density profile out to ∼400 au.

Toward IRS3A, the system geometry parameters used for the annuli correspond to an inclination of 69° and a position angle of 133°. With this method, we construct a radial surface density profile to analyze the stability of the disk (Figure 21). The temperature at 100 au for IRS3A is taken to be ≈50.9 K. The circumstellar disk of IRS3A is much more compact than the circumstellar disk of IRS3B, with the IRS3A disk radius ∼150 au, and thus the assumed temperature at 100 au is a good approximation for the median disk temperature.

6.3.1. Disk Stability

The radial surface density profiles allow us to characterize the stability of the disk to its self-gravity as a function of radius. The Toomre Q parameter (herein Q) can be used as a metric for analyzing the stability of a disk. It is defined as the ratio of the rotational shear and thermal pressure of the disk versus the self-gravity of the disk, susceptible to fragmentation. When the Q parameter is <1, it indicates a gravitationally unstable region of the disk.

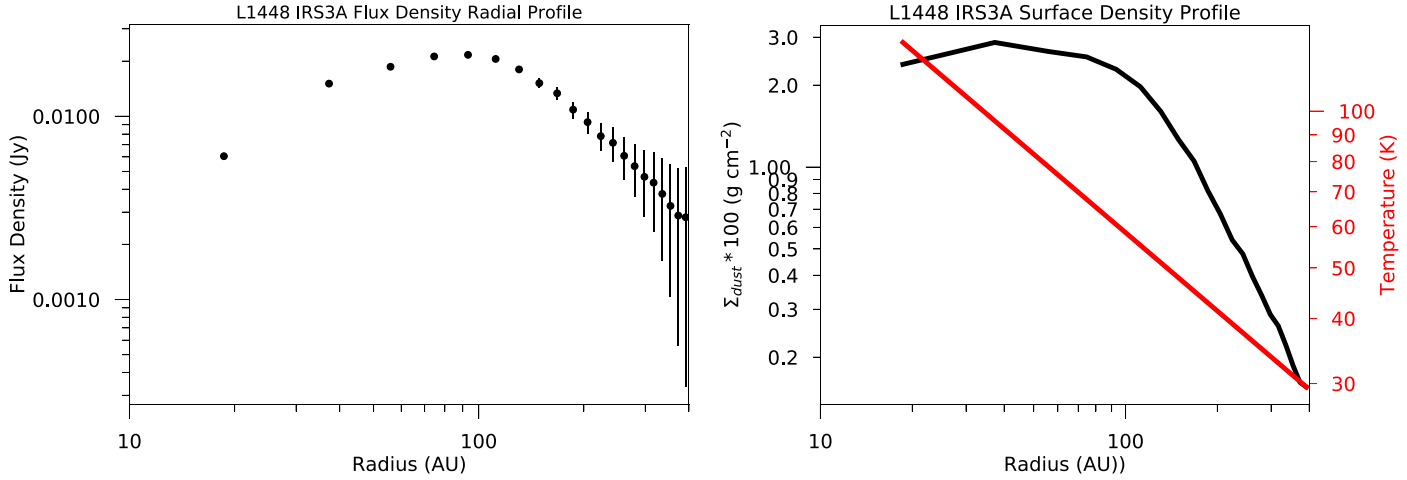

Figure 21. The left plot is the continuum flux density radial profile of IRS3A. The right plot is the radial surface density profile of the dust continuum in black, while the red line is the radial temperature profile of the disk. The temperature profile is $\propto R^{-0.5}$ and is scaled such that at 100 au it is described via (30 K) $\times$ $(L_*/L_\odot)^{0.25} \approx 53.1$ K.

Q is defined as

$$Q = \frac{c_s \kappa}{\pi G \Sigma}, \tag{3}$$

where the sound speed is c_s, the epicyclic frequency is κ corresponding to the orbital frequency ($\kappa = \Omega$ in the case of a Keplerian disk), the surface density is Σ, and G is the gravitational constant.

We further assume the disk is thermalized and the disk sound speed radial profile is given by the kinetic theory of gases:

$$c_s(T) = \left(\frac{k_b T}{m_{\rm H}\mu}\right)^{0.5}, \tag{4}$$

where T is the gas temperature and μ is the mean molecular weight (2.37). We then evaluate the angular frequency as a function of radius,

$$\Omega(R) = \left(\frac{GM_*}{R^3}\right)^{0.5}, \tag{5}$$

where $M_* = 1.15\ M_\odot$.

Simulations have shown that values of $Q < 1.7$ (calculated in 1D) can be sufficient for self-gravity to drive spiral arm formation within massive disks, while $Q \approx 1$ is required for fragmentation to occur in the disks (Kratter et al. 2010b). Figure 22 shows the Q radial profile for the circumstellar disk of L1448 IRS3B, which varies by an order of magnitude across the plotted range (0.4–4). The disk has $Q < 1$ and therefore is gravitationally unstable starting near ~120 au, interior to the location of the embedded tertiary within the disk and extending out to the outer parts of the disk (~500 au) as indicated by the IRS3B Toomre Q radial profile. The prominent spiral features present in the circumstellar disk span a large range of radii (10s–500 au).

Figure 23 shows the Toomre Q radial profile for the circumstellar disk of L1448 IRS3A. The IRS3A dust continuum emission, while having possible spiral arm detection (Figure 1), is more indicative of a gravitationally stable disk through the analysis of the Toomre Q radial profile ($Q > 5$ for the entire disk). This is due to the higher-mass central protostar and lower disk surface density, as compared with the circumstellar disk of IRS3B. Thus substructures in IRS3A may not be gravitationally driven spiral arms and could reflect other substructure. The

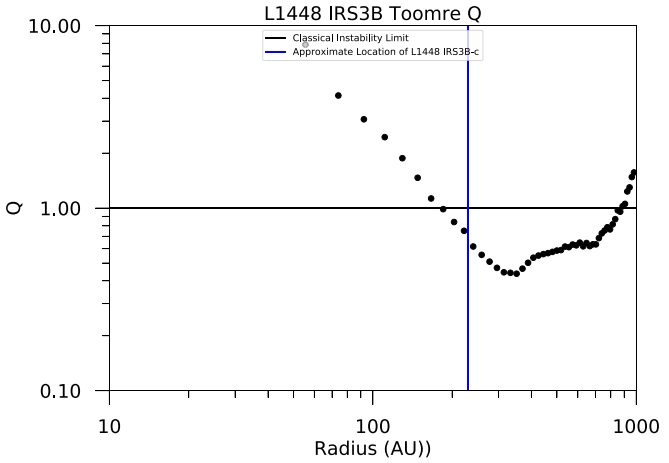

Figure 22. Toomre Q parameter plotted as a function of deprojected radius for IRS3B. The horizontal line indicates a Toomre Q parameter of 1, at which the disk would be gravitationally unstable. As indicated, the disk Toomre Q parameter drops below 1 at a radius of ~120 au. The vertical line corresponds to the deprojected radius of IRS3B-c. The observed spiral arms also become most prominent at $R > 100$ au, where Toomre Q approaches 1.

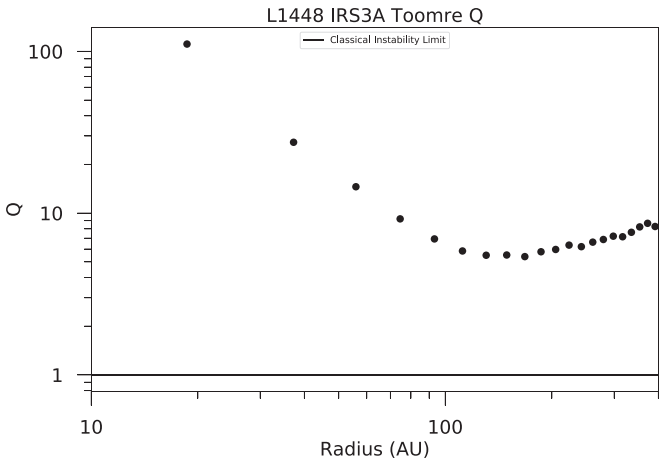

Figure 23. Toomre Q parameter plotted as a function of deprojected radius for IRS3A. The horizontal line indicates a Toomre Q parameter of 1, at which the disk would be gravitationally unstable. The circumstellar disk of IRS3A is much less massive than IRS3B, and coupled with a more massive protostar, the disk is more stable against GIs.

circumstellar disk around IRS3A has a mass of 0.04 $M_\odot$, and the protostar has a mass of 1.4 $M_\odot$.

6.4. Interpretation of the Formation Pathway

The formation mechanism for the IRS3A source, the IRS3B system as a whole, and the more widely separated L1448 NW source Tobin et al. (2016b) is most likely turbulent fragmentation, which works on the 100s–1000s au scales (Offner et al. 2010; Lee et al. 2019). Companions formed via turbulent fragmentation are not expected to have similar orbital configurations and thus are expected to have different V_{sys}, position angle, inclination, and outflow orientations. For the wide companion, IRS3A, the disk and outflows are nearly orthogonal to IRS3B and have different system velocities (e.g., 5.3 km s^{-1} and 4.9 km s^{-1}, respectively; Tables 4 and 5). McBride & Kounkel (2019) have shown that protostellar systems dynamically ejected from multibody interactions are less likely to be disk bearing. Considering the low systemic velocity offset (IRS3A: 5.3 km s^{-1}, IRS3B: 4.9 km s^{-1}), the well-ordered Keplerian disk of IRS3A, and relative alignment along the long axis of the natal core (Sadavoy & Stahler 2017), the systems would not likely have formed via the dynamical ejection scenario from the IRS3B system (Reipurth & Mikkola 2012).

In contrast, the triple system IRS3B appears to have originated via disk fragmentation. The well-organized $C^{17}O$ emission, which traces the disk continuum emission, indicates that the circum-multiple disk in IRS3B is in Keplerian rotation at both compact and extended spatial scales (0.″2 to >2.″0; 50 au to >600 au) (see Figure 4). The derived disk mass ($M_d/M_s \sim 25\%$) is high, such that the effects of self-gravity are important (Lin & Pringle 1990). The low-m (azimuthal wavenumber) spiral arms observed in the disk are consistent with the high mass (Kratter & Lodato 2016). The protostellar disk is provided stability on scales near the central potential due to the shear effects of Keplerian rotation and higher temperatures, while, at larger radii, the rotation velocity falls off and the local temperature is lower, allowing for local GI. Moreover, as seen in Figure 22, Toomre's Q falls below unity at radii >120 au, coincident with the spatial location of the tertiary IRS3B-c, as expected if recently formed via GI in the disk. Additionally the inner binary, IRS3B-ab, could have formed via disk fragmentation prior to the IRS3B-c, resulting in the well-ordered kinematics surrounding IRS3B-ab.

The PV analysis of IRS3B-c also suggests that the central mass of the tertiary continuum source is low enough (~0.02 $M_\odot$) to not significantly alter the kinematics of the disk (Figures 4 and 6).

The apparent coplanarity of IRS3B-abc and the well-organized kinematics of both the disk and envelope tracers, $C^{17}O$ and $H^{13}CO^+$, argue against the turbulent fragmentation pathway within the subsystem. The PV diagram of IRS3B-ab is well structured in various disk-tracing molecules, and the outflow orientation of IRS3B-c is aligned with the angular momentum vector of IRS3B-ab, making dynamical capture unlikely.

6.5. Protostar Masses

Comparing the masses of IRS3A (1.51 $M_\odot$) and IRS3B (1.15 $M_\odot$) to the initial mass function (young cluster initial mass function toward binaries; Chabrier 2005) shows these protostars will probably enter the main sequence as typical stars once mass accretion from the infalling envelope and massive disks completes. IRS3B-a and -b are likely to continue accreting matter from the disk and envelope and grow substantially in size.

In addition to the symmetry in the inner clumps, further analysis toward IRS3B-ab of the spatial location of the kinematic centers indicates that the kinematic center is consistent with being centered on the deficit ("deficit"; Figure 2) with a surrounding inner disk, where IRS3B-a is a bright clump moving into the inner disk. The continuum source IRS3B-b would be just outside the possible inner disk radius. These various kinematic centers are within one resolving element of the $C^{17}O$ beam, and thus we are unable to break the degeneracy of the results from these observations alone. Higher-resolution kinematics and continuum observations are required to understand the architecture of the inner disk and whether each dust clump corresponds to a protostar or whether the clumps are components of the inner disk and the central protostar is not apparent from dust emission in our observations.

If we assume the IRS3B-ab clumps surround a single central source, this source would most likely form an A-type ($M_* \approx$ 1.6–2.4 $M_\odot$) star, depending on the efficiency of accretion (10%–15%; Jørgensen et al. 2007). Similarly, IRS3A is likely to form an A-type star. If the IRS3B-ab clumps each represent a forming protostar, then each source would most likely form an F- or G-type ($M_* \approx$ 0.8–1.4 $M_\odot$) star depending on the ratio of the masses between the IRS3B-a and IRS3B-b components. IRS3B-c, while currently estimated to have a mass <0.2 $M_\odot$, could still accrete a substantial amount of mass of the disk and limit the accretion onto the central IRS3B-ab sources. This mechanism can operate without the need to open a gap (Artymowicz & Lubow 1996), which remains unobserved in these systems.

More recently, Maret et al. (2020) targeted seven class 0 protostars in Perseus with marginal resolution and sensitivities, to fit the molecular lines emission against Keplerian curves to derive protostellar masses. Their fitting method is similar to our own PV diagram fitting and has an average protostellar mass of ~0.5 $M_\odot$. If IRS3B-ab is a single-source protostar, then this source would be significantly higher mass ($M_* \sim 1.2\,M_\odot$) than the average mass of the sample, similar for IRS3A ($M_* \sim 1.4\,M_\odot$). However, if IRS3B-ab is a multiple protostellar source of two equal mass protostars ($M_* \sim 0.56\,M_\odot$), then these sources would be consistent with the survey's average protostellar mass. Maret et al. (2020) included IRS3B (labeled L1448-NB), using the molecules ^{13}CO, $C^{18}O$, and SO, and the protostellar parameters are consistent with the results we derived here ($M_* \sim 1.4\,M_\odot$, position angle ~ 29.°5, and $i \sim 45°$), despite lower sensitivities and resolutions compared with our observations.

Yen et al. (2017) targeted several well-known class 0 protostars and compared their stellar properties against other well-known sources (see reference Table 5 and Figure 10), to determine the star/disk evolution. They derived an empirical power-law relation for class 0 toward their observations $R_d = (44 \pm 8) \times \left(\frac{M_*}{0.1\,M_\odot}\right)^{0.8\pm0.14}$ au and a class 0+I relation of $R_d = (161 \pm 16) \times \left(\frac{M_*}{1.0\,M_\odot}\right)^{0.24\pm0.12}$ au. The L1448 IRS3B system, with a combined mass ~1.15 $M_\odot$, disk mass ~0.29 $M_\odot$, and FWHM Keplerian gaseous disk radius of ~300 au, positions the target well into the class 0 stage (~245–500 au for the Yen et al. 2017 relation) and ~2–3× the average stellar mass and radius of these other well-known targets. The protostellar mass of IRS3B is larger relative to the

sample of protostars observed in Yen et al. (2017), which had typical central masses of 0.2–0.5 $M_\odot$. However, this is the combined mass of the inner binary and each component could have a lower mass. L1448 IRS3A, which has a much more compact disk (FWHM Keplerian disk radius of ∼158 au) and a higher central mass than IRS3B (∼1.4 $M_\odot$), is more indicative of a class I source using these diagnostics. We note there is substantial scatter in the empirically derived relations (Tobin et al. 2020); thus the true correspondence of disk radii to an evolutionary state of the YSOs is highly uncertain and we observe no evidence for an evolutionary trend with disk radii.

6.6. Gravitational Potential Energy of IRS3B-c

In analyzing the gravitational stability of the IRS3B circumstellar disk, we can also analyze the stability of the clump surrounding IRS3B-c. If the clump around IRS3B-c is subvirial (i.e., not supported by thermal gas pressure) it would be likely unstable to gravitational collapse, undergoing rapid (dynamical timescale, $\tau_{\rm dyn}$) collapse resulting in elevated accretion rates compared with the collapse of virialized clumps. Additionally, it would be unlikely to observe this short-lived state during the first orbit of the clump. Dust clumps embedded within protostellar disks are expected to quickly ($t < 10^5 - {\rm yr}$) migrate from their initial position to a quasi-stable orbit much closer to the parent star (Vorobyov & Elbakyan 2019). Thus observing the IRS3B-c clump at the wide separation within the disk is likely due to it recently forming in situ. The virial theorem states $2E_{\rm kin} + E_{\rm pot} = 0$, or in other words we can define an $\mathcal{R}$ such that $\mathcal{R} := \frac{2E_{\rm kin}}{|E_{\rm pot}|}$ will be <1 for a gravitationally collapsing clump and >1 for a clump to undergo expansion. Assuming the ideal gas scenario of N particles, we arrive at $E_{\rm kin} = 1.5Nk_bT_{\rm clump}$, where k is the Planck constant and $T_{\rm clump}$ is the average temperature of the particles. The potential energy takes the classic form $E_{\rm pot} = \frac{-3}{5}\frac{GM_{\rm clump}^2}{R_{\rm clump}}$. We can define $N = \frac{M_{\rm clump}}{\mu m_{\rm H}}$, where μ is the mean molecular weight (2.37) and $m_{\rm H}$ is the mass of hydrogen. Assuming the clump is thermalized to the $T_{\rm peak} = 54.6$ K, the mass of the clump is 0.07 $M_\odot$, the upper bound for the IRS3B-c protostar is 0.2 $M_\odot$, and the diameter is 78.5 au (Table 3), we calculate $\mathcal{R} \approx 1.4$ for the dust clump alone (this $\mathcal{R}$ is likely an upper bound since our mass estimate for the dust is likely a lower limit due to the high optical depths) and ≈0.3 for the combined dust clump and protostar. (This $\mathcal{R}$ is likely a lower bound since our mass estimate for the protostar is an upper limit in order to remain consistent with the kinematic observations.) This indicates that the core could be virialized but could also reflect that a circumstellar accretion disk around IRS3B-c, or in the upper limit of the protostellar mass, could undergo contraction.

6.7. Mass Accretion

The mass in the circumstellar disks and envelopes provides a reservoir for additional mass transfer onto the protostars. However, this mass accretion can be reduced by mass outflow due to protostellar winds; thus we need to determine the maximal mass transport rate of the system to determine whether winds are needed to carry away momentum (Wilkin & Stahler 1998). While these observations do not place a direct constraint on $\dot{M}$, from our constraints on M_* and the observed total luminosity we can estimate the mass accretion rate. In a viscous, accreting disk, the total luminosity is the sum of the stellar and accretion luminosity:

$$L_{\rm bol} \sim L_* + L_{\rm acc}, \tag{6}$$

and the $L_{\rm acc}$ is

$$L_{\rm acc} = \frac{GM_*\dot{M}}{R_*}, \tag{7}$$

half of which is liberated through the accretion disk and half of which is emitted from the stellar surface. From our observations, we can directly constrain the stellar mass, and thus, using the stellar birth line in Hartmann et al. (1997) (adopting the models with protostellar surface cooling that provides lower-estimates), we can estimate the protostellar radius. From these calculations we can estimate the mass accretion rate of the protostars. The results are tabulated in Table 6 but are also summarized here. For the single protostar IRS3A this is straightforward, but for the binary source IRS3B-ab, care must be taken. We adopt the two scenarios for the system configuration: (1) the protostellar masses are equally divided (two 0.575 $M_\odot$ protostars) and (2) one protostar dominates the potential (one 1.15 $M_\odot$ protostar). From Figure 3 in Hartmann et al. (1997), we estimate the stellar radius to be 2.5 $R_\odot$, 2.5 $R_\odot$, and 2 $R_\odot$ for stellar masses 0.575 $M_\odot$, 1.15 $M_\odot$, and 1.51 $M_\odot$, respectively. From Figure 3 in Hartmann et al. (1997), we estimate the stellar luminosity to be 1.9 $L_\odot$, 3.6 $L_\odot$, and 2.5 $L_\odot$ for stellar masses 0.575 $M_\odot$, 1.15 $M_\odot$, and 1.4 $M_\odot$, respectively (see Section 3.2).

Considering the bolometric luminosities for IRS3B and IRS3A given in Section 3.2, we find the $\dot{M} \sim 4.95 \times 10^{-7}$ $M_\odot$ yr^{-1} for IRS3A. Then for IRS3B-ab, in the first scenario (two 0.575 $M_\odot$ protostars), we find $\dot{M} \sim 1.5 \times 10^{-6}$ $M_\odot$ yr^{-1}, and in the second scenario (one 1.15 $M_\odot$ protostar), we find $\dot{M} \sim 6.6 \times 10^{-7}$ $M_\odot$ yr^{-1}. These accretion rates are unable to build up the observed protostellar masses within the typical lifetime of the class 0 stage (∼160 kyr) and thus require periods of higher accretion events to explain the observed protostellar masses. This possibly indicates that the IRS3B-ab system is more consistent as an equal mass binary system. However, further, more sensitive, and higher-resolution observations to fully resolve out the dynamics of the inner disk are needed to fully characterize the sources.

Table 6
Mass Accretion

Source	$L_{\rm bol}$ ($L_\odot$)	M_* ($M_\odot$)	R_* ($R_\odot$)	L_* ($L_\odot$)	$\dot{M}_{\rm acc}$ (10^{-7} $M_\odot$ yr^{-1})
IRS3B-ab[a]	13.0[b]	(0.575, 1.2)	(2.5, 2.5)	(1.91, 3.57)	(15.3, 6.56)
IRS3A	14.4[b]	1.5	2	2.53	5.43

Notes. Summary of the derived parameters from Hartmann et al. (1997) to estimate the amount of mass accretion that is consistent with protostellar models and the observations. The methodology for estimating R_*, L_*, $\dot{M}$, and $M_{\rm accreted}$ is provided in Section 6.7.

[a] When constraining R_*, L_*, $\dot{M}$, and $M_{\rm accreted}$, IRS3B can be analyzed in two scenarios, (1) equally mass binary and (2) one protostar with most of the mass; we reference these delineations as (equal mass, single massive protostar), respectively.

[b] The bolometric luminosity is scaled to a distance of 288 pc from Tobin et al. (2016b).

We further compare the accretion rates derived here with a similar survey toward class 0+I protostars (Yen et al. 2017). We find IRS3A is consistent with L1489 IRS, a class I protostar with a $M_* \sim 1.6\,M_\odot$ (Green et al. 2013) and a $\dot{M} \sim 2.3 \times 10^{-7}$ $M_\odot$ yr^{-1} (Yen et al. 2014). Furthermore, in the case IRS3B-ab is an equal mass binary, the derived accretion rates as compared with the sources in Yen et al. (2017) are in the upper echelon of rates. However, in the case IRS3B-ab is best described as a single-mass protostar, the derived accretion rates are consistent with TMC-1 and TMC-1A, other class 0+I sources in Yen et al. (2017).

While the currently estimated accretion rates for IRS3B and IRS3A would not be able to assemble the observed protostar masses in the lifetime of a class 0 protostar, accretion rates are not necessarily constant through the protostellar phase. The well-known FU Orionis phenomena are exemplary examples of nonsteady accretion in protostars (e.g., Hartmann & Kenyon 1996; Audard et al. 2014). Accretion bursts have also been observed in both class I and class 0 protostars in recent years (Fischer et al. 2013; Safron et al. 2015). GI in disks has been proposed as a mechanism to drive outburts with the accretion of clumps of material from the disks (Stamatellos et al. 2011; Dunham et al. 2014; Vorobyov et al. 2014; Mercer & Stamatellos 2017; Sharma et al. 2020). In this scenario, the accretion luminosity increases quickly, stabilizing the disks. After the accretion event has finished, the protostars undergo a "quiescent" stage, while the disk can redevelop GIs and fragment. Two possible signatures for this mechanism would be in the outflow configuration: bipolar jets with periodically spaced knots and GIs of the disk. IRS3B does exhibit a gravitationally unstable disk (Section 6.3.1), but the outflow, while having many bright features (see Appendix D) does not show periodically spaced knots like the example from Plunkett et al. (2015). Thus, it is possible that both IRS3B and IRS3A have undergone past accretion bursts, helping to explain their current masses and relatively low inferred accretion rates, but they do not currently exhibit features of outbursting protostars and we cannot unequivocally state that they have undergone past outbursts.

7. Summary

We present the highest sensitivity and resolution observations tracing the disk kinematics toward L1448 IRS3B and IRS3A to date, $C^{17}O/C^{18}O$ comparison: $\sim$5$\times$ higher S/N at 4.0 km s^{-1}, $\sim$3$\times$ higher resolution, and $\sim$2$\times$ better velocity resolution compared with Tobin et al. (2016a). Our observations resolve three dust continuum sources within the circum-multiple disk with spiral structure and trace the kinematic structures using $C^{17}O$, $H^{13}CN/SO_2$, and $H^{13}CO^+$ surrounding the protomultiple sources. The central gravitating mass in IRS3B, near -a and -b, dominates the potential as shown by the organized rotation in $C^{17}O$ emission. We compare the high-fidelity observations with radiative transfer models of the line emission components of the disk. The presence of the tertiary source within the circum-multiple disk, detection of dust continuum spiral arms, and the Toomre Q analysis are indicative of the disk around IRS3B being gravitationally unstable.

We summarize our empirical and modeled results:

1. We resolve the spiral arm structure of IRS3B with high fidelity and observed IRS3B-c, the tertiary, to be embedded within one of the spiral arms. Furthermore, a possible symmetric inner disk and inner depression are marginally resolved near IRS3B-ab. IRS3B-b may be a high-density clump just outside of the inner disk. We also marginally resolve possible spiral substructure in the disk of IRS3A. We calculate the mass of the disk surrounding IRS3B to be $\sim$0.29 $M_\odot$ with $\sim$0.07 $M_\odot$ surrounding the tertiary companion, IRS3B-c. IRS3A has a disk mass of $\sim$0.04 $M_\odot$.
2. We found that the $C^{17}O$ emission is indicative of Keplerian rotation at the scale of the continuum disk and fit a central mass of $1.15^{+0.09}_{-0.09}$ $M_\odot$ for IRS3B using a fit to the PV diagram. $H^{13}CO^+$ traces the larger structure, corresponding to the outer disk and inner envelope for IRS3B. Meanwhile, the $H^{13}CN/SO_2$ blended line most likely reflects SO_2 emission, tracing outflow launch locations near IRS3B-c. The *pdspy* modeling of IRS3B finds a mass of $1.19^{+0.13}_{-0.07}$ $M_\odot$, comparable to the PV diagram fit of $1.15^{+0.09}_{-0.09}$ $M_\odot$.
3. We find that the tertiary companion is forming a central protostar that is $<$0.2 $M_\odot$. This upper limit is based on its lack of significant disturbance of the disk kinematics. Moreover, we find that there is a jet originating from the clump, confirming that a protostar is present.
4. For IRS3A, the $H^{13}CN/SO_2$ emission likely reflects $H^{13}CN$ emission due to a consistent velocity with $C^{17}O$. $H^{13}CN$ emission indicates Keplerian rotation at the scale of the continuum disk corresponding to a central mass of 1.4 $M_\odot$. The molecular line, $C^{17}O$, is also detected but is much fainter in the source but consistent with a central mass result of 1.4 $M_\odot$. The *pdspy* modeling fit for IRS3A yields mass $1.51^{+0.06}_{-0.07}$ $M_\odot$, which is also comparable to the PV diagram estimate of 1.4 $M_\odot$.
5. The azimuthally averaged radial surface density profiles enable us to analyze the gravitational stability as a function of radius for the disks of IRS3B and IRS3A. We find the circum-multiple disk of IRS3B is gravitationally unstable ($Q < 1$) for radii $>$120 au. We find the protostellar disk of IRS3A is gravitationally stable ($Q > 5$) for the entire disk. We marginally detect substructure in IRS3A, but at our resolution, we cannot definitely differentiate between spiral structure and a gap in the disk. If the substructure is spiral arms due to GIs, then the disk mass must be underestimated by a factor of 2–4 from our Toomre Q analysis.

Through the presented analysis, we determine the most probable formation pathway for the IRS3B and its spiral structure is through the self-gravity and fragmentation of its massive disk. The larger IRS3A/B system (including the even wider companion L1448 NW) likely formed via turbulent fragmentation of the core during the early core collapse, as evidenced by the nearly orthogonal disk orientation and different system velocity for IRS3A and IRS3B.

We thank the anonymous reviewer for helpful comments. N.R. and J.T. acknowledge funding from NSF grant AST-1814762. This work is supported in part by NSF AST-1910364. Z.L. is supported in part by NSF AST-1716259 and NASA 80NSSC20K0533. K.M.K. acknowledges support from NASA Grant 80NSSC18K0726. P.D.S acknowledges support from NSF AST-2001830. This paper makes use of the following ALMA data: 2016.1.01520.S. ALMA is a

partnership of ESO (representing its member states), NSF (USA), and NINS (Japan), together with NRC (Canada), MOST and ASIAA (Taiwan), and KASI (Republic of Korea), in cooperation with the Republic of Chile. The Joint ALMA Observatory is operated by ESO, AUI/NRAO, and NAOJ. The National Radio Astronomy Observatory is a facility of the National Science Foundation operated under cooperative agreement by Associated Universities, Inc. The computing for this project was performed at the University of Oklahoma Supercomputing Center for Education and Research. This research has made use of NASA's Astrophysics Data System. This research made use of APLpy, an open-source plotting package for Python.

Facility: ALMA.

Software: Numpy (Harris et al. 2020), scipy (Virtanen et al. 2019), emcee (Foreman-Mackey et al. 2013), Matplotlib (Hunter 2007), Astropy (Astropy Collaboration et al. 2013; Price-Whelan et al. 2018), APLpy (Robitaille & Bressert 2012), pdspy (Sheehan et al. 2019), CASA (McMullin et al. 2007).

Appendix A
Observations

The ALMA correlator was configured to observe ^{12}CO ($J = 3 \rightarrow 2$), C^{17}O ($J = 3 \rightarrow 2$), H^{13}CO^{+} ($J = 4 \rightarrow 3$), H^{13}CN ($J = 4 \rightarrow 3$), SiO ($J = 7 \rightarrow 6$), and a broad 2 GHz continuum band centered at 335.5 GHz (894 μm). A summary of the correlator setup is provided in Table 2. The raw data were reduced using the Cycle 4 ALMA pipeline within the Common Astronomy Software Application (CASA) (McMullin et al. 2007) version 4.7.0. All further processing was done using the CASA version 4.7.2, and the reduction sequence is described here. To maximize the sensitivity of the continuum observations, emission-free channels from the higher-resolution windows were added to the continuum after appropriate flagging of line emission. The total bandwidth recovered from this method was ~1.2 GHz, which, in conjunction with the continuum spectral window bandwidth of 1.875 GHz, yields ~3 GHz of aggregate continuum bandwidth with an average frequency center of 341.0 GHz. Given the high S/N of the sources, we performed self-calibration (summary to reproduce in Table 7) on the separate configurations (C40-3 and C40-6) to further increase the S/N by correcting short timescale phase and amplitude fluctuations. During the phase-only self-calibration, the solution intervals for each additional iteration were "inf" (the entire scan length, dictated by the time on a single pointing), 30.25 s (5 integrations), and 12.1 s (2 integrations). During the amplitude self-calibration, the solution interval of "inf" was used. The final self-calibrated measurement sets from the two configurations were concatenated using the CASA task *concat*. The resulting images were generated from this concatenated data set using *Briggs weighting* with a *robust* parameter of 0.5 (Figure 1). The beam size of the combined continuum image is $0\farcs11 \times 0\farcs05$ (32 × 15 au). We achieved 69 μJy beam^{-1} sensitivity for the aggregate continuum data, and the full list of frequencies, bandwidths, beam sizes, sensitivities, and tapering for the suite of molecules is provided in Table 2.

During the high-resolution execution, the central frequency of the SiO spectral window was set to 347.01 GHz with a bandwidth of 469 MHz, falling outside of the emission range for the target molecule. However, for the C40-3 configuration, the spectral setup was corrected and SiO was observed.

Table 7
Self-calibration

Step	Rms (mJy beam^{-1})	IRS3B S/N	IRS3A S/N	Iterations	Solution Integration (s)
No-selfcal.	6.5 | 74	82 | 43	26 | 13	100 | 100	
phase-cal. 1	4.2 | 25	140 | 140	48 | 40	100 | 110	"inf"
phase-cal. 2	1.7 | 11	310 | 330	120 | 100	300 | 500	30.25
phase-cal. 3	1.3 | 5.8	540 | 620	200 | 190	3000 | 1500	12.1
ampl.-cal.	0.7 | 4.3	1000 | 840	390 | 260	2500 | 2500	"inf"

Note. Summary of the parameters required to reproduce the gain and amplitude self-calibrations. The configurations are delineated as C40-6 | C40-3, respectively, in the table. "inf" indicates the entire scan length, dictated by the time on a single pointing, which is typically 6.05 s.

Appendix B
Optimal Disk-tracing Molecular lines

To infer properties about the central potential from the circumstellar disk characteristics, we must disentangle the envelope and disk kinematics from the molecular line emission. Previous observations conducted by Tobin et al. (2016a) of IRS3B included molecular lines $C^{18}O$ and ^{13}CO. However, while emission from $C^{18}O$ spatially coincides with the disk and is optically thin, it can have resolved-out emission toward the molecular line center, underrepresenting the underlying gas structure and reducing the fidelity of the tracer (Booth & Ilee 2020). Furthermore, ^{13}CO is a poor kinematic tracer for embedded class 0 disks because it is a more abundant molecule that will have a high optical depth (and subsequently a larger degree of spatial filtering, which limits the velocity range it is sensitive to) and confusion with the outflow. This tracer is better suited toward more evolved class I sources (possibly IRS3A). Combining all previous observations of the sources, we find $C^{17}O$ is possibly the best tracer for class 0 disks, being the least abundant molecule and thus experiencing the least amount of spatial filtering, both of which allow for accurate emission reconstruction near the line center. However, due to the low abundance, this molecule requires substantial integration time and is not suited for class I disks.

Appendix C
Application of Radiative Transfer Models

We generate a set of *priors* for the protostellar parameters based on the observational constraints. These *priors* are then sampled via a uniform distribution and fed into *emcee* to generate the samples, each sample describing a unique set of model parameters. These parameters are used to generate synthetic channel maps for the lines of interest, computed with RADMC-3D. These synthetic data cubes are Fourier transformed to recover a synthetic visibility data set. These are regridded and subsequently cross-compared with the observed data in the uv-plane. The likelihood of the parameters for this comparison is then updated internally, and the MCMC either probabilistically accepts the sample and migrates to this new point or does not accept it by comparing the new likelihood to the previous sample. The whole process is repeated until convergence.

We assume the kinematic rotation of the disk is described by a Keplerian orbit, with an azimuthal velocity (in cylindrical coordinates) of $V(R) = \sqrt{GM_*/R}$. We assume the molecular line emission comes from a flared disk geometry as motivated by viscous and irradiated disk evolution, where the mass density profile is described, in cylindrical coordinates with the origin at the gravitational source, by the equation

$$\rho(R, z) = \frac{\Sigma(R)}{\sqrt{2\pi}h(R)} \exp\left(-0.5\left(\frac{z}{h(R)}\right)^2\right), \quad \text{(C1)}$$

where R is the distance in the radial direction in cylindrical coordinates, Σ is the surface mass density of each molecule species, and h is the disk scale height. We assume the disk can be described via a power-law surface mass density profile that is truncated at some outer radius, of the form

$$\Sigma(R) = \Sigma_0 \times R^{-\gamma}. \quad \text{(C2)}$$

We also define

$$\Sigma_0 = \frac{(2-\gamma)M_{\rm disk}}{2\pi(R_{\rm out}^{2-\gamma} - R_{\rm in}^{2-\gamma})}, \quad \text{(C3)}$$

where $R_{\rm out}$ is the outer cutoff radius, $R_{\rm in}$ is the inner cutoff radius, and γ is the surface density power-law exponent.

Another assumption we make is that the vertical structure of the disk is set by local hydrostatic equilibrium with a vertically isothermal temperature profile and a radial power-law temperature profile of the form

$$T(R) = T_0\left(\frac{R}{1\ {\rm au}}\right)^{-q}, \quad \text{(C4)}$$

which then sets the scale height of the disk, under the balance of thermal pressure and gravity, to be

$$h(R) = \left(\frac{k_b R^3 T(R)}{GM_*\mu m_{\rm H}}\right)^{1/2}, \quad \text{(C5)}$$

where k_b is the Boltzmann constant, G is the gravitational constant, $m_{\rm H}$ is the mass of hydrogen, and μ is the mean molecular weight (assuming classic protostellar mean molecular weight, $\mu \approx 2.37$; Lodders 2003). Additionally, chemical variations such as gas freeze-out onto dust grains toward the midplane and outer disk are excluded from the models.

Combining the aforementioned parameters that describe the disk structure plus the inclusion of disk geometric orientations, we have the following free parameters: position angle (p.a.), inclination (inc.), temperature (T_0), stellar mass (M_*), disk radius (R_D), disk mass ($M_{\rm disk}$), surface density power law (γ), system source velocity ($V_{\rm sys}$), and uniform microturbulent line broadening (α) (Table 5). Furthermore, we have a number of fixed parameters that are used throughout the models but are not fit: molecular gas-to-H_2 abundance ratio (for IRS3B $C^{17}O = 5.88 \times 10^{-8}$; for IRS3A $H^{13}CN = 2.04 \times 10^{-7}$), inner disk cutoff radius ($R_{\rm in} = 0.1$ au), and the temperature power-law index ($q = 0.35$).

The combined fitting is computationally expensive, requiring on order 10^4 core-hours to reach convergence. A bulk of the computation time (up to 10 minutes per individual model) is used when RADMC-3D attempts to ray trace massive disks.

Appendix D
Outflows

D.1. ^{12}CO Line Emission

The second most abundant molecule to H_2, ^{12}CO, is shown as moment 0 maps in Figures 24–26. The ^{12}CO integrated intensity maps toward IRS3B (Figures 24 and 25) show clear signs of a collimated outflow originating from a region near IRS3B-ab and IRS3B-c that extends to $\sim 20''$. Outflows are thought to be a signature of stellar birth with the highest-velocity outflows ($>20\,{\rm km\,s^{-1}}$) and high collimation frequently found toward class 0 protostars (Andre et al. 1993). We observe asymmetric emission of the ^{12}CO outflows with excess redshifted emission dominating the data cube. The low-velocity outflows appear to originate from IRS3B-ab, while the high-velocity jets appear to originate from both IRS3B-ab and -c. The outflows from IRS3B-ab and IRS3B-c are highly entangled at the lower-velocity emission ($<10\,{\rm km\,s^{-1}}$) but become more easily separated at higher-velocity emission

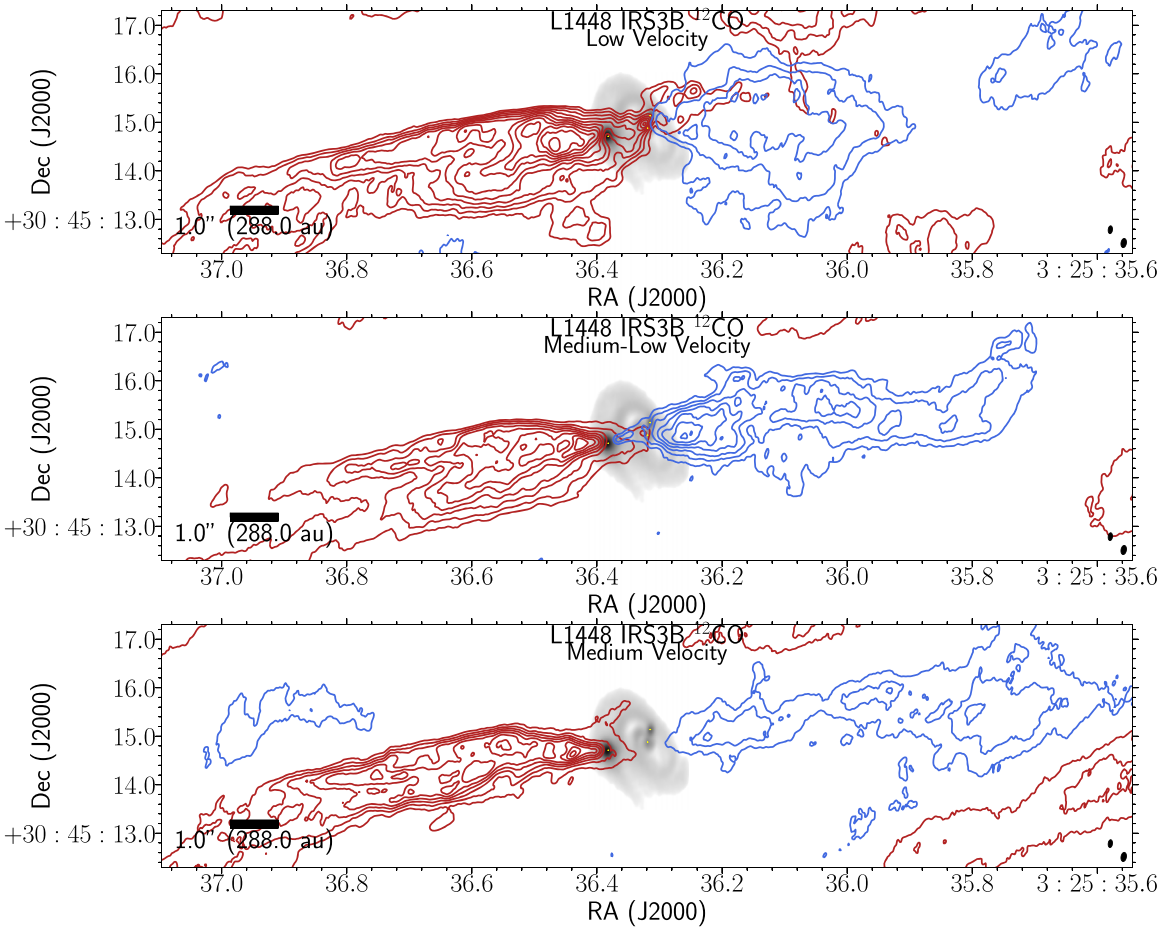

Figure 24. Moment 0 map (integrated intensity) of ^{12}CO, overlaid on the continuum (gray scale) image from Figure 1, split up according to velocity ranges, providing exquisite detailing of the location and collimation of the IRS3B outflows. The central outflow from IRS3B extends 10″ (2880 au), beyond the edge of the primary beam of ALMA at 879 μm, from launch location on either side. The panels correspond to low-, medium-low, and medium-velocity ranges. The following panel descriptions will be noted red (blue), corresponding to the Doppler shifted emission. Low velocity: velocity ranges 5.5 → 10.5 km s^{-1} (4 → −1 km s^{-1}), contours start at 3σ (3σ) and iterate by 2σ (2σ) with the 1σ level starting at 0.1 (0.1) Jy beam^{-1} for the red (blue) channels. Medium-low velocity: velocity ranges 10.5 → 15.5 km s^{-1} (−6 → −4 km s^{-1}), contours start at 5σ (5σ) and iterate by 3σ (2σ) with the 1σ level starting at 0.04 (0.004) Jy beam^{-1} for the red (blue) channelsy. Medium velocity: velocity ranges 15.5 → 20.5 km s^{-1} (−11 → −6 km s^{-1}), contours start at 10σ (10σ) and iterate by 4σ (4σ) with the 1σ level starting at 0.02 (0.02) Jy beam^{-1} for the red (blue) channelsy. The ^{12}CO synthesized beam (0.″19 × 0.″11) is the bottom rightmost overlay on each of the panels, and the continuum synthesized beam (0.″11 × 0.″05) is offset diagonally.

(>20 km s^{-1}). The outflows of IRS3B-ab and IRS3B-c appear aligned within the wide opening angle (∼45°) of the IRS3B-ab emission. However, both of these sources are marginally misaligned from the IRS3B-ab continuum disk minor axis (<10°). In the blueshifted emission, there appears a faint but very wide opening angle (∼65°) for the outflows, which is resolved out in these observations but more clear in Tobin et al. (2016a). Additionally, there is a crescent-shaped overdensity along the blueshifted emission, which could be due to orbital movement of the tertiary and/or precessions of the outflows. In the redshifted emission there are three main overdensities that occur along the line of the outflow, possibly indicative of irregular, high accretion events in the past. ^{12}CO integrated intensity maps toward IRS3A (Figure 26) show low-velocity, wide-angle outflows toward line center, unlike the collimated outflows toward IRS3B.

D.2. SiO Line Emission

The SiO emission (Figures 27 and 28) corresponds to shocks along the outflow. SiO most probably forms via dust grain sputtering, which can inject either silicon atoms or SiO molecules into the gas (Caselli et al. 1997). This happens from neutral particle impacts on charged grains in addition to grain-grain collisions at sufficient velocities (25–35 km s^{-1}; Caselli et al. 1997). Furthermore, we observe a relatively high asymmetry in the emission intensity between the red- and blueshifted emission, while the radial extent (distance from launch location) is more symmetric about the outflow launch origin. Unlike the ^{12}CO emission, the outflow launch location from SiO seems to coincide with IRS3B-c for both the high- and low-velocity emission rather than IRS3B-ab. However, the lower resolution leaves some ambiguity as to the true launch location.

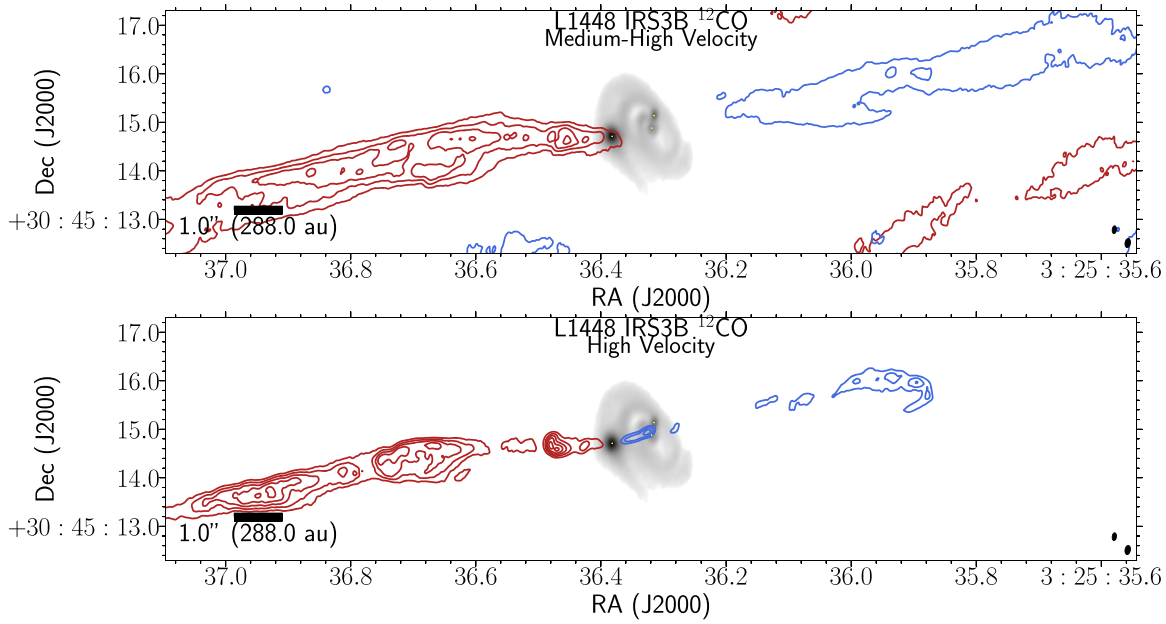

Figure 25. Same as Figure 24 but for the medium-high velocity: velocity ranges 20.5 → 25.5 km s^{-1} (−16 → −11 km s^{-1}), contours start at 3σ (3σ) and iterate by 4σ (4σ) with the 1σ level starting at 0.04 (0.04) Jy beam^{-1} for the red (blue) channels. High velocity: velocity ranges 25.5 → 30.5 km s^{-1} (−21 → −16 km s^{-1}), contours start at 5σ (5σ) and iterate by 2σ (2σ) with the 1σ level starting at 0.04 (0.04) Jy beam^{-1} for the red (blue) channels. The ^{12}CO synthesized beam (0.″19 × 0.″11) is the bottom rightmost overlay on each of the panels, and the continuum synthesized beam (0.″11 × 0.″05) is offset diagonally.

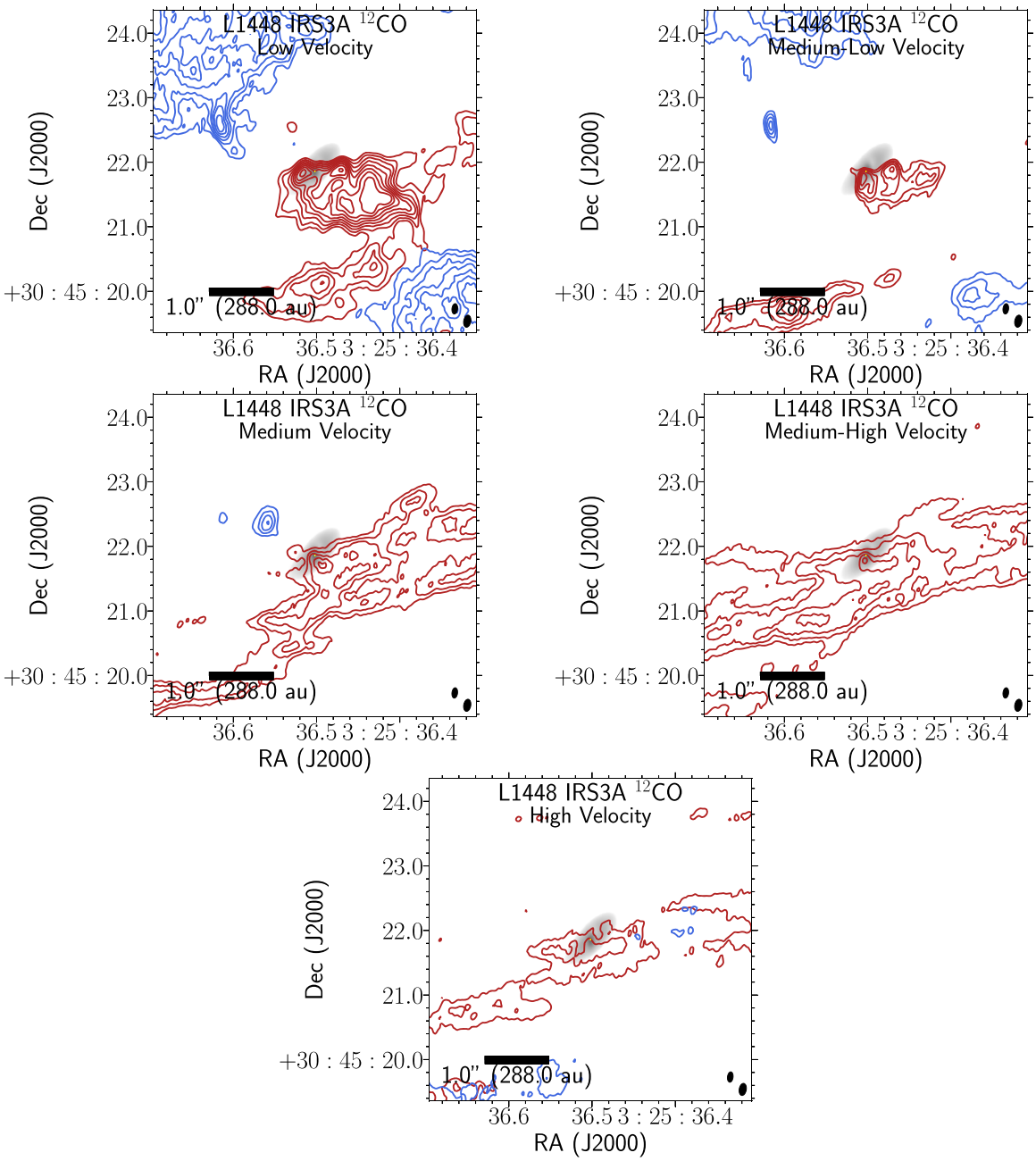

Figure 26. Similar to Figures 24 and 25 toward the IRS3A source with the same velocity ranges. Low velocity: velocity ranges 5.5 → 10.5 km s^{-1} (4 → −1 km s^{-1}), contours start at 5σ (5σ) and iterate by 4σ (2σ) with the 1σ level starting at 0.1 (0.1) Jy beam^{-1} for the red (blue) channels. Medium-low velocity: velocity ranges 10.5 → 15.5 km s^{-1} (−6 → −4 km s^{-1}), contours start at 5σ (5σ) and iterate by 2σ (2σ) with the 1σ level starting at 0.04 (0.004) Jy beam^{-1} for the red (blue) channels. Medium velocity: velocity ranges 15.5 → 20.5 km s^{-1} (−11 → −6 km s^{-1}), contours start at 5σ (5σ) and iterate by 2σ (2σ) with the 1σ level starting at 0.02 (0.02) Jy beam^{-1} for the red (blue) channels. Medium-high velocity: velocity ranges 20.5 → 25.5 km s^{-1} (−16 → −11 km s^{-1}), contours start at 3σ (3σ) and iterate by 2σ (2σ) with the 1σ level starting at 0.04 (0.04) Jy beam^{-1} for the red (blue) channels. High velocity: velocity ranges 25.5 → 30.5 km s^{-1} (−21 → −16 km s^{-1}), contours start at 3σ (3σ) and iterate by 2σ (2σ) with the 1σ level starting at 0.04 (0.04) Jy beam^{-1} for the red (blue) channels. The ^{12}CO synthesized beam (0.″19 × 0.″11) is the bottom rightmost overlay on each of the panels, and the continuum synthesized beam (0.″11 × 0.″05) is offset diagonally.

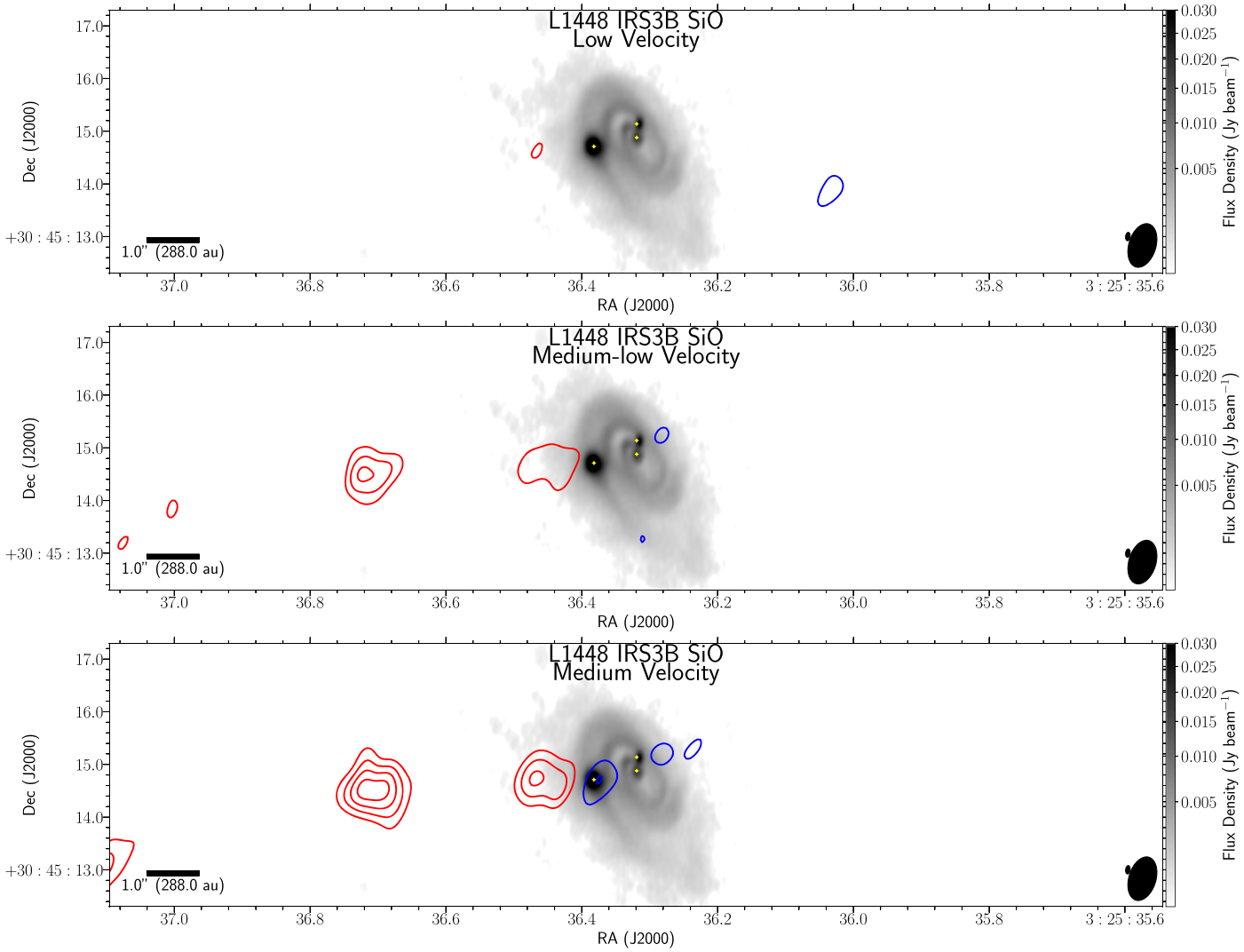

Figure 27. Moment 0 map (integrated intensity) of SiO, overlaid on the continuum (gray scale) image from Figure 1. SiO shows locations of shocked gas fronts. The panels correspond to low-, medium-low, and medium-velocity ranges. The following panel descriptions will be noted red (blue), corresponding to the Doppler shifted emission. Low velocity: velocity ranges 5.5 → 10.5 km s^{-1} (4 → −1 km s^{-1}), contours start at 5σ (5σ) and iterate by 3σ (3σ) with the 1σ level starting at 0.11 (0.09) Jy beam^{-1} for the red (blue) channels. Medium-low velocity: velocity ranges 10.5 → 15.5 km s^{-1} (−6 → −4 km s^{-1}), contours start at 5σ (5σ) and iterate by 3σ (3σ) with the 1σ level starting at 0.01 (0.01) Jy beam^{-1} for the red (blue) channels. Medium velocity: velocity ranges 15.5 → 20.5 km s^{-1} (−11 → −6 km s^{-1}), contours start at 5σ (5σ) and iterate by 3σ (3σ) with the 1σ level starting at 0.009 (0.012) Jy beam^{-1} for the red (blue) channels. The SiO synthesized beam (0.″85 × 0.″52) is the bottom rightmost overlay on each of the panels, and the continuum synthesized beam (0.″11 × 0.″05) is offset diagonally.

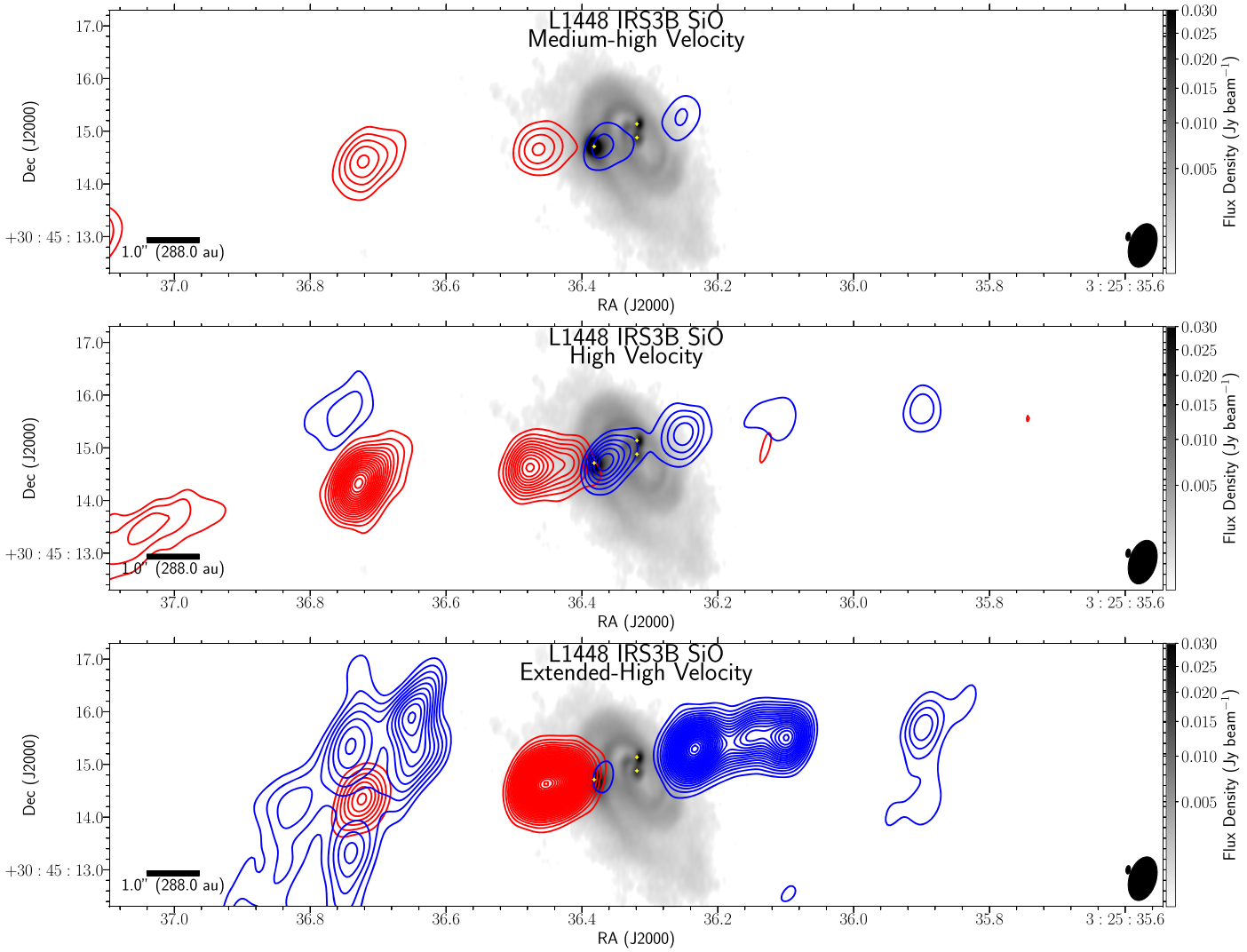

Figure 28. Similar to Figure 27 but for the medium-high velocity: velocity ranges 20.5 → 25.5 km s^{-1} (−16 → −11 km s^{-1}), contours start at 5σ (5σ) and iterate by 3σ (3σ) with the 1σ level starting at 0.012 (0.015) Jy beam^{-1} for the red (blue) channels. High velocity: velocity ranges 25.5 → 30.5 km s^{-1} (−21 → −16 km s^{-1}), contours start at 5σ (5σ) and iterate by 3σ (3σ) with the 1σ level starting at 0.008 (0.015) Jy beam^{-1} for the red (blue) channels. Extended high velocity: velocity ranges 30.5 → 50 km s^{-1} (−40 → −21 km s^{-1}), contours start at 5σ (5σ) and iterate by 3σ (3σ) with the 1σ level starting at 0.025 (0.025) Jy beam^{-1} for the red (blue) channels. There is significant blueshifted emission on the eastern side of the image, in the same location as the redshifted outflow, which is coming from the L1448-C outflow, located ∼3′ south of L1448 IRS3B. The SiO has additional emission well beyond the velocity range of the emission in ^{12}CO and is presented as an additional panel ("extended-high velocity"), which only features the redshifted emission. The SiO synthesized beam (0.″85 × 0.″52) is the bottom rightmost overlay on each of the panels, and the continuum synthesized beam (0.″11 × 0.″05) is offset diagonally.

Appendix E
Molecular Line Spectra

In order to visualize the structure and dynamics in 3D data cubes, we construct moment 0 maps and PV diagrams to reduce the number of axis by either integrating along the frequency axis or along slices across the minor axis, respectively. We can also construct spectra, centered on the sources, and integrated radially outward in annuli.

Figure 29 is the C^{17}O spectrum for the IRS3B-c system. We extract the emission within an ellipse centered on IRS3B-c to define the main core of the IRS3B-c spectrum in red and an annulus just outside of this ellipse to define the comparative IRS3B-ab disk spectrum in red. The IRS3B-c spectrum features a deficit of emission toward line center due to the high optical depths toward this clump. Figure 30 is the C^{17}O spectrum for the IRS3B system. This spectrum is centered on the kinematic center of the disk (Table 4) and is integrated out to the size of the gaseous disk (Table 3). Figure 31 is the C^{17}O emission toward IRS3A, which is faint in these observations, making it not a suitable molecule for tracing disk kinematics.

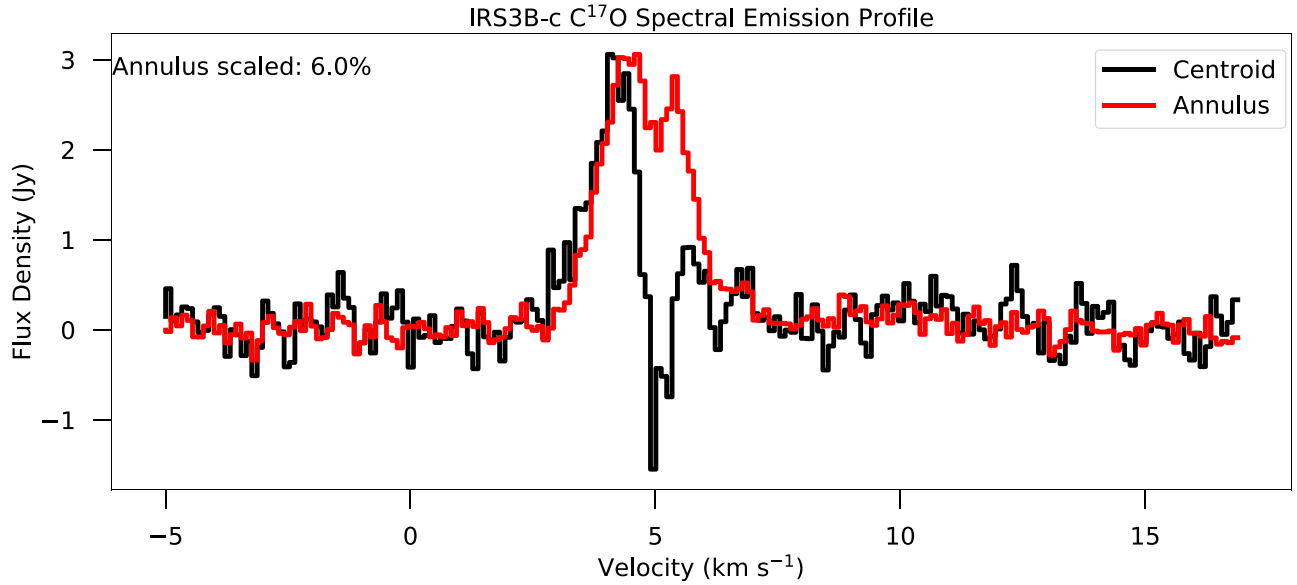

Figure 29. $C^{17}O$ integrated spectral emission profile of IRS3B-c, set to the rest frequency of $C^{17}O$. The profiles were extracted by integrating the emission within an annulus, where the co-center of the annuli is set to the center point of IRS3B-c, while the inclination and position angle of the annulus are set to the IRS3B-ab parameters. The black profile is extracted from a central ellipse 2 times the size of the restoring beam, while the red profile is extracted from an annulus with the same width as the average restoring beam, three beam widths off of the source. The central emission features a deficit of emission toward line center. The profiles are normalized to highlight the emission profiles rather than the actual values of the emission.

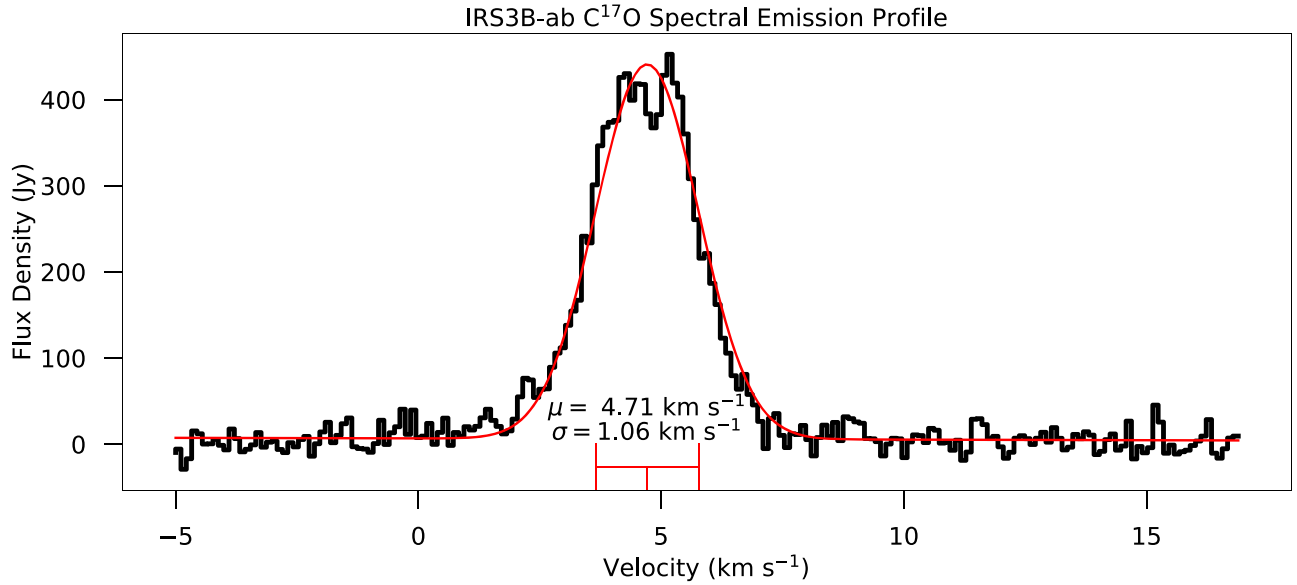

Figure 30. $C^{17}O$ integrated spectral emission profile of IRS3B-ab, set to the rest frequency of $C^{17}O$. The profile is extracted by integrating the emission within an ellipse, where the center, inclination, and position angle are set to the center point of IRS3B-ab. The black profile is extracted from a central ellipse the same size as the gaseous disk in Table 3. The red line is a Gaussian fit to the spectra, with parameters $\mu = 4.71^{+0.02}_{-0.02}$ km s^{-1} and $\sigma = 1.06^{+0.02}_{-0.02}$ km s^{-1}.

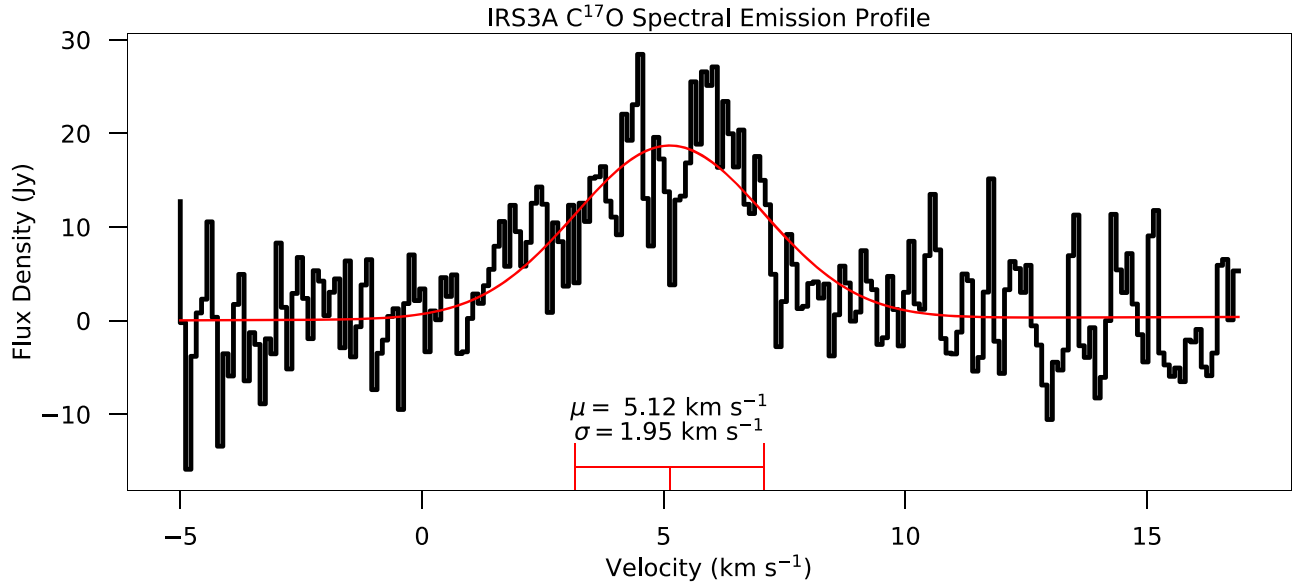

Figure 31. $C^{17}O$ integrated spectral emission profile of IRS3A, set to the rest frequency of $C^{17}O$. The profiles were extracted by integrating the emission within an ellipse, where the center, inclination, and position angle are set to the center point of IRS3A. The black profile is extracted from a central ellipse the same size as the gaseous disk in Table 3. The $C^{17}O$ emission toward this source is fainter than the emission from other dense gas tracers, thought to trace disk kinematics like that of $H^{13}CN$. The red line is a Gaussian fit to the spectrum, with parameters $\mu = 5.12^{+0.15}_{-0.15}$ km s^{-1} and $\sigma = 1.95^{+0.75}_{-0.17}$ km s^{-1}.

Appendix F
Tertiary Subtraction and Gaussian Fitting

The continuum emission of the bright, embedded source, IRS3B-c, biases the analysis of the radial disk structure and circumstellar disk mass estimate of the IRS3B system. By removing this source, we can independently examine the disk and the tertiary source in order to characterize their properties separately (Figure 32). In order to remove the tertiary source, we fit two Gaussians with a zero-level offset to the position of the source using the *imfit* task in CASA (a point source and single Gaussian did not provide adequate fit while preserving the underlying disk emission). The offset serves to preserve the emission from the underlying IRS3B-ab disk emission. We also restricted the *imfit* task to a $0\farcs8 \times 0\farcs7$ ellipse around the source such that the fit does not extend into the surrounding emission from the spiral arms. With these parameters generated from the *imfit* task, we then constructed a model image of the tertiary. We used the CASA task *setjy* to Fourier transform the model image and fill the model column of the measurement set with the model visibility data. We then use the task *uvsub* to subtract this model from the data, producing the residual visibilities without the tertiary. A tertiary subtracted image is generated from this residual data set and shown in Figure 32 along with the model of the tertiary used to construct this data set. The masses generated from this fit are $\sim$0.07 $M_\odot$, as described in Section 3.1 and provided in Table 4. We then are able to reconstruct and taper the resulting visibilities to smooth over the substructure of the disk, in order to better fit the circum-multiple disk. The image (Figure 33) is fit with a 2D Gaussian using the *imfit* in CASA, and the results of the fit are provided in Table 3.

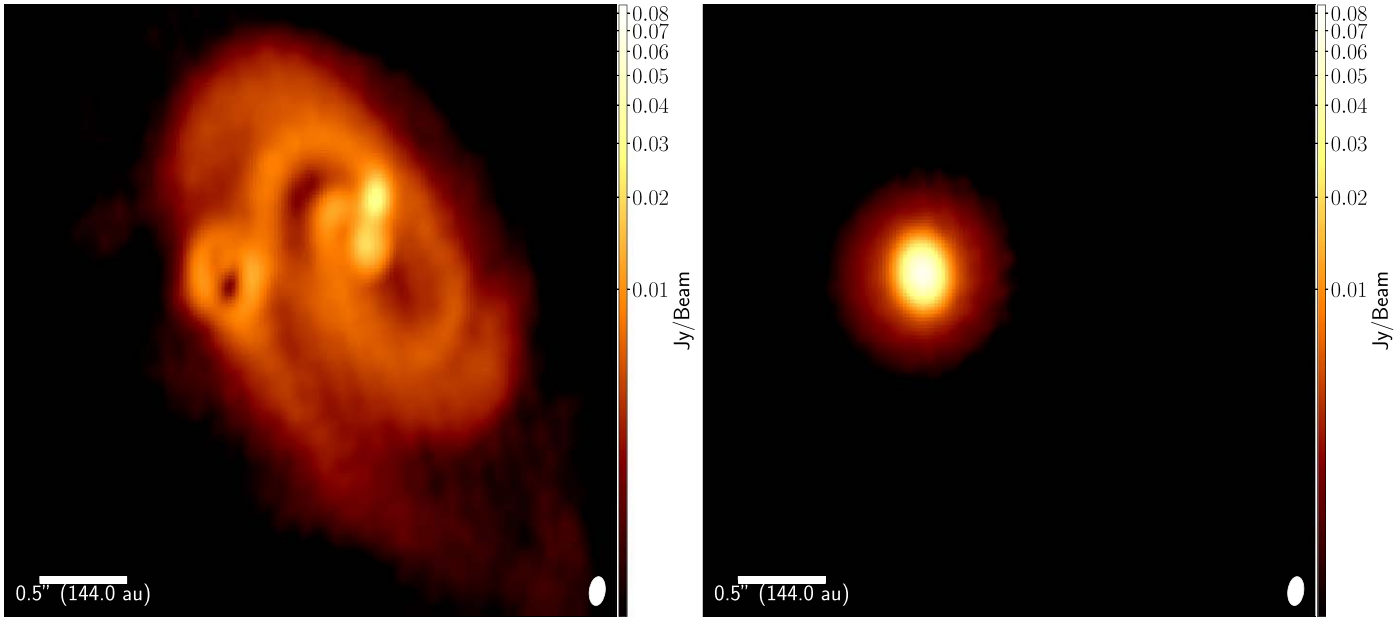

Figure 32. Continuum (879 μm) images of IRS3B with the tertiary clump removed (left image) for analysis and the model of the tertiary clump (right image). The tertiary model was constructed using two 2D Gaussians with a zero-level offset in order to properly restore the underlying disk emission without introducing additional features. The left image was used to exclude the embedded tertiary mass from the dust component of the circumstellar disk, while the right image image was then used for analysis of the compact dust emission around the tertiary.

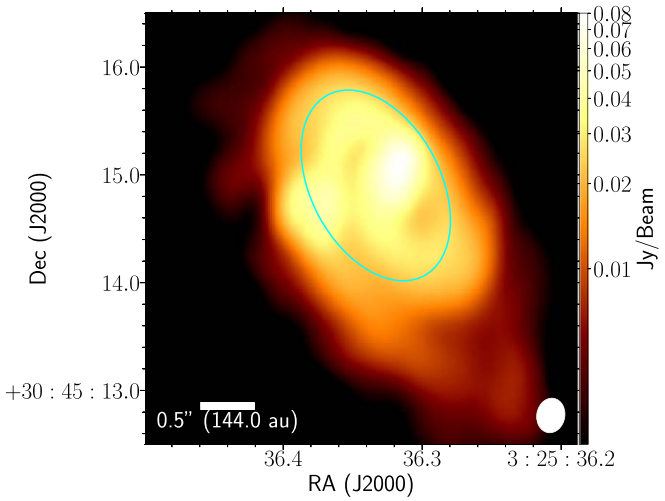

Figure 33. Continuum (879 μm) image of IRS3B with the tertiary removed, reconstructed with Briggs weighing robust parameter of 2 and tapered to 500 kλ. This smooths over the substructure of the continuum disk to enable fitting of the disk with a single 2D Gaussian profile, without overfitting the substructure. The cyan line is the Gaussian fit of the circum-multiple disk of IRS3B, with the major and minor axis of the ellipses defined by the FWHM major and minor axis of the 2D Gaussian fit.

ORCID iDs

Nickalas K. Reynolds https://orcid.org/0000-0002-9239-6422
John J. Tobin https://orcid.org/0000-0002-6195-0152
Patrick Sheehan https://orcid.org/0000-0002-9209-8708
Kaitlin M. Kratter https://orcid.org/0000-0001-5253-1338
Claire J. Chandler https://orcid.org/0000-0002-7570-5596
Dominique Segura-Cox https://orcid.org/0000-0003-3172-6763
Leslie W. Looney https://orcid.org/0000-0002-4540-6587
Michael M. Dunham https://orcid.org/0000-0003-0749-9505

References

Abt, H. A. 1983, ARA&A, 21, 343
Adams, F. C., Ruden, S. P., & Shu, F. H. 1989, ApJ, 347, 959
André, P., Di Francesco, J., Ward-Thompson, D., et al. 2014, in Protostars and Planets VI, ed. H. Beuther et al. (Tucson, AZ: Univ. Arizona Press), 27
Andre, P., Ward-Thompson, D., & Barsony, M. 1993, ApJ, 406, 122
Andrews, S. M., Rosenfeld, K. A., Kraus, A. L., & Wilner, D. J. 2013, ApJ, 771, 129
Andrews, S. M., Wilner, D. J., Hughes, A. M., Qi, C., & Dullemond, C. P. 2009, ApJ, 700, 1502
Arce, H. G., & Sargent, A. I. 2006, ApJ, 646, 1070
Artymowicz, P., & Lubow, S. H. 1996, in Interaction of Young Binaries with Protostellar Disks, ed. S. Beckwith et al. (Berlin: Springer), 115, doi:10.1007/BFb0102630
Astropy Collaboration, Robitaille, T. P., Tollerud, E. J., et al. 2013, A&A, 558, A33
Audard, M., Ábrahám, P., Dunham, M. M., et al. 2014, in Protostars and Planets VI, ed. H. Beuther et al. (Tucson, AZ: Univ. Arizona Press), 387
Bate, M. R., Bonnell, I. A., & Bromm, V. 2002, MNRAS, 336, 705
Bohlin, R. C., Savage, B. D., & Drake, J. F. 1978, ApJ, 224, 132
Booth, A. S., & Ilee, J. D. 2020, MNRAS, 493, L108
Boss, A. P., & Keiser, S. A. 2013, ApJ, 764, 136
Caselli, P., Hartquist, T. W., & Havnes, O. 1997, A&A, 322, 296
Chabrier, G. 2005, in The Initial Mass Function 50 Years Later, Astrophysics and Space Science Library Vol. 327, ed. E. Corbelli, F. Palla, & H. Zinnecker (Dordrecht: Springer), 41
Dullemond, C. P., Juhasz, A., Pohl, A., et al. 2012, RADMC-3D: A Multi-purpose Radiative Transfer Tool, v. 2.0, Astrophysics Source Code Library, ascl:1202.015
Dunham, M. M., Vorobyov, E. I., & Arce, H. G. 2014, MNRAS, 444, 887
Duquennoy, A., & Mayor, M. 1991, A&A, 248, 485
Enoch, M. L., Evans, N. J., II, Sargent, A. I., & Glenn, J. 2009, ApJ, 692, 973
Evans, N. J. I. 1999, ARA&A, 37, 311
Fischer, W., Megeath, T., Furlan, E., et al. 2013, Protostars and Planets VI, Poster, #1H023
Fisher, R. T. 2004, ApJ, 600, 769
Foreman-Mackey, D., Hogg, D. W., Lang, D., & Goodman, J. 2013, PASP, 125, 306
Ginsburg, A., Bally, J., Goddi, C., Plambeck, R., & Wright, M. 2018, ApJ, 860, 119
Green, J. D., Evans, N. J. I., Jørgensen, J. K., et al. 2013, ApJ, 770, 123
Hall, C., Dong, R., Teague, R., et al. 2020, arXiv:2007.15686
Harris, C. R., Millman, K. J., van der Walt, S. J., et al. 2020, Natur, 585, 357

Hartmann, L., Cassen, P., & Kenyon, S. J. 1997, ApJ, 475, 770
Hartmann, L., & Kenyon, S. J. 1996, ARA&A, 34, 207
Hunter, J. D. 2007, CSE, 9, 90
Jørgensen, J. K., Johnstone, D., Kirk, H., & Myers, P. C. 2007, ApJ, 656, 293
Jørgensen, J. K., van Dishoeck, E. F., Visser, R., et al. 2009, A&A, 507, 861
Kratter, K., & Lodato, G. 2016, ARA&A, 54, 271
Kratter, K. M., Matzner, C. D., Krumholz, M. R., & Klein, R. I. 2010a, ApJ, 708, 1585
Kratter, K. M., Murray-Clay, R. A., & Youdin, A. N. 2010b, ApJ, 710, 1375
Kristensen, L. E., & Dunham, M. M. 2018, arXiv:1807.11262
Kwon, W., Looney, L. W., Mundy, L. G., Chiang, H.-F., & Kemball, A. J. 2009, ApJ, 696, 841
Lada, C. J. 1987, in IAU Symp. 115, Star Forming Regions, ed. M. Peimbert & J. Jugaku (Cambridge: Cambridge Univ. Press), 1
Lee, A. T., Offner, S. S. R., Kratter, K. M., Smullen, R. A., & Li, P. S. 2019, ApJ, 887, 232
Li, Z.-Y., Banerjee, R., Pudritz, R. E., et al. 2014, in Protostars and Planets VI, ed. H. Beuther et al. (Tucson, AZ: Univ. Arizona Press), 173
Lin, D. N. C., & Pringle, J. E. 1990, ApJ, 358, 515
Lis, D. C., Keene, J., Young, K., et al. 1997, Icar, 130, 355
Lodders, K. 2003, ApJ, 591, 1220
Maret, S., Maury, A. J., Belloche, A., et al. 2020, A&A, 635, A15
Mathieu, R. D. 1994, ARA&A, 32, 465
McBride, A., & Kounkel, M. 2019, ApJ, 884, 6
McMullin, J. P., Waters, B., Schiebel, D., Young, W., & Golap, K. 2007, in ASP Conf. Ser. 376, Astronomical Data Analysis Software and Systems XVI, ed. R. A. Shaw, F. Hill, & D. J. Bell (San Francisco, CA: ASP), 127
Mercer, A., & Stamatellos, D. 2017, MNRAS, 465, 2
Moe, M., & Di Stefano, R. 2017, ApJS, 230, 15
Moeckel, N., & Bate, M. R. 2010, MNRAS, 404, 721
Nyquist, H. 1928, Transactions of the American Institute of Electrical Engineers, 47, 617
Offner, S. S. R., & Arce, H. G. 2014, ApJ, 784, 61
Offner, S. S. R., Kratter, K. M., Matzner, C. D., Krumholz, M. R., & Klein, R. I. 2010, ApJ, 725, 1485
Ortiz-León, G. N., Loinard, L., Dzib, S. A., et al. 2018, arXiv:1808.03499
Ossenkopf, V., & Henning, T. 1994, A&A, 291, 943
Padoan, P., & Nordlund, Å. 2004, ApJ, 617, 559
Pérez, S., Casassus, S., & Benéz-Llambay, P. 2018, MNRAS, 480, L12
Perez, S., Dunhill, A., Casassus, S., et al. 2015, ApJL, 811, L5
Pinte, C., Ménard, F., Duchêne, G., et al. 2018a, A&A, 609, A47
Pinte, C., Price, D. J., Ménard, F., et al. 2018b, ApJL, 860, L13
Pinte, C., van der Plas, G., Ménard, F., et al. 2019, NatAs, 3, 1109
Plunkett, A. L., Arce, H. G., Mardones, D., et al. 2015, Natur, 527, 70
Price-Whelan, A. M., Sipőcz, B. M., Günther, H. M., et al. 2018, AJ, 156, 18
Raghavan, D., McAlister, H. A., Henry, T. J., et al. 2010, ApJS, 190, 1
Reipurth, B., & Mikkola, S. 2012, Natur, 492, 221
Robitaille, T., & Bressert, E. 2012, APLpy: Astronomical Plotting Library in Python, v. 1.1.1, Astrophysics Source Code Library, ascl:1208.017
Rosenfeld, K. A., Andrews, S. M., Hughes, A. M., Wilner, D. J., & Qi, C. 2013, ApJ, 774, 16
Sadavoy, S. I. 2013, PhD thesis, Univ. Victoria
Sadavoy, S. I., Di Francesco, J., André, P., et al. 2014, ApJL, 787, L18
Sadavoy, S. I., & Stahler, S. W. 2017, MNRAS, 469, 3881
Safron, E. J., Fischer, W. J., Megeath, S. T., et al. 2015, ApJL, 800, L5
Seifried, D., Sánchez-Monge, Á, Walch, S., & Banerjee, R. 2016, MNRAS, 459, 1892
Sharma, R., Tobin, J. J., Sheehan, P. D., et al. 2020, arXiv:2010.05939
Sheehan, P. D., Wu, Y.-L., Eisner, J. A., & Tobin, J. J. 2019, ApJ, 874, 136
Shu, F. H., Adams, F. C., & Lizano, S. 1987, ARA&A, 25, 23
Sierra, A., & Lizano, S. 2020, ApJ, 892, 136
Stahler, S. W., Korycansky, D. G., Brothers, M. J., & Touma, J. 1994, ApJ, 431, 341
Stamatellos, D., Hubber, D., & Hubber, A. 2011, in ASP Conf. Ser. 451, 9th Pacific Rim Conference on Stellar Astrophysics, ed. S. Qain et al. (San Francisco, CA: ASP), 213
Stamatellos, D., & Whitworth, A. P. 2009, MNRAS, 392, 413
Tazzari, M., Beaujean, F., & Testi, L. 2018, MNRAS, 476, 4527
Terebey, S., Shu, F. H., & Cassen, P. 1984, ApJ, 286, 529
Tobin, J. J., Hartmann, L., Chiang, H.-F., et al. 2013, ApJ, 771, 48
Tobin, J. J., Kratter, K. M., Persson, M. V., et al. 2016a, Natur, 538, 483
Tobin, J. J., Looney, L. W., Li, Z.-Y., et al. 2016b, ApJ, 818, 73
Tobin, J. J., Megeath, S. T., van't Hoff, M., et al. 2019, ApJ, 886, 6
Tobin, J. J., Sheehan, P. D., Megeath, S. T., et al. 2020, ApJ, 890, 130
Ulrich, R. K. 1976, ApJ, 210, 377
Virtanen, P., Gommers, R., Oliphant, T. E., et al. 2019, arXiv:1907.10121
Visser, R., van Dishoeck, E. F., & Black, J. H. 2009, A&A, 503, 323
Vorobyov, E. I., & Basu, S. 2011, in IAU Symp. 276, The Astrophysics of Planetary Systems: Formation, Structure, and Dynamical Evolution, ed. A. Sozzetti, M. G. Lattanzi, & A. P. Boss (Cambridge: Cambridge Univ. Press), 463
Vorobyov, E. I., & Elbakyan, V. G. 2019, A&A, 631, A1
Vorobyov, E. I., Pavlyuchenkov, Y. N., & Trinkl, P. 2014, ARep, 58, 522
Whitney, B. A., Wood, K., Bjorkman, J. E., & Wolff, M. J. 2003, ApJ, 591, 1049
Wilkin, F. P., & Stahler, S. W. 1998, ApJ, 502, 661
Williams, J. P., & Best, W. M. J. 2014, ApJ, 788, 59
Wilson, T. L., Rohlfs, K., & Hüttemeister, S. 2009, Tools of Radio Astronomy (Berlin: Springer)
Wilson, T. L., & Rood, R. 1994, ARA&A, 32, 191
Worley, C. E. 1962, AJ, 67, 590
Yen, H.-W., Koch, P. M., Takakuwa, S., et al. 2017, ApJ, 834, 178
Yen, H.-W., Takakuwa, S., Ohashi, N., et al. 2014, ApJ, 793, 1
Yorke, H. W., & Bodenheimer, P. 1999, ApJ, 525, 330
Zhu, Z., Zhang, S., Jiang, Y.-F., et al. 2019, ApJL, 877, L18
Zucker, C., Speagle, J. S., Schlafly, E. F., et al. 2019, ApJ, 879, 125